Unmanned Aerial Vehicle-based Non-destructive Testing Methods for Concrete Structures

by

Sean Blaney
BASc. in Engineering Science, University of Toronto, 2015

A Thesis submitted in Partial Fulfillment of the
Requirements for the Degree of

MASTER OF APPLIED SCIENCE

in the Department of Mechanical Engineering

©Sean Blaney, 2018
University of Victoria

All rights reserved. This thesis may not be reproduced in whole or in part,
by photocopy or other means, without the permission of the author.

Unmanned Aerial Vehicle-based Non-destructive Testing Methods for Concrete Structures

by

Sean Blaney
BASc. in Engineering Science, University of Toronto, 2015

Supervisory Committee

Dr. Rishi Gupta, Supervisor
Department of Civil Engineering

Dr. Yang Shi, Departmental Member
Department of Mechanical Engineering

Abstract

In this work, unmanned aerial vehicle-based non-destructive testing methods for concrete structures are evaluated and developed. There exists a need for improved infrastructure inspection techniques with increased expediency. Unmanned aerial vehicles (UAVs) are highly mobile and have shown promise towards achieving this directive, but more work is required to adapt traditional NDT methods to be UAV-compatible. To this end, concrete sounding techniques were evaluated with a quantitative acoustic frequency analysis procedure on a series of concrete slabs. One such method was adapted for use with a UAV and was used to detect subsurface voids in one of the concrete samples and offer a means of depth estimation. This work was complemented with experiments concerning UAV-based visual and infrared imaging techniques already in practice for UAV-based concrete inspection. Together, findings indicate the strengths and weaknesses of the NDTs tested and suggest further improvements for UAV-based NDTs and inspection strategies moving forward. Development of a novel sensor platform for UAV-based measurement, as well as results of an actual bridge inspection using infrared and optical methods demonstrate the present capabilities of the UAV-based instrumentation.

Table of Contents

Supervisory Committee ii

Abstract iii

Table of Contents iv

List of Figures vii

List of Tables x

Abbreviations xi

Unit Abbreviations xii

1 Introduction 1

1.1 Background and motivation 1

1.1.1 Current non-destructive tests for concrete structures 2

1.1.2 The need for UAV inspection techniques 3

1.1.3 Current state of UAV-based infrastructure inspection 3

1.2 Objectives 4

1.3 Thesis Outline 5

1.4 Research Contributions 5

2 UAV-based optical imaging of concrete structures 6

2.1 Optical image inspection flight strategy 6

2.1.1 Image quality and blurring 7

2.1.2 Motion blur 7

2.1.3 Blur caused by inadequate focus 13

2.1.4 Image sensor: a note on potential issues with sensor size and image resolution 16

2.1.5 Flight strategy sample calculation 17

2.2 Distance and crack width estimation utility 18

3 UAV-based infrared thermography of concrete structures 23

3.1 Infrared thermography as a tool for concrete and bridge inspection 23

3.2 Infrared imaging of voids and delaminations in concrete test specimens . . 24

3.2.1 Specimens, equipment, and test conditions 24

3.2.2 Infrared imaging results 26

3.2.3 Infrared imaging conclusions 29

4 Sounding of subsurface concrete defects using frequency response of flexural vibration 30

Abstract 31

Nomenclature 32

4.1 Introduction 32

4.1.1 Problem Statement 32

4.1.2 Concrete Sounding Background 32

4.1.3 Expected flexural frequency peak 34

4.2 Specimens 37

4.3 Methods 43

4.3.1 Audio recording and processing 43

4.3.2 Hammer percussion sounding 44

4.3.3 Speaker-based excitation sounding 46

4.3.4 Modified chain drag 47

4.3.5 Accelerometer and glass disc reference measurements 48

4.4 Defect detection performance 49

4.4.1 Slab vibration and thickness ratio 52

4.4.2 Speaker performance: glass 54

4.4.3 Speaker performance: concrete 56

4.4.4 Performance of hammer percussion and chain drag 58

4.5 Conclusions 59

Acknowledgements 60

5 UAV-based sounding of subsurface concrete defects 61

Abstract 62

5.1 Introduction 63

5.2 Specimens 63

5.3 Concrete sounding 65

5.4 Noise Reduction Strategy 66

5.5 UAV-based performance relative to baseline and reference results 67
5.6 Effect of noise reduction measures 68
5.7 Conclusion 71
5.8 Acknowledgments 72

6 Implementation of UAV-based inspection methods 73
6.1 A UAV-compatible Instrumentation Platform 73
6.2 Platform design 74
6.3 Prototype 77
6.3.1 Materials and construction 77
6.3.2 Operation and features 78
6.4 Skutz River Bridge Inspection 80
6.5 Legal use of research UAVs in Canada 80
6.6 Skutz Bridge and imaging conditions 80
6.7 Skutz Bridge deck imaging results 81
6.8 Bridge deck shadow area comparison 83
6.9 Skutz Bridge deck inspection conclusions 84

7 Conclusions 86
7.1 Future work 87
7.1.1 Optical and thermal methods 87
7.1.2 UAV-based concrete sounding 88

References 89

Appendix A Images used in distance and crack width estimation 96

Appendix B Thermal images of concrete slab specimens 99

Appendix C i3P Prototype Images 105

List of Figures

2.1 The basic geometry of a thin lens. 9
2.2 P3S camera blur for a range of distances and speeds. 12
2.3 Thin lens DOF parameters. 15
2.4 Location of top, middle, and bottom measurements on a sample. 19

3.1 The P3S mid-flight. 25
3.2 The FLIR Vue Pro as mounted on the P3S. 26
3.3 Infrared images of each slab. 27

4.1 Slab defect depth and lateral size. 35
4.2 The plot used to estimate h/b from Nelson. 36
4.3 Slab 3 dimensions. 39
4.4 Slab formwork. 40
4.5 Slab and defect numbering. 43
4.6 Microphone configuration. 44
4.7 Zoom H1 recorder and hammers. 45
4.8 Hammer percussion test configuration. 46
4.9 Slab speaker test. 47
4.10 Single-link chain drag configuration. 48
4.11 Accelerometer configuration. 49
4.12 Frequency spectrums for 2 oz. hammer test. 50
4.13 Normalized spectrums for glass speaker test. 55
4.14 Glass up- and down-chirp spectrum comparison. 56
4.15 Speaker test concrete spectrums. 57

5.1 UAV-based sounding test setup. 64
5.2 Slab section views showing cover dimensions. 64
5.3 Diagram of basic UAV-based test setup. 66
5.4 Impact FFT before and after noise reduction. 68
5.5 STFT spectrograms of a recording of an impact. 70

6.1 Diagram of i3P connections and layout. 74
6.2 The i3P design with arms fixed in an upright position. 76
6.3 The i3P design with arms retracted. 76
6.4 Overview of i3P prototype. 77
6.5 Underside of i3P prototype. 78
6.6 i3P prototype demonstrating a thermal image broadcast. 79
6.7 Overview of Skutz bridge elements visible in optical images. 81
6.8 Optical and thermal Skutz bridge deck images. 82
6.9 Optical and thermal images of the Skutz bridge deck debris. 83
6.10 Skutz Bridge divider shadow optical images. 85
6.11 Skutz Bridge divider shadow infrared images. 85

A.1 Images for sample #1 from the Phantom 3 Standard. 96
A.2 Images for sample #2 from the Phantom 3 Standard. 97
A.3 Images for sample #1 from the Sony DSC-W570 Camera. 97
A.4 Images for sample #2 from the Sony DSC-W570 Camera. 98

B.1 Thermal images of slabs #1 and 2. 99
B.2 Thermal images of slabs #1, 2, 3, and 4. 100
B.3 Thermal images of slabs #3 and 4. 101
B.4 Thermal images of slabs #3, 4, and 5. 102
B.5 Thermal images of slabs #6 and 7. 103
B.6 Thermal images of slabs #6 and 7. 104

C.1 Taranis X9D Plus RC Remote 105
C.2 i3P prototype showing cameras and antennae. 106
C.3 i3P prototype showing arm positions. 107

C.4 i3P prototype images. 108
C.5 i3P prototype images showing opposite sides. 109
C.6 i3P prototype images featuring optical and thermal cameras. 110
C.7 i3P showing optical camera broadcast. 111

List of Tables

2.1 Key parameters of the P3S aircraft and its camera. 11

2.2 Optical strategy sample calculations. 18

2.3 Crack distance and width evaluated at the top of each crack. 20

2.4 Crack distance and width evaluated at the middle of each crack. 21

2.5 Crack distance and width evaluated at the bottom of each crack. 21

3.1 Thermal image defect size estimates. 28

4.1 Dimensions and depths of defects. 42

4.2 Defects detected. 52

4.3 Defect detection sorted by depth ratio. 53

5.1 Frequencies of peaks for simulated subsurface voids. 67

Abbreviations

COC	Circle of confusion
CW	Crack width
DOF	Depth of field
NDT	Non-destructive test or non-destructive testing
P3S	Phantom 3 Standard
SFOC	Special Flight Operations Certificate
UAV	Unmanned aerial vehicle

Unit Abbreviations

MPa	Megapascal
N	Newton
Nm	newton meter
in	inch
kg	kilogram
kg/m^3	kilograms per cubic meter
m	meter
m/s	meters per second
mm	millimeter
px	pixel

Chapter 1

Introduction

1.1 Background and motivation

Unmanned aerial vehicles (UAVs) promise to transform a multitude of industries and commercial processes from parcel delivery to agriculture, and infrastructure inspection is no exception. As the most commonly used building material worldwide, concrete forms an essential component of a variety of structures from skyscrapers to bridges. Accordingly, concrete testing stands to feature prominently during UAV-based infrastructure inspection. Non-destructive testing (NDT) in particular is an important form of evaluation for structures prior to the end of service life.

Non-destructive testing of concrete structures is well-established; there exist a wide variety of techniques and methods currently in practice [1]. Many standard methods are designed to be performed by a human inspector manually with hand held equipment [2–4]. However, access to the areas of some structures by human operators is limited. For example, bridge spans possess a number of features that can be very difficult to gain direct access to like the underside of the deck [5].

Infrastructure in just Canada and the United States is expected to require significant investment to replace, repair, and maintain. The extrapolated poor bridge replacement costs for Canada are estimated at roughly 2 billion CAD [6]. In the United States, there is an estimated need for 123-billion USD required for bridge rehabilitation [7].

UAV-based inspection platforms offer an alternative to traditional hand held methods. Hand held methods are restricted by the mobility of the operator, but UAV-based instru-

ments are able to move unencumbered by limits of human movement. A UAV can access the underside and sides of a bridge deck or the high reaches of a building edifice in short order. UAV-based inspection methods have the potential to be significantly faster than hand held methods.

With this in mind, it is no surprise there already exist a number of commercial UAVs advertised as tools for infrastructure inspection [8, 9]. A February 2018 report from Global Market Insights [10] indicates the 2016 commercial drone market was over USD 2 billion, and is projected to reach USD 17 Billion by 2024 with an expected compound annual growth rate of roughly 25 %.

Current NDT methods of concrete inspection are typically limited to means of contact measurement. If UAVs are to further develop as a means of delivering inspection instruments to concrete structures, the feasibility of contact measurements needs to be explored.

This thesis aims to investigate currently practiced UAV-based inspection techniques and to evaluate the possibility of additional techniques.

1.1.1 Current non-destructive tests for concrete structures

There are a variety of non-destructive tests for concrete structures, but the basic premise of all NDTs is the same; some information about the structure must be obtained without inflicting any damage upon it [11]. Typically, NDTs use visible light, infrared emissions, sound, vibration, conduction, or some other kind of electromagnetic emission or response to obtain information from the structure.

Visual inspection is a hugely popular procedure that evaluates the surface of the structure for signs of damage, defect, or disrepair. Acoustic methods like coin tapping and chain drag use the sound of the structure to locate defects [2]. Frequency analysis or more intensive stress-wave methods like impact echo testing can yield information about the depths of defects [12]. In this vein, similar methods are under development that use nonlinear waves [13]. Ground penetrating radar can also see below the surface of concrete to detect subsurface defects. Conductivity, half-cell potential, and electrical resistivity can yield information about the as-built concrete material properties of a particular structure. Non-contact ultrasonic methods have been used to detect surface cracks [14] and subsurface defects [15].

Infrared thermography can rapidly assess the condition of large areas of concrete, and is capable of detecting subsurface defects but not estimating their depth. Some of these methods like chain drag as presently standardized are operator dependent [16], but newer techniques that record acoustic signals and process them for frequency content to remove subjectivity have been demonstrated [17]. A laser Doppler vibrometer can be coupled with a method of excitation, a long-range acoustic device for example, to detect subsurface concrete defects [18].

1.1.2 The need for UAV inspection techniques

Infrastructure inspection is traditionally the domain of skilled operators trained in the use of specialized hand held equipment. While this approach has worked adequately, for many structures, it requires a host of accommodations to maneuver the inspector to the location of the inspection site on the structure. For example, an inspection of the underside of a bridge deck may require an elaborate crane-like vehicle or the installation of scaffolding, or harnessing to allow the inspector access to the desired bridge components.

Manual inspections also present an issue in terms of scale in that very large structures are difficult to inspect in a timely fashion. Long span bridges in India may extend over 1000 m with dozens of spans [19], so a rapid method of getting the inspection tools where they are needed is required. A vehicle may suffice for some locations on such a structure, but the sides and underside of the bridge are a greater challenge.

It has been shown for visual inspections that UAVs can offer a more expedient alternative to traditional methods of inspecting some large concrete structures. Inspection strategies and best practices to this end have been investigated by a variety of researchers [5, 20, 21].

1.1.3 Current state of UAV-based infrastructure inspection

UAV-based infrastructure inspection is advertised for a number of commercial platforms available [8, 9]. The most common NDT tools used on the platforms available are optical and infrared cameras.

Optical cameras on UAVs for infrastructure inspection can reach areas of structures that are not easily accessible to human inspectors. A variety of structures may be inspected.

Visual inspection strategies have been investigated by various researchers [5, 20, 21]. Surface crack detection is a key element of visual inspection, and a number of efforts have been made to detect and analyze cracks in images during a UAV-based inspection of a concrete or masonry structure [22–24].

Use of infrared (IR) cameras for inspection of concrete structures is well established as a means of detecting defects like near-surface delaminations [2]. To this end, infrared cameras have been tested by Ellenberg et al. [25] on mock bridge decks to successfully detect induced delaminations and estimate their lateral size. The Minnesota Department of Transportation demonstrated the use of an infrared camera during inspection of an actual bridge deck [26], but the bridge did not contain any near-surface delaminations, so none were detected.

1.2 Objectives

The objectives of this document are succinctly summarized as follows:

1. Determine which method of excitation for concrete sounding shows the best performance with UAV-compatible acoustic devices.
2. Development of a cursory optical inspection strategy for long, roughly linear structures.
3. Evaluate the ability of a UAV-based infrared camera to detect simulated defects in concrete specimens.
4. Evaluate the ability of a UAV-based acoustic sounding method to detect simulated defects in concrete specimens.
5. Describe the development of a low-cost, UAV-compatible device to hold instrumentation for infrastructure inspection.
6. Document an inspection of a bridge deck using UAV-based optical and thermal cameras.

1.3 Thesis Outline

The thesis is presented in chapters. Chapter 1 describes the purpose and scope of the document. Chapter 4 characterizes the performance of sounding methods in evaluating concrete sounding methods. Chapters 2 and Chapter 3 consider optical and thermal methods of inspection respectively.

Chapter 5 demonstrates a proof-of-concept for a UAV-based concrete sounding method. Chapter 6 describes the creation of a custom prototype UAV instrumentation payload system, presents results of a bridge field inspection performed using optical and thermal methods, and makes general recommendations for future inspections.

1.4 Research Contributions

Established optical and thermal methods of concrete sample inspection are applied to a purpose-made set of concrete specimens with induced simulated delaminations and voids.

Acoustic methods are evaluated for inspection of these defects, including a method that makes use of a novel excitation method (speaker-based excitation). The best performer of these methods (hammer percussion) is combined with a UAV using an innovative passive actuation system. The UAV-based sounding is shown to be capable of defect depth estimate in the concrete samples.

The design and prototyping of a low-cost UAV payload is presented. The device described is an inventive platform to position and secure instruments like cameras on a UAV for infrastructure inspection purposes.

A bridge deck inspection of an actual bridge deck is described, and general recommendations for future inspections are proposed based on the results.

Chapter 2

UAV-based optical imaging of concrete structures

2.1 Optical image inspection flight strategy

The discussion of optical imaging presented in this section is primarily concerned with the impact of image quality on a simple flight strategy for a UAV.

UAVs have limited flight times dictated largely by battery life and payload. With this in mind, it is prudent to perform some rudimentary flight planning before performing an inspection of a very large and regularly shaped concrete structure. For example, a very long concrete bridge with multiple spans could extend 1000 m or longer like the 1205 m-long Old Surajbadi Highway Bridge in India [19]. Some elements like support columns occur at discrete intervals along the bridge span, but since the deck is more or less a contiguous piece, it may be possible to rapidly image the entire deck by moving an optical camera-equipped UAV at a continuous speed.

In order to adequately address the basics of a UAV flight plan for a visual inspection with the aim of detecting cracks or other features on a concrete surface such as the aforementioned bridge deck, there are a number of factors to consider. A "flight plan" in this context refers only to a desired constant distance and speed at which a flight can take place and still capture the level of detail about the subject of an optical camera-based inspection of a large reinforced concrete structure.

The aim of this section is to use simple estimation techniques for image quality to be able to make a basic flight strategy for a piece of infrastructure of a particular size. This preliminary flight strategy will include a speed and distance for a given set of parameters. Alternatively, it is possible to image the concrete structure with a UAV that moves rapidly between a series of waypoints at which it takes images while stationary.

2.1.1 Image quality and blurring

The ability to detect and estimate the size of a feature like a crack on the concrete surface requires an acceptable level of image quality. A discussion of image quality can include image clarity, resolution, visibility, and sharpness [27]. For a UAV-based optical camera, image blurring can be user controlled via speed and distance to some extent, and will form the basis for most of the discussion in this section. Blur can be the result of improper focus, camera and subject motion, low signal-to-noise ratio, diffraction, lens aberrations, and resolution problems [27].

Blur due to motion and improper focus are at the crux of the image quality and flight strategy discussion as they are relatively easy to relate to flight strategy. Resolution is an important consideration throughout the discussion of these two sources of blur. It is more difficult to establish a straightforward and meaningful relationship between the UAV flight strategy and other sources of blur, contrast, and sharpness. Correction of aberration (also referred to as distortion) is more important to estimating crack width in images in which the cracks are not located primarily towards the image center. Aberrations are less urgently relevant to the determination of a velocity-distance flight strategy insofar as they are determined by camera properties. Some aberration in UAV-based images has been shown to be removable in post-processing, such as the distortion correction reported by Ellenberg et al. [21].

The contents of the forthcoming discussion detail simple techniques to estimate blur for the purposes of developing a simple flight strategy.

2.1.2 Motion blur

Motion blur is an important consideration for a constant speed flight strategy. A stop-and-start waypoint-based inspection flight strategy does not include any significant motion blur.

Blur due to UAV motion depends on the properties of the camera mounted to the UAV, the distance between the camera and the concrete surface (insofar as it impacts the field of view or magnification of the image), as well as the UAV speed and direction of travel relative to the concrete surface [28].

To greatly simplify the analysis, it will be assumed that the UAV motion is in a plane parallel to the concrete surface it is inspecting. Out-of-plane trajectories either indicate the UAV is moving away from or towards a collision with the concrete surface, which is not conducive to a UAV inspection. The motion blur of an image can be estimated using the equation [28]:

$$b_v = \frac{t \cdot s_s \cdot v \cdot \cos\phi}{FOV} \tag{2.1}$$

In which b_v is the amount of motion-induced blur in the image in m, t is the exposure time in seconds, s_s is the image sensor size in m, v is the UAV speed in m/s, ϕ is the angle between the direction of motion and the subject of interest (in this case, the concrete surface), and FOV is the field of view of the camera lens in m. By modeling the camera lens as a thin lens, its behaviour is governed by the thin lens equation [29]:

$$\frac{1}{d_i} + \frac{1}{d} = \frac{1}{f} \tag{2.2}$$

In which d_i is the distance from the lens to the image sensor in m, d is the distance between the lens and the subject in m, and f is the focal length of the camera lens in m. In photographic terms, d_i is the image conjugate distance and d is the object conjugate distance [30]. It is helpful to note that the lateral magnification (also known as linear or transverse magnification) of the camera lens is described by the relationships [28, 29]:

$$M = \frac{h_i}{h_o} = \frac{d_i}{d} = \frac{s_s}{FOV} \tag{2.3}$$

In which M is the lateral magnification, h_i is the size of the image, and h_o is the size of the subject in any consistent set of units. Equations 2.2 and 2.3 can be combined to yield the useful expression:

$$M = \frac{f}{d - f} \tag{2.4}$$

Combining Equations 2.3 and 2.4 gives an expression for the distance to the subject of interest:

$$d = \frac{f \cdot h_o}{h_i} + f \tag{2.5}$$

It is worth noting that all terms in Equation 2.5 are distance and all have the same units—

m for the purpose of this discussion. The relationships for Equations 2.2 and 2.5 are illustrated in Figure 2.1.

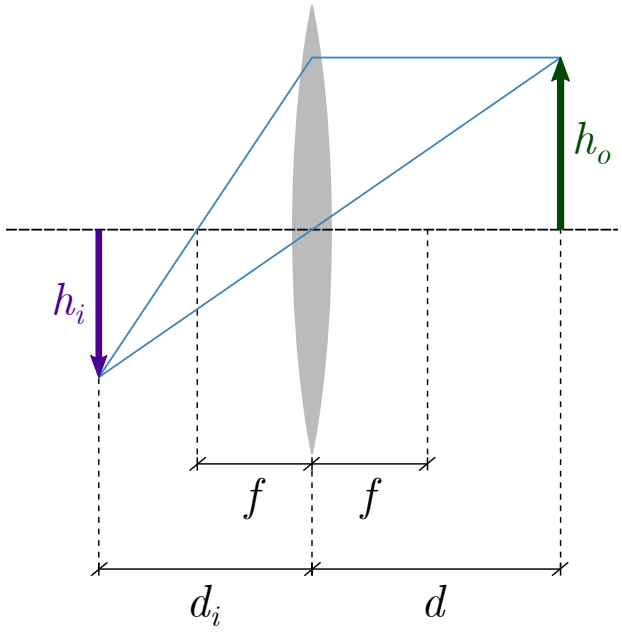

Figure 2.1: The basic geometry of a thin lens.

Equations 2.1 and 2.3 can be used with the assumption that direction of motion is parallel to the surface being imaged (i.e. $\phi = 0$) to yield a simplified expression for the blur:

$$b_v = t \cdot M \cdot v \tag{2.6a}$$

$$b_v = t \left(\frac{f}{d - f} \right) v \tag{2.6b}$$

A measured size on the image sensor in pixels ($h_{i,px}$) can be converted to the size of the image in m ($h_{i,m}$) using the image sensor size in both pixels and m ($s_{s,px}$ and $s_{s,m}$ respectively) via the relationship:

$$h_{i,m} = h_{i,px} \left(\frac{s_{s,m}}{s_{s,px}} \right) \tag{2.7}$$

The ratio of pixels in the image to the real-life size of the actual subejct ($h_{o,m}$) is given by:

$$\frac{h_{o,m}}{h_{i,px}} = \frac{s_{s,m}}{s_{s,px}} \frac{1}{M} \tag{2.8}$$

The calculation of distance between the lens and the subject of interest (d) normally

requires a reference object in-plane with the subject. The actual length of the reference in meters ($h_{o,m}$) must be known. The pixels in an image are rectilinear, so the reference distance should be either roughly vertical or horizontal in the image. This means a vertical reference requires the sensor size be the height of the image sensor, and a horizontal reference requires the sensor size be the width of the image sensor. For an image with known parameters:

- f— focal length in m
- $s_{s,m}$ and $s_{s,px}$— sensor size in m and pixels
- t— exposure time in s
- $h_{o,m}$— reference object size (in m) in plane with the subject of interest
- v— UAV speed (in m) relative to the subject of interest and reference

The distance to the subject of interest and the expected motion blur can be estimated using the following procedure:

1. Measure the size of the reference object image in pixels ($h_{i,px}$)
2. Convert the reference image size to meters using Eq. 2.7 (i.e. compute $h_{i,m}$)
3. Compute distance to the subject of interest using Eq. 2.5 with $d = f\left(\frac{h_{0,m}}{h_{i,m}}\right) + f$
4. Compute the magnification using Eq. 2.4
5. Compute the blur (in m) using Eq. 2.6
6. Convert the blur to pixels (if desired) using one of the ratios in Eq. 2.7

This procedure is helpful for the analysis of a single instance of an image. To perform some level of flight planning, the easiest thing to do is to use the same equations along with a known minimum size of object that is desired for detection, both in the image ($h_{i,px}$) and in-plane ($h_{o,m}$). To express this more compactly, Equations 2.3, 2.5, and 2.7 can be combined to yield the expressions:

$$h_{o,m} = h_{i,px}\left(\frac{d-f}{f}\right)\frac{s_{s,m}}{s_{s,px}} \tag{2.9a}$$

$$h_{i,px} = h_{o,m}\left(\frac{f}{d-f}\right)\frac{s_{s,px}}{s_{s,m}} \tag{2.9b}$$

Or, in terms of d:

$$d = f\left(\frac{h_{o,m}}{h_{i,px}}\frac{s_{s,px}}{s_{s,m}} + 1\right) \tag{2.10}$$

For example, a camera with sensor size 4000 pixels/6.25 mm and focal length 3.61 mm at a distance 1 m from a concrete surface, a crack of actual width 5 mm will be roughly 12 pixels in the image without any blur:

$$h_{i,px} = h_{o,m}\left(\frac{f}{d-f}\right)\frac{s_{s,px}}{s_{s,m}} = 0.005\left(\frac{0.00361}{1.0-0.00361}\right)\left(\frac{4000}{0.00625}\right) = 11.59 \text{ pixels}$$

Any blur (in pixels) can still be computed using Equations 2.4, 2.6, and 2.7. In this example, say the UAV is moving at 10 m/s, and the camera has exposure time 1/8000 s, then the blur would be 4.5288×10^{-6} m or roughly 3 pixels:

$$b_{v,m} = t \cdot \frac{f}{d-f} \cdot v = (1/8000)\left(\frac{0.00361}{1-0.00361}\right)10 = 4.5288 \times 10^{-6} \text{ m}$$

$$b_{v,px} = b_{v,m} \cdot \frac{s_{s,px}}{s_{s,m}} = 4.5288 \times 10^{-6}\left(\frac{4000}{0.00616}\right) = 2.9408 \text{ pixels}$$

Essentially, for a particular camera, the distance and speed of the UAV during a concrete inspection must be selected according to the desired width of crack to be detected, and the required width of the crack in the image (including blur considerations).

The key parameters of the camera and Phantom 3 Standard UAV used in this research are shown in Table 2.1. Some of this information is visualized in Figure 2.2.

Table 2.1: Key parameters of the P3S aircraft and its camera.

Parameter	**Value**
Focal length	3.61 mm
Sensor Size (w × h)	4000 × 3000 pixels 6.25 × 4.69 mm
Sensor Size (diag.)	7.81 mm
Exposure time	8 to 1/1000 s
f-number (relative aperture)	f/2.8
FOV	94°
Max aircraft speed	16 m/s

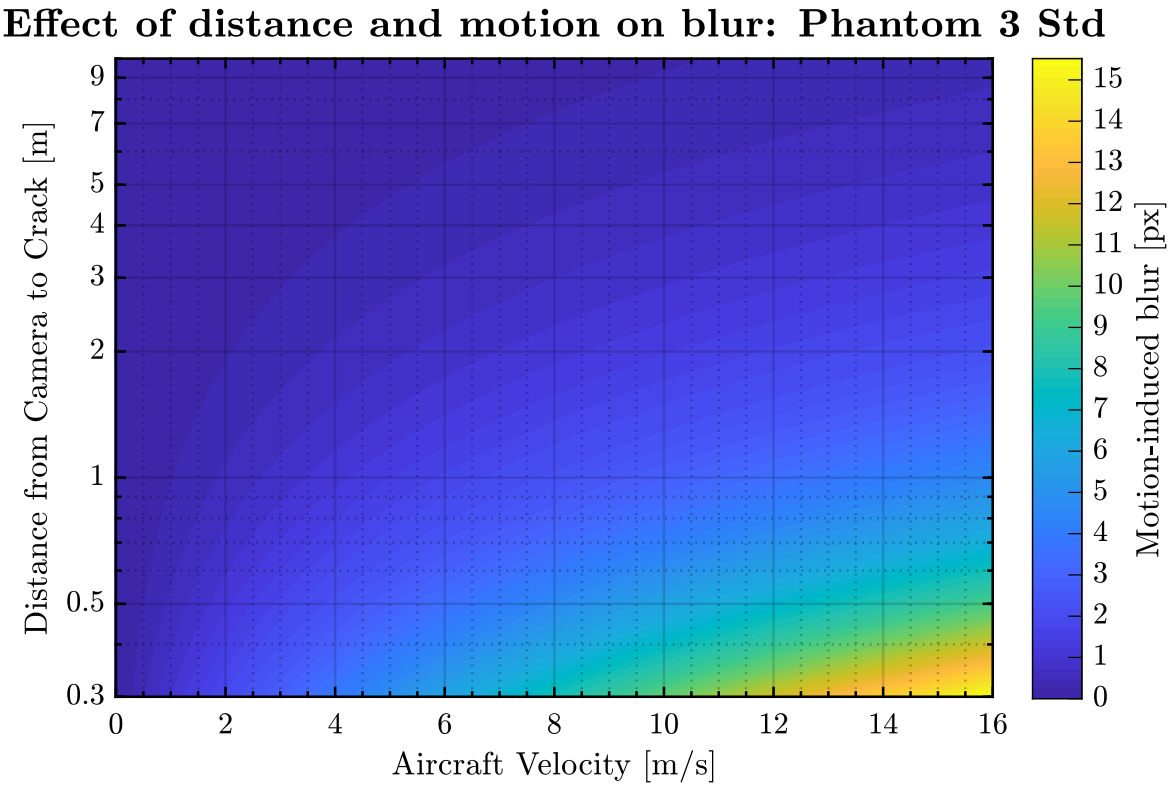

Figure 2.2: P3S camera blur for a range of distances and speeds.

Essentially, Figure 2.2 is a visual representation of Eq. 2.6b using the P3S parameters in Table 2.1 with velocities ranging between and distances from 200 to 5000 mm. Since $d >> f$ in this case, it may be said that the blur in the image in pixels is directly proportional to the velocity in m/s, and roughly inversely proportional to the distance between the camera lens and crack surface in meters. Using 2.9b with a range of distances from 200 to 5000 mm, and a range of actual crack widths from 0 to 10 mm the same relationship emerges between actual crack width (mm), distance, and image crack width (px). The crack width in the image in pixels is directly proportional to the crack width in meters, and roughly inversely proportional to the distance between the camera lens and crack surface in meters. While Figure 2.2 is for the P3S camera, the shape of the plot will be similar for other cameras, although the values on the axes and colourbar will change according to the specific camera parameters. It follows that flight planning according to aircraft velocity is very straightforward, as outlined in Procedure 2.1.

Procedure 2.1: Determination of basic flight strategy.

1. Determine camera properties (focal length, sensor size in mm and pixels, exposure time)
2. Decide on three of: minimum acceptable actual crack width (mm), minimum acceptable image crack width (px), subject distance (mm), image blur (px), and maximum aircraft velocity (m/s)
   (a) Compute the other two using the known parameters and Equations 2.6b, 2.9, and 2.10 as required

2.1.3 Blur caused by inadequate focus

While velocity-induced blur can be cause for concern, blur is also commonly caused by out-of-focus images. For UAV-based photography with stock cameras, focus issues can be further compounded by a fixed focal length and fixed focus distance. The discussion in this section will center on the effect of distance on focusing.

Using a relatively simply optical model, it is first helpful to describe an in-focus image. When an image is in focus, a point of light on the subject is projected through the lens to a point on the image sensor, as is depicted in Figure 2.1. However, there is no guarantee that the image sensor will be at the location where the image is projected by the lens: it may be either in front of or behind the image projection. What this means for our point of light on the subject is that it will appear as a circle on the image sensor. This circle is called the circle of confusion (COC, or c). The size of the maximum acceptable circle of confusion is affected by the camera lens properties and focus distance, but is ultimately determined by either lens user or manufacturer. A larger circle of confusion will produce an image that appears blurrier than one with a smaller circle of confusion.

It is worth noting at this juncture the difference between the terms focal length (f) and focus distance (x) in this discussion. Focal length is a property of the lens and is the distance from the lens center to where it focuses rays of light that are orthogonal to the lens vertical midline. The focus distance is the distance between the lens and a subject that is perfectly in focus, which is to say the circle of confusion has essentially zero size. Figure 2.3 illustrates the focal length (f), focus distance (x), and circle of confusion (c).

Given a maximum permissible circle of confusion it is possible to compute the depth of field (DOF) of a camera. The depth of field is the range of subject distances that will have a circle of confusion smaller than the maximum circle of confusion. That is, a subject in the depth of field of the camera can be brought into an acceptable level of focus. The DOF spans between a near limit (D_n) and a far limit (D_f). The focus distance will lie somewhere between these two limits (i.e. in the DOF).

To maximize the field of view, the focus distance is made the same as the hyperfocal distance (H) of the camera. Put another way, the hyperfocal distance is the focus distance that produces an infinite far limit on the DOF. The hyperfocal distance is given by the equation [31]:

$$H = \frac{f^2}{Nc} + f \tag{2.11}$$

In which H is the hyperfocal distance in m, N is the f-number or relative aperture of the lens, c is the circle of confusion in m, and f is the focal length in m as before. Depth of field limits are given by the equations [31]:

$$D_n = \frac{xf^2}{f^2 + Nc\,(x - f)} = \frac{x\,(H - f)}{H + x - 2f} \tag{2.12}$$

$$D_f = \frac{xf^2}{f^2 - Nc\,(x - f)} = \frac{x\,(H - f)}{H - x} \tag{2.13}$$

In which D_n and D_f are the near and far depth of field limits, respectively, in m, x is the focus distance in m, and f is the focal length in m. The depth of field itself is then given by:

$$DOF = D_f - D_n \tag{2.14}$$

In the case that $x = H$, the equation for the near limit can be expressed as:

$$D_n = \frac{H}{2} \tag{2.15}$$

All of these distances and concepts are visualized for a simple lens in Figure 2.3.

In terms of blur caused by out-of-focus images, the circle of confusion adequately describes this phenomenon. If the circle of confusion is the size of one pixel on the image sensor, then assuming one pixel of additional blur is a conservative estimate of this type of blur.

On a zoom (or varifocal) lens, the focus distance can be changed by changing the focal

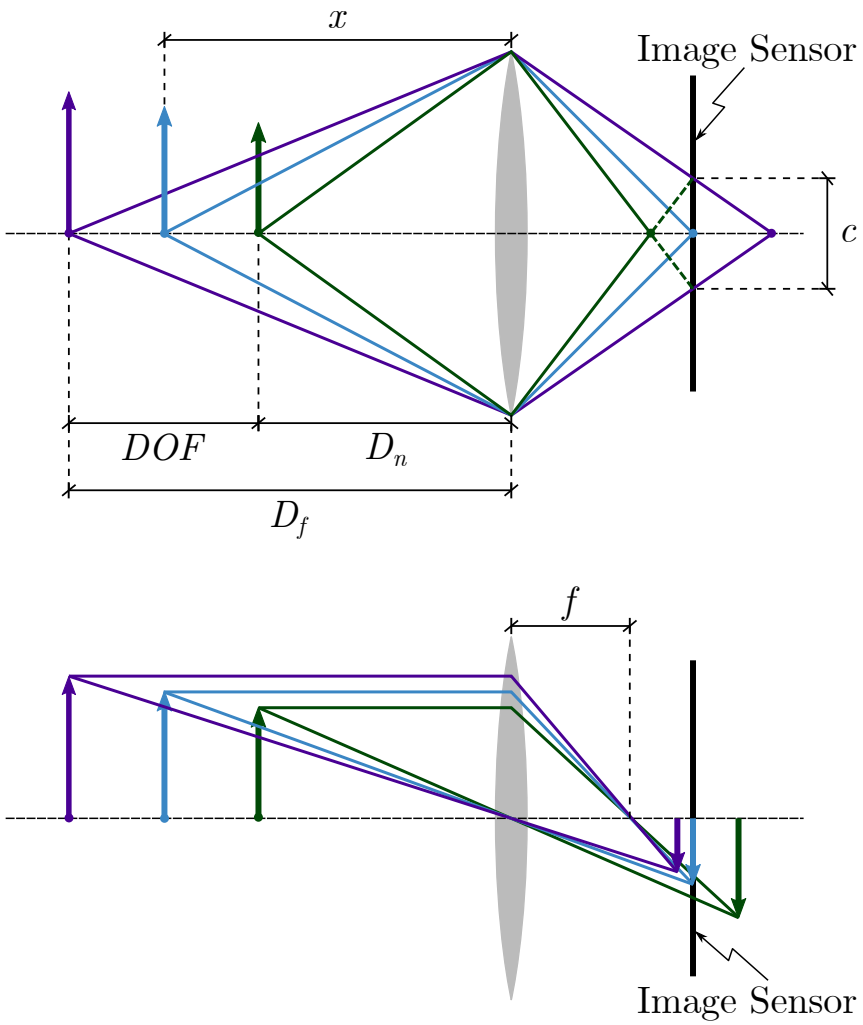

Figure 2.3: DOF (DOF), COC (c), focal length (f), and focus distance (x) for a thin lens.

length. For a UAV with a camera that is a roughly constant distance from a concrete surface, this means that a zoom lens with an adequate range of focal lengths can adjust to a particular subject distance to ensure it is acceptably in-focus. A zoom lens should be selected such that the DOF is large enough to accommodate small variations in camera–subject distance caused by unintended motion of the UAV.

However, the camera of the P3S is a prime lens, not a zoom lens. For a prime lens such as the one found on the P3S, the focal length, f, and focus distance, x, are fixed. In order to make images always appear in-focus (i.e. to keep just about everything in the DOF), the far limit of many prime lenses is near infinity. While this is perhaps the case with the P3S camera, its COC and DOF specifications are proprietary and not published by the manufacturer.

If the DOF or COC were reported for the P3S, it would be possible to suggest a precise minimum distance for adequate focus of images. However, by choosing a COC and assuming it has a focus distance that is roughly the hyperfocal distance, the other camera details can suggest a minimum distance.

Using the properties of the P3S camera, a COC of two pixels (0.0031 mm) or less indicates a hyperfocal distance of 1494 mm (by Eq. 2.11), and a near limit for DOF of 747 mm (via Equation 2.15):

$$H = \frac{f^2}{Nc} + f = \frac{3.61^2}{2.8 \cdot 0.0031} + 3.61 = 1494 \text{ mm}$$

$$D_n = \frac{H}{2} = \frac{1494}{2} = 747 \text{ mm}$$

A similar procedure with the steps reversed could be used with a desired minimum distance to compute the largest COC that could be expected.

2.1.4 Image sensor: a note on potential issues with sensor size and image resolution

It is worth noting that the mathematical relationships and procedures described in this chapter assume use of the full image sensor. However, cameras are capable of recording images at less than the full image sensor pixel resolution. For example, video frames are often recorded with a pixel resolution lower than that of the camera sensor.

The actual physical size of the image formed on the sensor by the projection of the subject depends on the optics of the camera lens and distance to the subject. However, if only part of the sensor is being used, it is possible that the way the image is recorded in pixels will be changed. The maximum FOV in the recorded image may also be changed.

As a simple example, if in Figure 2.3 the image sensor used a portion in the middle that was shorter than the blue image projected, a portion of the arrow would be omitted from the image.

In the absence of detailed information from the manufacturer on how a particular camera sensor is being used to take images or video which have a resolution lower than that of the full image sensor pixel resolution, some tests on sample images with known

values may be required to evaluate the accuracy of the equations presented in this section. Some cameras may use capture methods, storage techniques, and file formats that lose information or create artifacts. Of course, images that have a resolution higher than that of the image sensor are also cause for concern.

2.1.5 Flight strategy sample calculation

An example calculation helps to illustrate the use of Sections 2.1.2 and 2.1.3 in the formulation of a basic flight strategy for a bridge inspection.

Assume a bridge inspection is required for a bridge with a concrete deck and support structure. The sides of the deck are to be imaged by a DJI Phantom 3 Standard UAV. The P3S camera has and aircraft have the properties shown in Table 2.1. The bridge is 500 m in length, and both sides need to be imaged by the P3S.

Suppose that cracks with a width of 5 mm or more are of interest. The cracks are to be at least 9 pixels in the images. The acceptable blur in the cracks is to be no more than 3 pixels. Note that these values are purely for illustration and are not necessarily representative of any specific real-world bridge. Values for minimum crack width and acceptable blur for a real-world structure are at the discretion of the flight planner and image analyst. Using this information and Procedure 2.1, the following computations can be performed. Starting with Eq. 2.10:

$$d = f\left(\frac{h_{o,m}}{h_{i,px}}\frac{s_{s,px}}{s_{s,m}} + 1\right) = 0.00361\left(\left(\frac{0.005}{9}\right)\left(\frac{4000}{0.00616}\right) + 1\right) = 1.3059 \text{ m}$$

Now, letting $D_n = d$ and assuming $H = 2 \cdot D_n$ as in Eq. 2.15, the COC can be estimated using a rearranged Eq. 2.11:

$$c = \frac{f^2}{N\left(H - f\right)} = \frac{0.00361^2}{2.8\left(2.6118 - 0.00361\right)} = 1.7845 \times 10^{-6} \text{ m} \approx 0.002 \text{ mm}.$$

$$c = 1.7845 \times 10^{-6} \text{ m} \cdot \frac{4000 \text{ px}}{0.00616 \text{ m}} = 1.1588 \text{ px}$$

This means the blur due to motion is to be no more than 1.8412 pixels, meaning the velocity of the flight can be estimated using a rearranged Eq. 2.6b:

$$v = \frac{b_{px}}{t}\frac{s_{s,m}}{s_{s,px}}\left(\frac{d - f}{f}\right) = \left(\frac{1.8412}{1/8000}\right)\left(\frac{0.00616}{4000}\right)\left(\frac{1.1757 - 0.00361}{0.00361}\right) = 8.1833 \text{ m/s}$$

So for the specified crack sizes and blur, the operation should take place at a speed of no more than about 8.2 m/s at a distance of about 1.3 m from the concrete surface. For both sides of the bridge, this operation should take about 2 minutes from start to finish. Results of calculations with the same parameters but a variety of crack widths are shown in Table 2.2.

Table 2.2: Optical strategy sample calculations for a variety of crack widths.

Min. Crack Width [mm]	**Max. Subject Distance [m]**	**Max. Inspection Velocity [m/s]**
2	0.5	0.2
5	1.3	8.2
8	2.1	16.2
10	2.6	21.5

The results in the table indicate that the camera configuration used is unsuitable for smaller cracks and better suited to larger cracks. The subject distance is actually the limiting factor in this case for this camera. With the selected parameters (how large the crack is in the image and the acceptable level of blur), the camera cannot get close enough to the sample to make small cracks (less than 2 mm) large enough in the image while maintaining adequate focus.

2.2 Distance and crack width estimation utility

A simple MATLAB®-based distance and crack width utility was developed for use with the DJI Phantom 3 Standard. Two test samples with induced cracks of widths ranging from 0.5 mm to 5 mm were imaged by both the Phantom 3 Standard camera during a test flight and a stationary handheld Sony DSC-W570 digital camera from the ground for reference. The effect of velocity change is not effectively gauged using the distance utility.

The utility works by performing the spatial calibration (i.e. the distance calculation) and then using this information combined with simple black and white image thresholding to estimate crack width (CW). A detailed instruction document regarding the use of the image utility as well as the MATLAB script are included in Appendix A. Spatial calibration

of the MATLAB® utility uses a code implementation developed and published online as a sample by a MATLAB® user [32]. The distance and crack utility does not use code verbatim from this sample. The images are individually manually thresholded to detect dark areas (cracks) and lighter areas (normal concrete surface). In this process light areas of the image are converted to white pixels and dark areas to black pixels. All images were taken outdoors during daylight hours on a sunny day in August 2017 at UVic's Civil Engineering Materials Test Facility. The utility uses thresholding to identify cracks on the concrete surface, so adequate lighting conditions such as those offered by the bright daylight are required. The top of each image is oriented perpendicularly to the Northeast (i.e. a vertical line in the image from top to bottom runs from Northeast to Southwest).

No camera calibration was performed on the DJI Phantom 3 Standard camera or the Sony DSC-W570 camera prior to the start of testing. While lens aberrations or distortions are not considered by the utility or in this example, geometric camera calibration could be used to estimate lens distortion (both radial and tangential) as well as offer an estimation of camera intrinsics and extrinsics [33].

The distance to the crack surface and the width of the crack was computed for each image at three locations on each sample. The distance calculation uses Equation 2.5 and the crack width calculation uses Equation 2.9a. The distance to the surface of the sample with the crack was recorded using a tape measure for the Sony DSC-W570 images to estimate the effectiveness of the distance estimation algorithm. The crack measurements were taken at the top, middle, and bottom of the samples, in the areas highlighted in Figure 2.4 below:

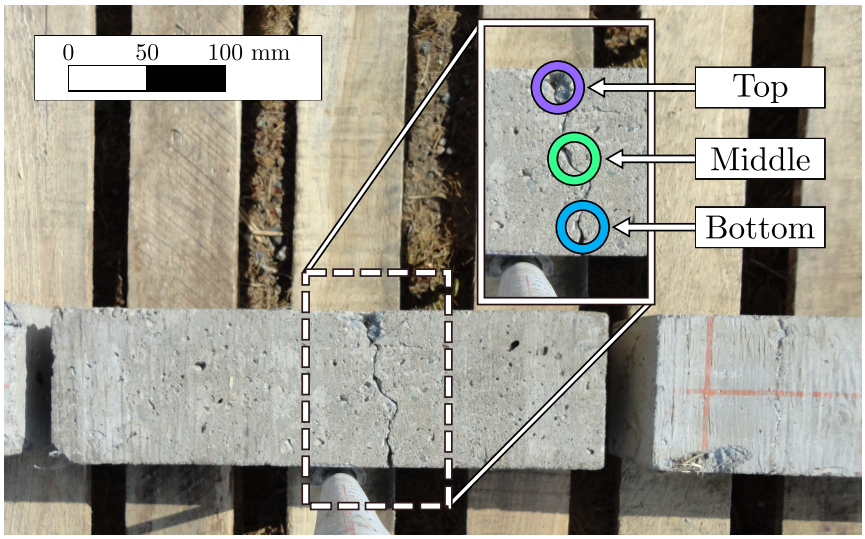

Figure 2.4: Location of top, middle, and bottom measurements on a sample.

Both the P3S and Sony DSC-W570 images were taken at four heights. The Sony DSC-W570 images were recorded at measured heights 0.5 m, 1.0 m, 1.5 m, and 2.0 m from the concrete surface. The P3S images were taken in-flight at four heights over the course of four passes above the concrete surface. The heights of these passes (numbered 1 through 4) were roughly comparable to the distances of the Sony images, but due to the limited accuracy of flight navigation, some deviation from these nominal heights for the P3S was observed. The P3S images are still images taken from a video of the test flight. The P3S camera can take stills at no less than 1 second intervals, so stills from a video taken at 30 frames per second are preferable when using this aircraft.

Cropped versions of all images used during the analysis are shown in Appendix A. The actual crack widths were measured using a crack width gauge card to the nearest 0.25 mm. The results of the calculated crack widths (CWs) and distances are shown in Tables 2.3, 2.4, and 2.5.

Table 2.3: Crack distance and width evaluated at the top of each crack.

Figure/ (Sample)	**Camera**	**Pass No. or nominal dist. [mm]**	**Calculated distance [mm]**	**Actual CW [mm]**	**Calculated CW [mm]**	**CW percent error [%]**
A.1a/(1)	P3S	Pass 3	476	1.0	1.208	20.8
A.1b/(1)	P3S	Pass 4	904	1.0	1.086	8.6
A.1c/(1)	P3S	Pass 1	1039	1.0	0.8833	11.7
A.1d/(1)	P3S	Pass 2	1920	1.0	1.635	63.5
A.3a/(1)	Sony	500	494	1.0	0.9207	7.9
A.3b/(1)	Sony	1000	966	1.0	1.144	14.4
A.3c/(1)	Sony	1500	1431	1.0	0.8487	15.1
A.3d/(1)	Sony	2000	1962	1.0	1.147	14.7
A.2a/(2)	P3S	Pass 3	541	5.0	4.721	5.6
A.2b/(2)	P3S	Pass 4	874	5.0	3.714	25.7
A.2c/(2)	P3S	Pass 1	1028	5.0	5.249	5.0
A.2d/(2)	P3S	Pass 2	1985	5.0	4.782	4.4
A.4a/(2)	Sony	500	484	5.0	3.423	31.5
A.4b/(2)	Sony	1000	974	5.0	3.650	27
A.4c/(2)	Sony	1500	1464	5.0	3.473	30.5
A.4d/(2)	Sony	2000	1914	5.0	3.409	31.8

Table 2.4: Crack distance and width evaluated at the middle of each crack.

Figure/ (Sample)	**Camera**	**Pass No. or nominal dist. [mm]**	**Calculated distance [mm]**	**Actual CW [mm]**	**Calculated CW [mm]**	**CW percent error [%]**
A.1a/(1)	P3S	Pass 3	475	1.0	1.207	20.7
A.1b/(1)	P3S	Pass 4	904	1.0	0.7681	23.2
A.1c/(1)	P3S	Pass 1	1040	1.0	0.8844	11.6
A.1d/(1)	P3S	Pass 2	1911	1.0	1.628	62.8
A.3a/(1)	Sony	500	493	1.0	1.163	16.3
A.3b/(1)	Sony	1000	965	1.0	1.144	14.4
A.3c/(1)	Sony	1500	1434	1.0	0.8509	14.9
A.3d/(1)	Sony	2000	1937	1.0	1.150	15.0
A.2a/(2)	P3S	Pass 3	541	2.0	2.295	14.8
A.2b/(2)	P3S	Pass 4	864	2.0	2.202	10.1
A.2c/(2)	P3S	Pass 1	1028	2.0	2.763	38.2
A.2d/(2)	P3S	Pass 2	2005	2.0	2.414	20.7
A.4a/(2)	Sony	500	486	2.0	2.432	21.6
A.4b/(2)	Sony	1000	974	2.0	2.449	22.5
A.4c/(2)	Sony	1500	1467	2.0	2.462	23.1
A.4d/(2)	Sony	2000	1914	2.0	2.273	13.7

Table 2.5: Crack distance and width evaluated at the bottom of each crack.

Figure/ (Sample)	**Camera**	**Pass No. or nominal dist. [mm]**	**Calculated distance [mm]**	**Actual CW [mm]**	**Calculated CW [mm]**	**CW percent error [%]**
A.1a/(1)	P3S	Pass 3	475	0.5	0.9002	80.0
A.1b/(1)	P3S	Pass 4	904	0.5	0.7681	53.6
A.1c/(1)	P3S	Pass 1	1039	0.5	0.8833	76.7
A.1d/(1)	P3S	Pass 2	1907	0.5	0	100
A.3a/(1)	Sony	500	494	0.5	0.5828	16.6
A.3b/(1)	Sony	1000	967	0.5	0.5728	14.6
A.3c/(1)	Sony	1500	1441	0.5	0.8551	71.0
A.3d/(1)	Sony	2000	1919	0.5	1.139	127.8
A.2a/(2)	P3S	Pass 3	541	0.5	0.9172	83.4
A.2b/(2)	P3S	Pass 4	864	0.5	1.038	107.6
A.2c/(2)	P3S	Pass 1	1030	0.5	0.8759	75.2
A.2d/(2)	P3S	Pass 2	1990	0.5	0	100.0
A.4a/(2)	Sony	500	487	0.5	0.5737	14.7
A.4b/(2)	Sony	1000	976	0.5	0.5782	15.6
A.4c/(2)	Sony	1500	1456	0.5	0.8640	72.8
A.4d/(2)	Sony	2000	1908	0.5	1.133	126.6

From the distances calculated for the Sony DSC-W570, the average percent error between the measured and calculated distances is just 3.1 %.

Due to the small sample size of data available, it is not possible to make statistically significant generalizations regarding the performance of the crack estimation. However, it is still possible to note that there is a general trend towards lower percent error between the actual and calculated crack widths as the width of the cracks increase. Given the closeness of the actual distances to computed distances, it is likely that the computed ratio of image pixels to actual distance in the plane of the crack (i.e. the concrete surface) is accurate.

The reason for some of the high errors for the narrow crack widths in particular appears to be a lack of adequate resolution in the image itself. Some of the 0.5 mm and 1.0 mm cracks are only two or three pixels across. While each pixel can be computed to a precise real width in mm, if a crack width would naturally lie in a real distance range between that of two pixels, the image only captures the information at the pixel level, and it is either "rounded" down or up depending on the thresholding used for the particular image and the exact amount of the crack occupying the pixel. For example, if a pixel width spans 0.3 mm in the plane of the actual crack, then a crack that is actually 0.45 mm will likely be calculated as either 0.3 mm, or 0.6 mm depending on the thresholding of the pixels involved.

Overall, this investigation into a distance utility illustrates a critical link between the size of the crack, resolution of the image, and distance between the camera and subject.

Chapter 3

UAV-based infrared thermography of concrete structures

3.1 Infrared thermography as a tool for concrete and bridge inspection

Infrared thermography is well-established as a tool for non-destructive bridge inspections. ASTM D4788 which details a "Standard Test Method for Detecting Delaminations in Bridge Decks Using Infrared Thermography" has existed in some form since 1988 [34]. More recent work by Sultan and Washer [35] confirms quantitatively the reliability of infrared thermography in locating shallow delaminations in concrete.

The use of infrared thermography from a UAV-based platform for concrete and bridge inspection is a more recent application. Optical imaging of infrastructure or concrete from UAVs is more common, but limited information on infrared is available. A 2015 report by the Minnesota Department of Transportation [26] demonstrated use of a infrared imaging during a bridge inspection to image the bridge deck. However the Minnesota study used a bridge without any observed delaminations or other defects, so the ability of the infrared thermography to detect defects in an actual bridge was not addressed.

Most infrastructure inspection that makes use of infrared thermography does so using a passive approach, which is to say that the infrared images capture the temperature differences in a structure or object that arise as a result of environmental conditions.

An exploratory study by Mavromatidis et al. [36] evaluated the use of active infrared thermography with a UAV. Essentially, this study used a flash heating technique to induce a temperature response in the inspection material, a composite plate. However, the approach of the Mavromatidis et al. study has not yet been investigated on bridges or concrete.

UAV-based passive infrared imaging of a mock bridge deck with induced delaminations was demonstrated by Ellenberg et al. [25]. This study showed that UAV-based infrared thermography is capable of detecting and (in combination with adequate post-processing techniques) of estimating delamination area.

3.2 Infrared imaging of voids and delaminations in concrete test specimens

3.2.1 Specimens, equipment, and test conditions

The test specimens outlined in Section 4.2 contain delaminations and voids in a concrete slab. A thermal camera-equipped UAV was used to obtain infrared images of the slabs. The slabs were located in an open-air lot on a dirt-base sparsely populated with local vegetation. The upper slab surfaces were uncovered and exposed to the local environmental conditions.

A DJI Phantom 3 Standard (P3S) modified to carry an infrared camera was the UAV used for all experiments. An image of the modified UAV in-flight is shown in Figure 3.1. Test flights were conducted above the slabs at a variety of altitudes below 50 feet ($\approx$ 15 m).

The infrared images were collected using a FLIR Vue Pro 640 model thermal camera with 19 mm lens and 30 Hz video capability. It is capable of taking video and stills at a maximum resolution of 640 $\times$ 512 pixels. An image of this thermal camera mounted to the PS3 is shown in Figure 3.2. This camera is not radiometric, meaning it is capable only of distinguishing between regions of different temperature and is not able to accurately gauge the temperature in degrees centigrade (or any other temperature scale). For the tests performed, distinguishing between regions of temperature difference is adequate to detect and locate defects embedded in the concrete.



(a)



(b)

Figure 3.1: The Phantom 3 Standard mid-flight showing (a) the concrete slab specimens in the background, and (b) the FLIR Vue Pro attached to a custom mounting plate. Images © 2017 Armando Tura, used with permission.

Infrared images were captured at full 640 × 512 resolution at a 1 second interval in 8-bit JPEG format.

Infrared imaging was conducted on 22 September 2017. The lot on which the slabs were located is on the University of Victoria campus adjacent to parking lot 7 and the UVIC Civil Engineering Materials Facility. Tests were conducted between 13:00 and 14:00 hours Pacific Daylight Time, at which time climate records for the UVIC indicate a temperature

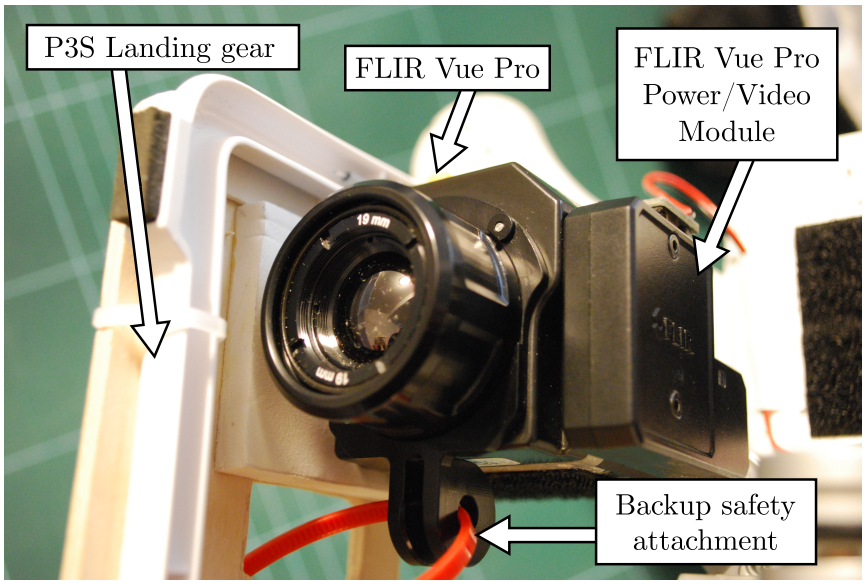

Figure 3.2: The FLIR Vue Pro as mounted on the P3S.

around 17–18°C and generally clear skies with few clouds. The specimens received in excess of three hours of direct sunlight prior to the tests (during which time the reported temperature ranged between 15 and 17°C), and reported wind was less than 10 km/h for the duration of all data collection. The slabs were dry for in excess of 24 hours prior to the tests. Images were collected by positioning the aircraft above the slabs and keeping it roughly stationary for a period of several seconds, so data was not collected at speed. These experimental parameters are compatible with relevant points of the procedure in ASTM D4788 – 03 [34] for infrared thermography of bridge decks (although the slabs are not a perfectly accurate representation of a bridge deck). ASTM D4788 – 03 [34] also requires defect locations are subsequently verified using sounding or other methods, performed as described in Section 4.2 and 4.3.

3.2.2 Infrared imaging results

A collection of infrared images showing each of the seven slabs is shown in Figure 3.3. Slabs and defects in Figure 3.3 are numbered and oriented as per the convention in Figure 4.5. The images have been cropped so the slabs occupy the majority of the frame, but some show clipped corners as a result. Original IR images as well as other images showing the slabs are shown in Appendix B. The defect depths as measured by slab drilling are recorded in Table 4.1 in Section 4.2.

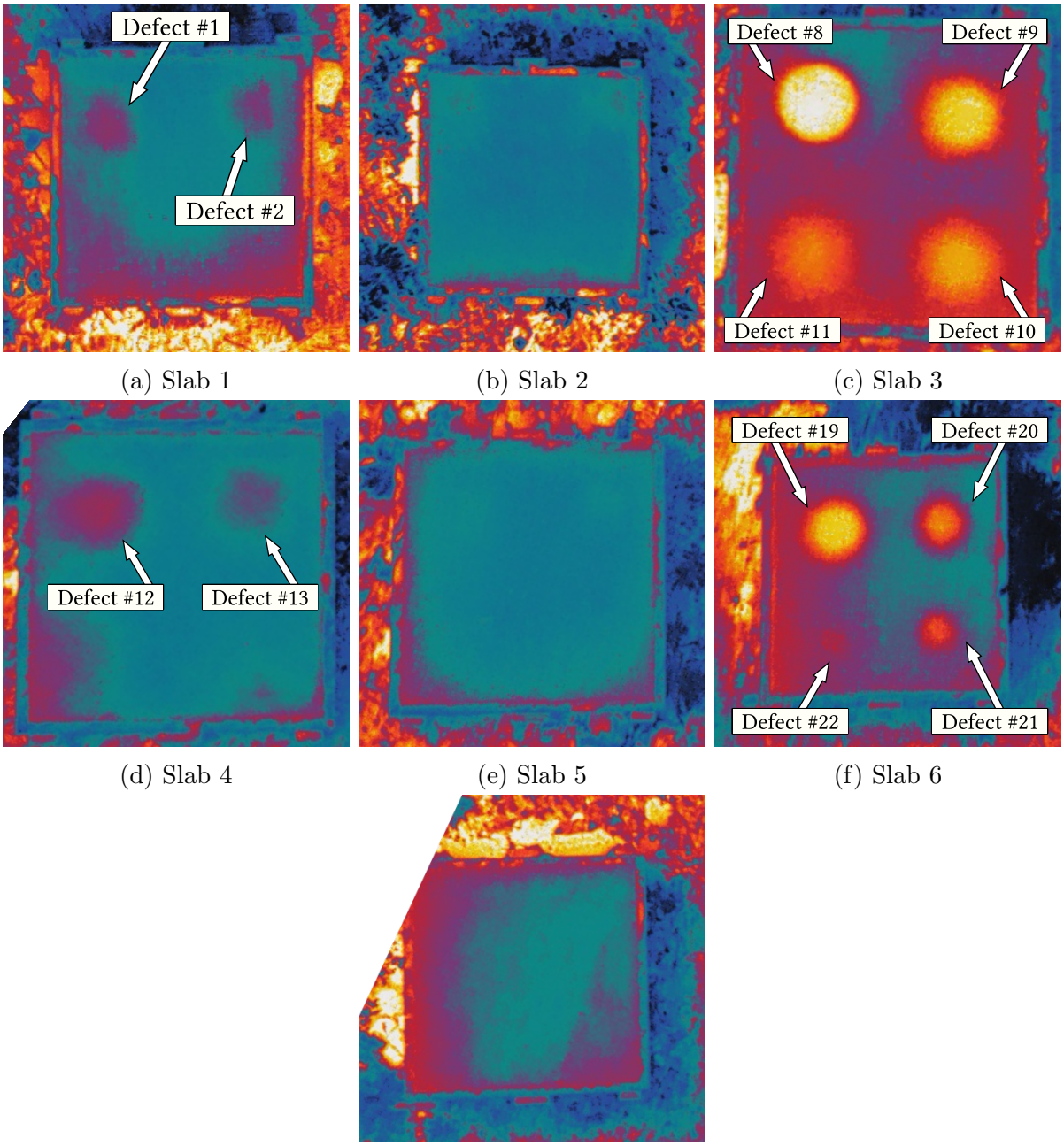

(a) Slab 1 (b) Slab 2 (c) Slab 3

(d) Slab 4 (e) Slab 5 (f) Slab 6

(g) Slab 7

Figure 3.3: Infrared images of each slab.

As shown in Figure 3.3, defects number 1, 2, 8, 9, 10, 11, 12, 13, 19, 20, 21, and 22 can be easily observed in the infrared images. The remaining defects are not seen in the infrared images. The defects that do not show up on the surface are those that are located deepest in the slabs. Of the defects that were detected, those closest to the surface show the greatest temperature difference, and those located deeper show less temperature difference. The edges of the thermally distinct areas corresponding to defects are also

sharper for shallower defects. Compare, for example, defects 8 and 11 in slab 3. The area corresponding to defect 8 transitions much more suddenly at its border than the border of defect 11, which shows a more gradual transition. The shallower defects also show a greater magnitude of temperature difference relative to their deeper counterparts.

From the image of slab 6, the decreased lateral defect size appears to have a similar effect to increased depth from the surface. Though located at similar depths, defects 19 and 22 are show drastically different edge profiles that cannot be explained by the lower number of pixels for the smaller defect.

A larger sample size would be required to make any statistically significant mathematical conclusions regarding detectability, but in general defects with lower depth to lateral size ratios are most prominent in the thermal images.

Table 3.1: Thermal image defect size estimates.

Defect Number	**Measured Depth [mm]**	**Nominal Lateral Size [mm]**	**IR-image Lateral Size Estimate [mm]**	**Percent Error [%]**
1	39	203	178	12.3
2	49	203	147	27.6
8	15	254	244	3.9
9	27	254	244	3.9
10	43	254	241	5.1
11	53	254	241	5.1
12	60	254	283	11.4
13	73	254	202	20.5
19	27	254	256	0.8
20	28	203	221	13.0
21	28	152	165	8.6
22	42	102	103	1.0

Using the edges of the slabs as a reference length, the lateral size of the defects can be estimated. A summary of estimated defect lateral size and actual defect lateral size are shown in Table 3.1. Some defects ended up not completely parallel to the concrete surface (i.e. one part of the embedded foam or plastic plate used to simulate the defect is at a different depth that the other). As such, the lateral size when viewed from a roughly parallel plane, as in the case of the UAV-based thermal camera above the slabs for these images, will be the projection of the actual size in a parallel plane, which will result in some

variance in the nominal defect size, which may explain some of the discrepancies shown in Table 3.1.

3.2.3 Infrared imaging conclusions

As in Ellenberg et al. [25], subsurface defects embedded in a concrete test slab are shown to be detectable. The lateral size of the defects detected can be estimated from the infrared images of the slabs with reasonable accuracy. In thermal images, shallower defects appear more clearly and with more well-defined edges than defects located farther from the surface. Defects with a larger lateral size also appear more prominently than those with smaller lateral dimensions. In general, this would indicate that there may exist some relationship between defect lateral size to depth ratio and defect detectability or edge clarity, which is agreement with work performed by Hiasa et al. [37]. Though not statistically significant, indications from the slabs imaged indicate that the larger the ratio of lateral size to depth, the greater the contrast between the defective area and the surrounding area. Similarly, larger lateral size to depth ratios on the slabs imaged correspond to sharper edges between the defective and non-defective areas.

Chapter 4

Sounding of subsurface concrete defects using frequency response of flexural vibration

This chapter is the accepted version of a paper published in the Elsevier journal Cement and Concrete Composites [38]:
Sean Blaney and Rishi Gupta. Sounding of subsurface concrete defects using frequency response of flexural vibration. *Cement and Concrete Composites*, 92:155–164, September 2018. ISSN 0958-9465. doi:10.1016/j.cemconcomp.2018.06.006

In this paper, existing acoustic inspection methods that make use of the vibrational properties of a concrete specimen that contains a delamination or void defect are evaluated. A novel speaker-based excitation setup is shown to be nearly as effective as an established chain link-based technique, though slightly less effective than an established hammer-based method. Factors affecting the speaker-based method are demonstrated. The effect of defect depth on detectability is observed.

A chapter-specific nomenclature section has been added to avoid ambiguity between chapters. The nomenclature presented is exclusively applicable to this chapter.

Abstract

Standard sounding procedures such as hammer percussion and chain drag can be used to locate subsurface concrete defects, but are often subject to the individual judgement and ear of trained inspectors. However, defect depth information can be difficult to gauge by ear alone. By recording audio and analyzing the frequency content of sounding via hammer percussion, a single- and triple-link chain drag, and a novel speaker-based excitation procedure, simulated defects in concrete test slabs were detected. The speaker-based method shows the capacity to detect a similar number of defects as chain drag methods, though it is slightly less effective than the hammer method. The duration and type of the acoustic signal used by the speaker to induce vibration are important factors in performance of the speaker-based method. The detectability of a defect via all methods tested depended largely on the ratio of defect depth to defect lateral dimensions; defect detectability was shown to drop after this ratio exceeded about 0.35.

Nomenclature

β	dimensionless frequency parameter (circular plate)	a	circular plate radius
λ	dimensionless frequency parameter (square plate)	b	square plate side length
ν	Poisson's ratio	D	plate flexural rigidity
ρ	mass density of plate	E	dynamic elastic modulus
ω	thick plate angular frequency	f	frequency of vibration
ω_0	thin plate angular frequency	h	defect depth (equivalent to plate height)

4.1 Introduction

4.1.1 Problem Statement

Sounding of concrete via a variety of impactors including coins [39], steel spheres [40], hammers [41], and steel chain [17] has been shown to be capable of detecting defect locations. The depth of the defect can be estimated using a frequency analysis of the recorded contact or non-contact measurement of the response [39, 40, 42]. The work described herein assesses the relative performance of three readily-available impactors (hammer, chain, and speaker) in detecting voids and delaminations in concrete specimens. While hammer-based and chain-based excitation for concrete sounding are well established, speaker-based excitation for concrete sounding using microphones is unexplored. All three methods are low-cost, but the ability to accurately control and change the contact time between a speaker and the concrete surface it excites using different acoustic signals is a feature not available to hammer or chain-based methods (which require a new impactor of a different size altogether to change impact time).

4.1.2 Concrete Sounding Background

Several standard methods for sounding concrete to detect delaminations are outlined by ASTM D4580/D4580M – 12 [2], including a chain drag procedure, which may be performed with an actual chain dragged over the concrete surface or with hammer-based tapping. This

standard specifies that the detection of delaminations occurs by the operator of the test noting dull or hollow sounds [2]. This procedure is subject to the ability of the operator to identify and make note of the sound of the defect-laden concrete. The depth of the defect can be difficult to detect by ear. A hammer percussion test may be said to be a type of coin tap test that uses a hammer as the impactor [1].

To remove the subjectivity of operator variance from the tests, the sound of the impact can be recorded by a microphone and the frequency content of the acoustic recording is used to identify defects. Sun, Zhu, and Ham [17] used a microphone to record the response of the concrete for a chain drag test [17]. A hammer percussion test using a microphone to record the sound of the impact has been shown by Wu and Siegel [41] to be roughly as effective as a contact force-based measurement of the vibration response in detecting problem areas in an aircraft skin specimen. Asano, Kamada, Kunieda, and Rokugo [42] demonstrated use of a microphone and digital audio card on concrete specimens. The use of a hammer sounding technique for Pavement was demonstrated by Felicetti [43]. Cheng, Cheng, and Chiang [39] showed coin tapping recorded using a microphone could be used to detect voids in concrete specimens.

When excited by an impact, concrete of a plate-like shape will vibrate prominently in thickness and flexural modes [44]. Concrete defect detection by sounding uses the concept that waves travelling in the concrete are reflected at a planar air-concrete interface due to the low specific acoustic impedance of air. The impact-echo method takes advantage of this reflection of thickness mode vibration waves to detect voids [44]. For the sounding tests performed in this study, rather than measuring the vibration at the concrete surface as in the impact-echo method prescribed by ASTM C1383 – 15 [3], the concrete vibration is recorded via the reflected wave in the air in a manner similar to an air-coupled impact echo procedure such as the one described by Zhu and Popovics [15]. However, the methods of excitation used in this study (the hammer, chain, and speaker) produce contacts with the concrete specimens that have longer contact times in comparison to those involved in an air-coupled impact echo test. As longer contact times limit the maximum useful frequencies of the tests [45], flexural frequencies of vibration, which are lower than thickness mode vibration frequencies, should be the most prominent modes of vibration found in the audio recordings. That is, frequency peaks associated with the flexural modes of vibration will be the most prominent in the amplitude spectrum of the fast Fourier transform of the recorded acoustic signals.

Haya, Luo, and Uomoto [46] used an impact acoustic method coupled with wavelet

analysis to observe the early part of the response signal to characterize defect strength and defect detection, and found the dominant frequency component over the total signal duration to characterize the boundary conditions or defects inside a specimen. Felicetti [43] observed a vibration of the impact device in the later part of the response signal recorded by the microphone, and used comparison of the frequency spectrums between damaged and undamaged pavement as a basis for defect detection. A similar but more cursory comparison forms the basis of defect detection in this work.

4.1.3 Expected flexural frequency peak

The relationship between the resonant frequency peaks associated with flexural vibration and the depth of a defect or thickness of a plate depend on the lateral size, shape, and boundary conditions of the plate [40]. In the case of acoustic sounds above the location of a planar void or delamination defect in concrete, plate thickness is the depth of the defect. In this study, the actual concrete above the defects is restricted or damped along the bottom surface to some degree by the foam (in the case of simulated voids) or plastic (in the case of simulated delaminations). Approximation of boundary conditions in the theoretical treatment of the concrete above a simulated defect to simplify calculation of expected flexural frequency peaks was used by Cheng and Sansalone [40], with simply supported boundary conditions.

Given concrete properties, lateral dimensions, plate depth, the expected frequency of vibration can be computed using closed form solutions for vibrating plates or finite element analysis. The appropriate dimensions for the specimens used in this study are shown in Figure 4.1. The defect depth is shown as h, the lateral size of delaminations is shown as b, and the diameter of the voids is shown as $2a$.

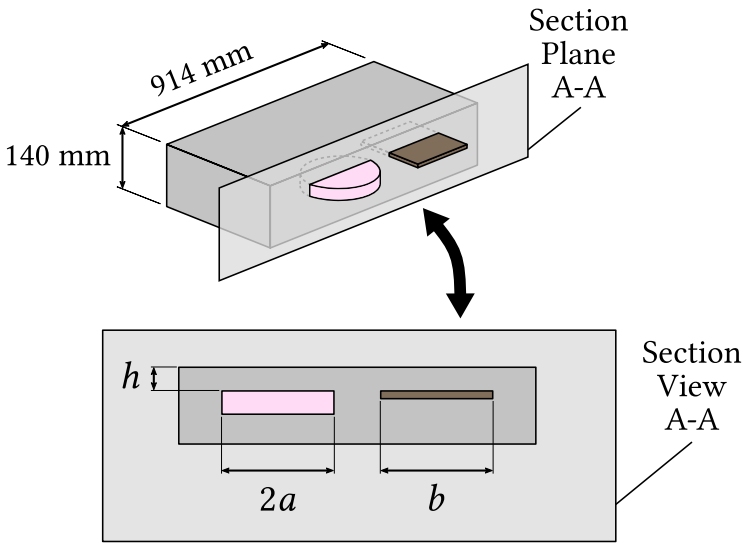

Figure 4.1: Slab defect depth and lateral size for voids (left) and delaminations (right).

Thus, the depth of a defect is the thickness of the plate of concrete that rests on top of a defect. Only the fundamental modes of vibration are considered. Impacts occur roughly over the center of defect locations, so fundamental frequencies should have the largest amplitude [40]. Higher modes of vibration are also likely to be recorded as the impact will likely not be perfectly centered. The equations used to relate the defect depth to the frequency for a thin square plate clamped on all sides are shown in a form similar to that of Leissa [52]:

$$\lambda = 2\pi f b^2 \sqrt{\frac{\rho h}{D}} \tag{4.1}$$

$$D = \frac{E h^3}{12\left(1-\nu^2\right)} \tag{4.2}$$

In which λ is a dimensionless frequency parameter that depends on boundary conditions, mode of vibration, and plate thickness ratio, f is the frequency of vibration in Hz, b is the side length of the square plate in m, ρ is the mass density of the plate in kg/m^3, h is the thickness of the plate in m, D is the plate flexural rigidity in N·m, E is the dynamic elastic modulus in Pa, and ν is the Poisson's ratio. Leissa [52] offers a value of $\lambda = 35.998965$ for a thin plate only. A plot by Nelson [47] offers a range of normalized angular frequency ratios (ω/ω_0) as a function of thickness to side ratio (h/b) that can be used to obtain estimates of the expected frequencies for the range of plate thicknesses used in this study. This plot is shown in Figure 4.2.

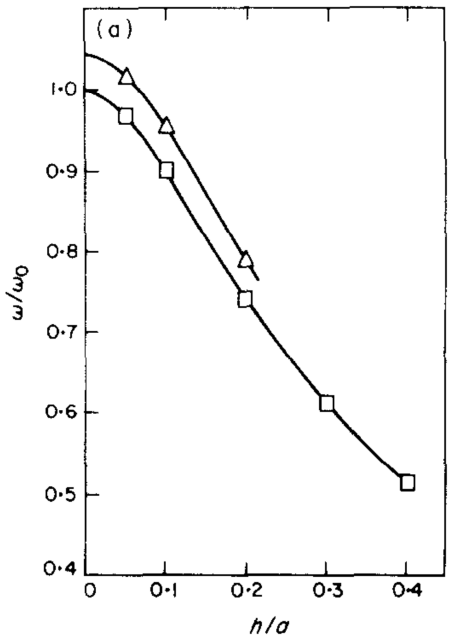

Figure 4.2: The plot used to estimate h/b from Nelson [47]: "Normalized frequency, ω/ω_0, as a function of thickness-side ratio for a square (C-C-C-C) plate. □, Present approximation; △ Cheung and Chakrabarti results. (a) m = 1, n = 1."[1]

In the plot shown in Figure 4.2, the square-box "present approximation" is the curve used for all estimations of ω/ω_0. The angular frequency for a thin plate with $h/b = 0$ is ω_0, and the angular frequency at h/b up to 0.4 can be estimated. A frequency computed using Equation 4.1 must be multiplied by the appropriate ω/ω_0 ratio obtained using Figure 4.2 according to the h/b ratio. The h/a in Figure 4.2 is equivalent to h/b in the terminology used in this work.

The equations for circular plates are also presented in a form similar to that used by Hosseini-Hashemi, Es'haghi, Taher, and Fadaie [48]:

$$\beta = 2\pi f a^2 \sqrt{\frac{\rho h}{D}} \tag{4.3}$$

In which β is a dimensionless frequency parameter, and a is the circle radius in m. To obtain values for β, Hosseini-Hashemi, Es'haghi, Taher, and Fadaie [48] offer a host of values for clamped circular plates.

These equations can be used to compute either a defect depth given a measured frequency, or an expected frequency from a measured depth. In order to do so, knowledge

[1]Reprinted from Journal of Sound and Vibration, Vol 60, H. M. Nelson, High frequency flexural vibration of thick rectangular bars and plates, pp 101–118, Copyright (1978), with permission from Elsevier

of concrete material properties and the defect lateral defect dimensions is required. The dimensionless frequency parameters that originate from published closed-form solutions of vibrating plates are also required. While extensive sounding using a grid can estimate lateral dimension information, other non-destructive methods as such infrared thermography offer a more expedient alternative.

4.2 Specimens

Seven reinforced concrete test slabs were constructed with simulated defects to evaluate the performance of several acoustic sounding methods. Six of the slabs, numbered 1 through 6, contained simulated voids and delaminations that were introduced during casting. The remaining slab served as a control slab that was free of induced defects or imperfections, numbered slab 7. All slabs are the same nominal size: $36 \times 36 \times 5.5$ inches (approximately $914 \times 914 \times 140$ mm). This ensures the lateral dimensions of the plate are more than six times the thickness, in accordance with the ASTM Standard C1383 – 15 [3] definition of a plate.

Each slab contains a grid of steel rebar reinforcement— three equally-spaced 800 mm lateral pieces of 10 mm diameter rebar ½ inch (12.7 mm) from the bottom surface of the slab, and three equally-spaced 800 mm longitudinal pieces of rebar fastened directly on top of and perpendicular to the lateral pieces using bailing wire. This reinforcement simulates that typically observed in slab-on-grade reinforced concrete slabs. Small plastic rebar chairs support the bottom layer of rebar to maintain the ½ inch (12.7 mm) cover.

The concrete mix was supplied by Butler Brothers Supplies Ltd. of Saanichton BC. Nominal properties of the concrete mix are 32 MPa target strength, 75±20 mm slump, 6±1% air, with 20 mm maximum aggregate size. A slump test performed during casting yielded a measurement within the specified range. The concrete was left in the forms during the curing process with the upper surface exposed to ambient weather conditions. No moist curing was used at any time during the curing process. The ambient temperature during the first 28 days of curing ranged between roughly 9 and 29.7 °C. Several 100 mm diameter 200 mm height test cylinders were cast at the same time as the slabs and left next to the slabs to expose the cylinders to curing conditions similar those experienced by the slabs. These cylinders were used to estimate the density and compressive strength of the concrete slab specimens. Tests were performed on the cylinders 80 days after casting

to allow full curing of the cylinders under ambient conditions. The concrete density of the cylinders was roughly 2300 kg/m^3 and the mean of three tested specimens resulted in a compressive strength of 23.6 MPa.

The essential dimensions of the control slab are shown in Figure 4.3a, including reinforcement (reinforcement is the same for all slabs). An example of the nominal configuration of a slab with defects is shown in Figure 4.3b, which illustrates the key parameters of slab 3, including the simulated voids. Other simulated defect slabs have a similar configuration with different nominal defect locations. The as-built simulated defect locations show some variance from the nominal configurations.

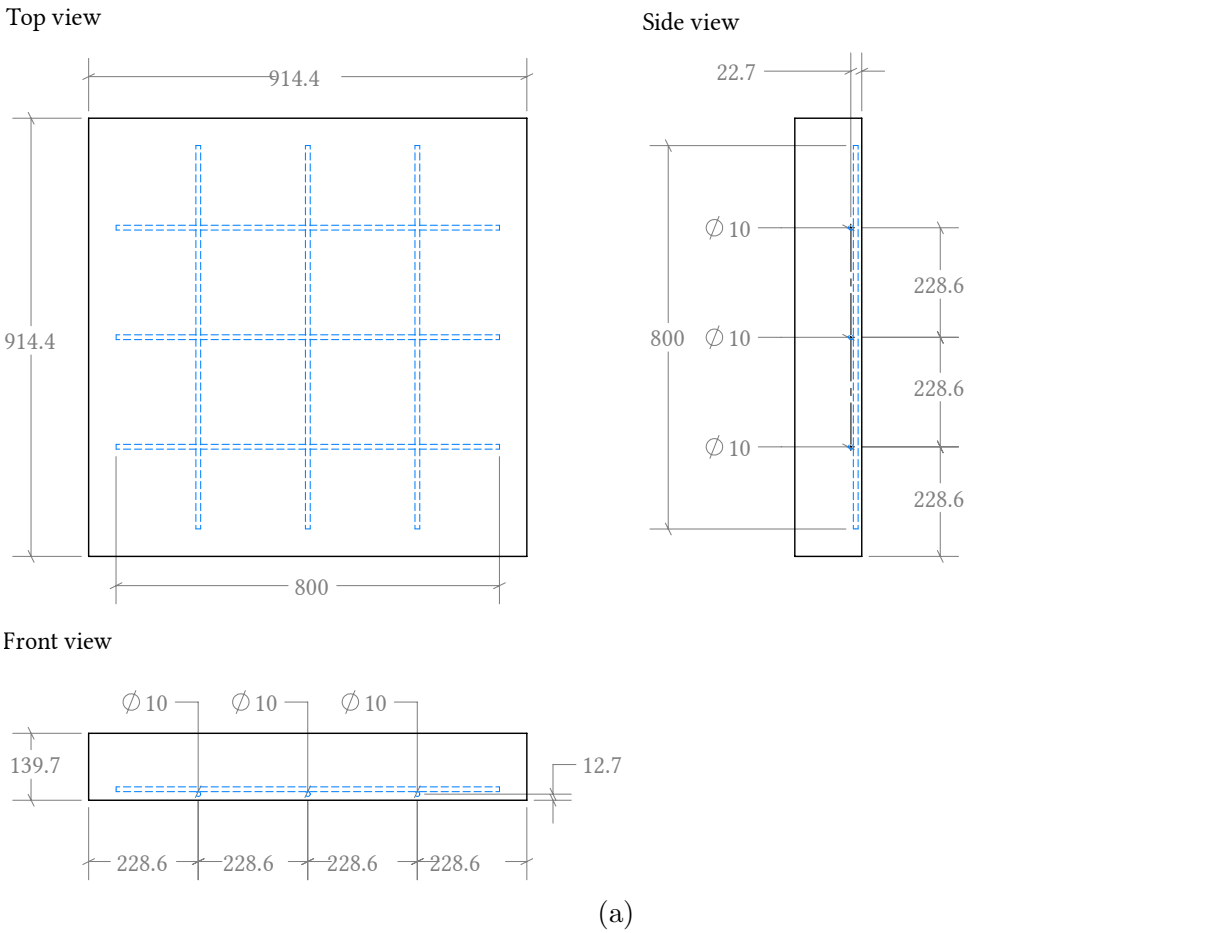

Figure 4.3: All dimensions are in mm: (a) Dimensions of the control slab; (b) Dimensions of slab 3 including nominal void locations (red) and rebar (blue).

Artificial voids and delaminations were deliberately introduced in slabs 1 through 6. Each slab contains a different arrangement of circular foam discs replicating voids or square plastic sheets simulating delaminations. Foam discs and plastic sheets have previously been used by Lu [49] as well as Zhu and Popovics [15] to simulate voids and delaminations, respectively. The void-simulating discs are cut from 1.5 in (38.1 mm) thick polystyrene insulation foam. The simulated delamination plastic squares are constructed of three layers of HDPE plastic laminated at the edges using an adhesive cloth tape, and are roughly 9 mm thick overall. Foam discs and plastic sheets are shown in Figure 4.4a and 4.4b.

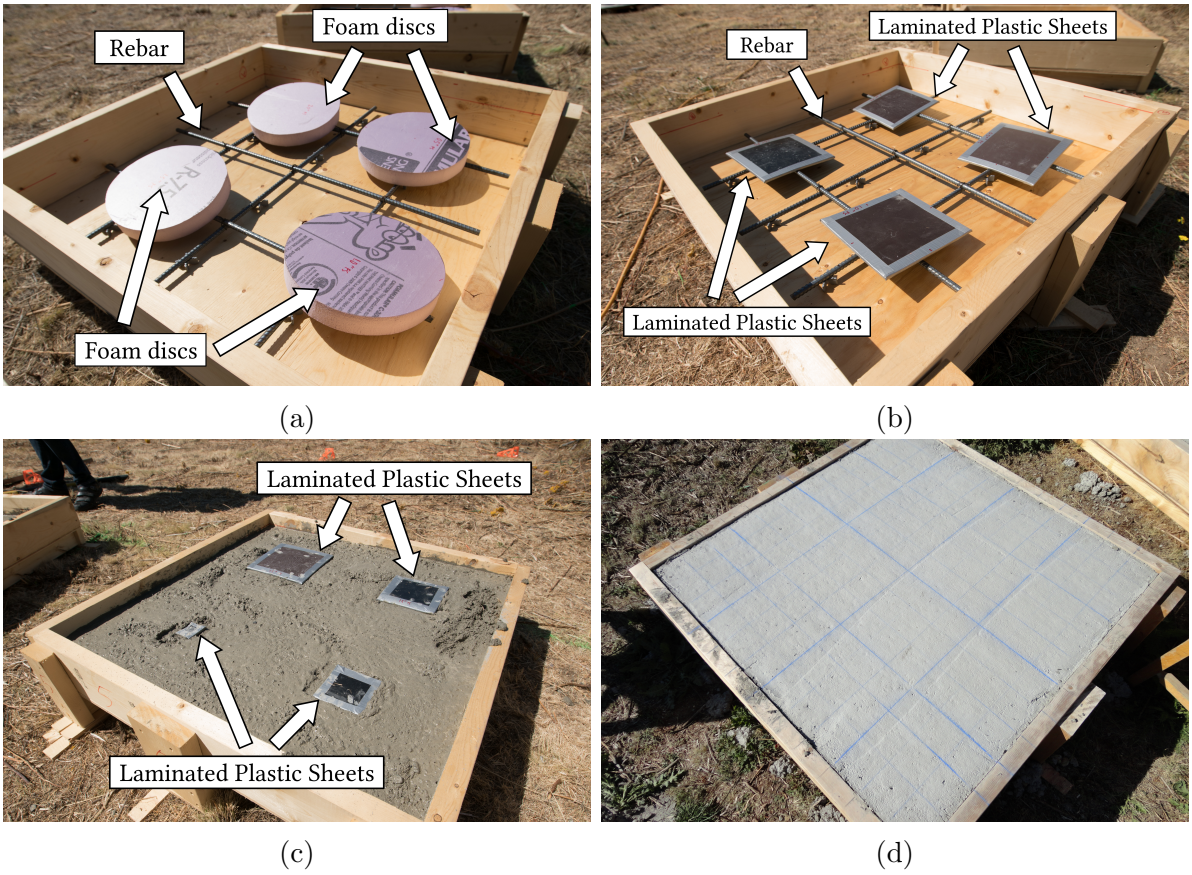

Figure 4.4: (a) Formwork showing the foam discs used to simulate voids; (b) Formwork with laminated plastic sheets used to simulate delaminations; (c) In-situ placement of laminated plastic sheets during casting; (d) Slab shown in formwork with 3 × 3 in surface grid shown.

The lateral defect dimensions (width and length for delaminations and diameter for voids) as well as the nominal depth of the simulated defects (distance from the upper concrete surface to the top surface of the foam or plastic) are different for each slab. Simulated defects were placed with the surface of the plastic or foam parallel to the top

and bottom of the slab. The center of each simulated defect surface was placed roughly 9 in (229 mm) from the two nearest edges of the slab. The plastic and foam were hand placed in the slab during casting without the aid of any anchoring system, as shown in Figure 4.4c. As a result, some significant variation in the nominal and actual simulated defect location was observed. The as-built lateral location of the simulated defects was confirmed for reference using infrared thermography. Actual as-built depths were measured after acoustic testing by drilling the slabs and measuring the depth to the nearest millimeter using ruled calipers. For defects that were left slightly out-of-plane (defects that did not have perfectly uniform depth), multiple measurements were taken and the mean was computed, as necessary. A summary of all as-built simulated defect dimensions and depths is included in Table 4.1. Expected frequencies calculated based on as-built locations using Equations 4.1, 4.2, and 4.3 are presented in Table 4.1 along with those measured via hammer-based accelerometer testing for defects that are detected.

Table 4.1: As-built and target dimensions and depths of defects of voids and delaminations (Del). Expected and measured frequencies are also presented.

No.	Type	Lateral Size (mm)	Target Depth (mm)	As-built Depth (mm)	Expected Freq. (kHz)	Accelerometer-measured Freq. (kHz)
1	Del	203×203	13	39	3.5	2.5
2	Del	203×203	25	49	4.3	3.2
3	Del	203×203	38	73	—	—
4	Del	203×203	51	82	—	—
5	Del	203×203	64	84	—	—
6	Del	203×203	76	101	—	—
7	Del	203×203	89	98	—	—
8	Void	⌀ 254	13	15	1.2	1.2
9	Void	⌀ 254	25	27	2.0	2.1
10	Void	⌀ 254	38	43	2.8	2.9
11	Void	⌀ 254	51	53	3.3	3.0
12	Void	⌀ 254	64	60	3.5	3.2
13	Void	⌀ 254	76	73	—	—
14	Void	⌀ 254	89	90	—	—
15	Del	203×203	38	62	4.7	4.0
16	Del	152×152	38	48	6.4	4.9
17	Del	102×102	38	84	—	—
18	Del	51×51	38	92	—	—
19	Void	⌀ 254	38	27	2.0	1.9
20	Void	⌀ 203	38	28	3.0	2.7
21	Void	⌀ 152	38	28	5.0	4.6
22	Void	⌀ 102	38	42	—	—

For the purposes of Table 4.1, defects are numbered starting in the upper left hand corner of each slab in a clockwise fashion, starting from the number one above the highest of the previous slab, as shown in Figure 4.5.

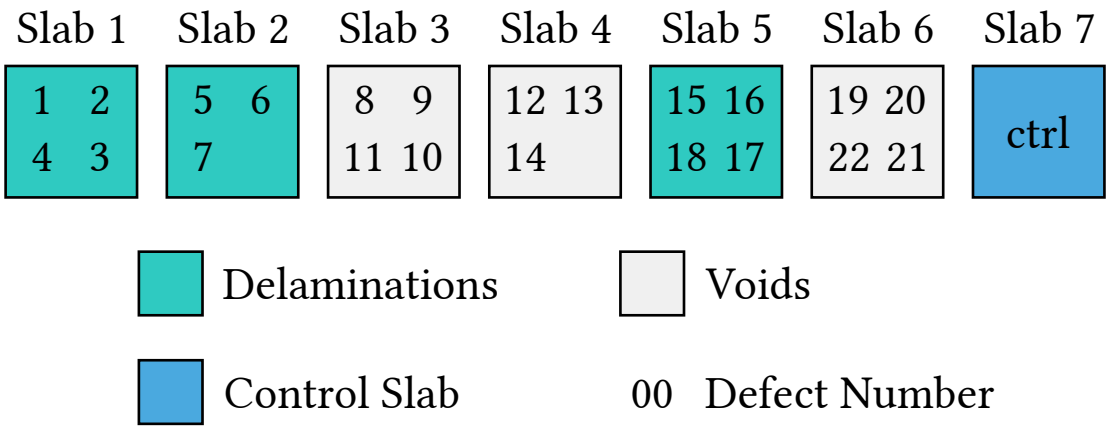

Figure 4.5: Defect numbering schemes for Table 1.

The top surfaces of the slabs are coarsely finished, resulting in exact as-built slab thickness to vary from the nominal 140 mm by roughly plus or minus 7 mm. All slabs and formwork are approximately level. A 3 × 3 in (76 mm) rectilinear grid, as shown in Figure 4.4d was established on the slab surfaces during testing to ensure consistent excitation location. The slabs were removed from formwork for acoustic testing, with two opposite edges resting on dimension lumber that was on a soft dirt foundation. There was no more than 3.5 in (89 mm) overlap between the wooden support and the bottom of a slab at the edge.

4.3 Methods

4.3.1 Audio recording and processing

Audio recording was performed using a Zoom H1 digital voice recorder. The Zoom H1 can record at a sample rate of 96 kHz at 24 bit depth, which means a frequency response as high as 48 kHz can be observed in a recording. The Zoom H1 does analog-digital and digital-analog conversion at 24-bit depth, and signal processing at 32-bit to ensure no information is lost in the recording process.

The microphone used during all recording was a Polsen OLM-20 Dual Omnidirectional Lavalier Microphone. This microphone records two mono signals from two microphones, so only the left signal was used in this work. It has a specified flat frequency response from 30 Hz to 18 kHz, which is an acceptable range for the type of defects and analysis used in

this study. The recorder and microphones are shown in Figure 4.6.

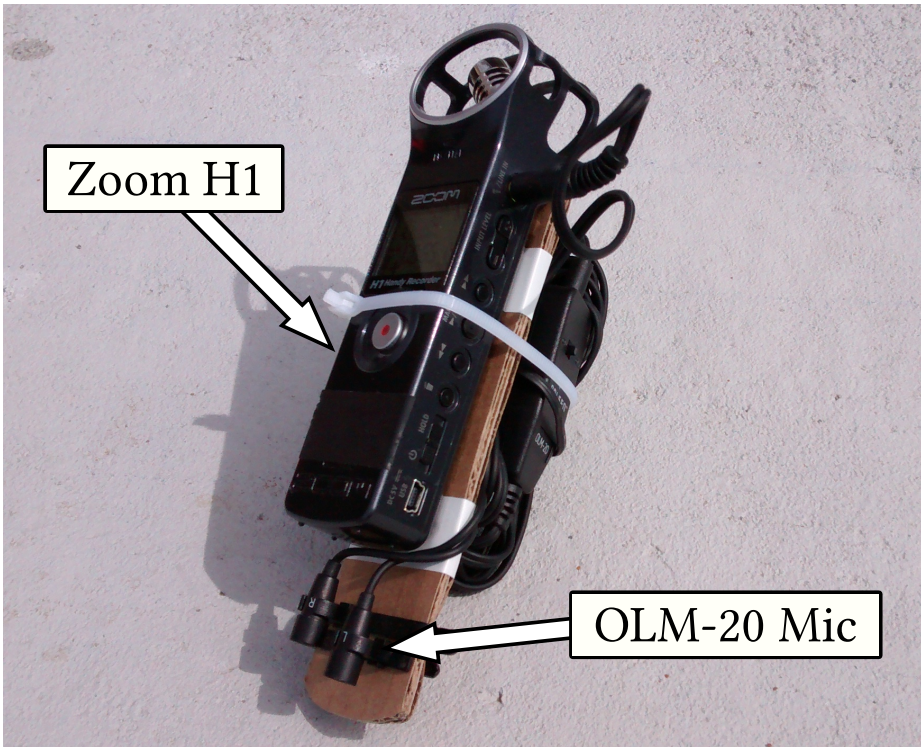

Figure 4.6: Microphone configuration showing two microphones and Zoom H1 recorder.

The Zoom H1 records the audio files in WAV format. Audacity® audio software was used to isolate the audio associated with a particular trial, which are then saved to shorter WAV files. Each of these short WAV files contains audio related only to a particular trial. Each file corresponds to a particular test case at a specific location over a simulated defect on a given slab. For example, one such file contains the audio of the hammer percussion test performed over the location of the shallowest defect of slab 3, and another file contains the same information but for the second shallowest defect. MATLAB® was used to extract frequency information out of the short WAV files. A single-sided fast Fourier transform (FFT) was generated for each trial, and the frequencies of the peaks of the amplitude spectrum are identified and recorded.

4.3.2 Hammer percussion sounding

Exact requirements for a hammer percussion sounding test are not well established by current sounding procedures such as those in ASTM standard D4580/D4580M – 12 [2].

However, the operating concept behind a hammer percussion test is similar to those tests and is relatively straightforward; a hammer is used by the operator to strike the concrete specimen, and the resulting acoustic disturbance is used to garner information about the concrete specimen. Instead of listening to the response by ear, the audio signals were digitally recorded and processed as described in the preceding section to extract meaningful frequency information. The hammer strike locations on the slabs are nodes in the 3×3 inch surface grid roughly over the center of each simulated defect (9 in from each of the two closest edges).



Figure 4.7: (Left to right) The 1, 2, 4, and 8 oz. hammers and Zoom H1 with OLM-20 mic. An 18 in (45 cm) ruler is shown for scale.

The four hammers were used in this study are shown in Figure 4.7. Three ball-peen hammers with weights 1, 2, and 4 oz. (0.028, 0.057, 0.113 kg, respectively) were used along with an an 8 oz. (0.227 kg) flat-head hammer. The diameters of the roughly hemispherical ball-peen hammers are 8.9 mm, 11.2 mm, and 17.4 mm for the 1, 2, and 4 oz. hammers respectively. According to the methods of Sansalone and Streett [50], steel ball impactors with diameters 8.9, 11.2, and 17.4 mm should have maximum excitation frequencies of 32.7, 26.0, and 19.8 kHz respectively. However, a hammer head has a noticeably higher mass in comparison with a steel ball of the same diameter as the hammer head. The mass to contact stiffness ratio determines the contact time for an impactor. Accordingly, the steel ball-peen hammers have higher contact times and lower maximum excitation frequencies than steel balls of the same diameter. The microphone was hand-held at a lateral distance of 56 mm or less from the impact location: less than 40 % of the slab thickness as in an

air-coupled impact echo test [15]. The configuration of the hammer impact test is shown in Figure 4.8.



Figure 4.8: Hammer percussion test configuration.

4.3.3 Speaker-based excitation sounding

A novel sounding procedure used a speaker (electroacoustic transducer) and the same operating concept as the hammer percussion method: a concrete specimen is vibrated and the audio response is recorded and processed. Gudmarsson, Ryden, and Birgisson [51] have shown a speaker is capable of non-contact resonance frequency excitation in asphalt concrete, but used an accelerometer on the surface for measurements. To adapt a speaker for use with sounding, the speaker excitation was made via contact, and the recording was performed using the same microphone procedure as the hammer percussion test. A speaker was temporarily affixed via an adhesive pad to the concrete specimen surface directly above the center of a defect location and variety of signals were played by the speaker to excite the concrete specimen.

There were a total of sixteen signals tested, including half-sinusoid "bump" features and symmetric up-down ramp functions in the image of a "spike" of durations 0.5, 0.2, and 0.1 milliseconds. The remaining ten signals were logarithmic chirps of varying length. Up-chirps started at an instantaneous frequency of 100 Hz and ended at 8 kHz, while

down-chirps progressed oppositely from 8 kHz to 100 Hz. Chirp lengths of 8, 20, 200, 1000, and 2000 ms were used.

The setup for the speaker-based excitation test is shown in Figure 4.9. The locations of the speaker on the surface of the concrete specimen are the same as those struck by the hammer during percussion sounding. A Boombx V1 vibration speaker with a frequency response range from about 0.3 to 10 kHz was used for all speaker excitation. The speaker unit is detachable and connects to the power box of the system using a 3.5 mm audio cable. The excitation signals were played from a computer using Audacity® and a Syba AUD201 USB soundcard.

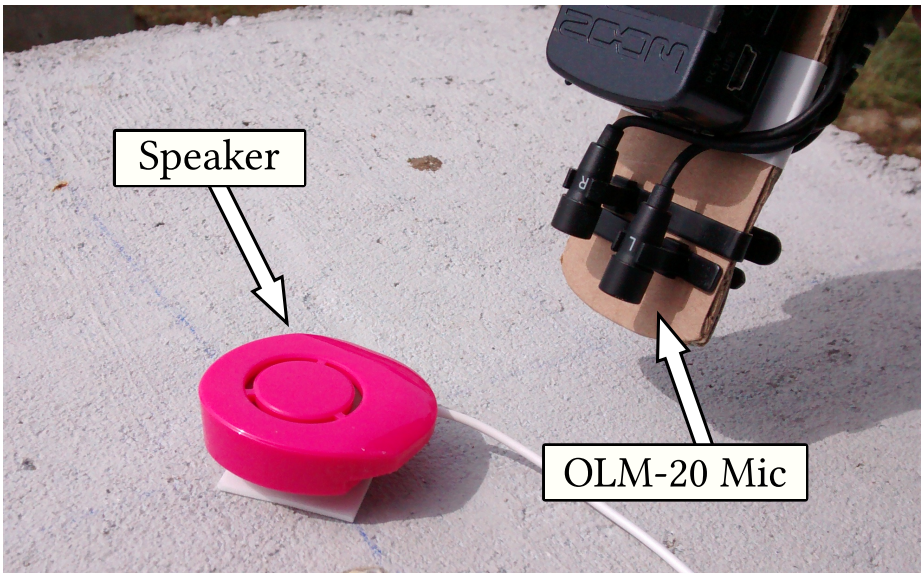

Figure 4.9: Close-up view of speaker unit attachment to slab surface.

4.3.4 Modified chain drag

The chain drag is a well-established test procedure for detecting delaminations in concrete bridge decks as in ASTM standard D4580/D4580M – 12 [2]. In practice, a chain drag is performed by an operator who drags a chain over a concrete deck or floor and listens for problem areas, which are marked with paint when detected. For this study, a three-link chain was dragged over the slab surfaces above where defects are located. The chain used was a hot dipped galvanized proof coil chain with link diameter 3/8 inch (9.5 mm) and total link length 2 1/8 in (54 mm). However, it has been reported that multiple chain links used during the standard test can sometimes produce unwanted noise and false positives in part

due to the added noise of chain links bumping into each other [17]. With self-noise due to chain links colliding with each other in mind, a single-link chain drag was also performed, in addition to the three link drag. A contraption was designed and constructed in which the chain is attached via a wire and foam connector to a 39 inch (991 mm) aluminum tube. The foam prevents unwanted noise from collisions between the aluminum tube and the chain link. The Zoom H1 recorder and microphones are mounted to the aluminum pole to give better acoustic access to the source of the sound signal, as shown in Figure 4.10.

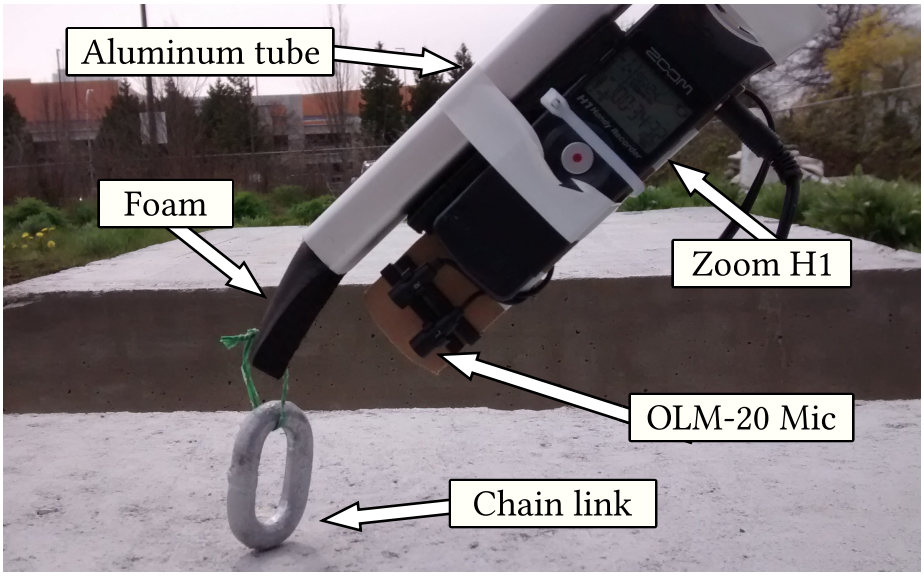

Figure 4.10: The single-link chain drag test configuration during a pass over a test slab.

4.3.5 Accelerometer and glass disc reference measurements

To validate the hammer data against a reliable reference measurement, accelerometer data was also recorded for hammer tests. As shown in Figure 4.11 An acclerometer was placed at 2 in (51 mm) or less lateral distance from the impact location for all tests and the response was recorded to offer reliable baseline data for hammer performance. An Olson Instruments RTG-1 Resonance Test Gauge (which uses a PCB Piezotronics 353B15 accelerometer) was used as the system for all accelerometer tests. The chain and speaker methods used did not produce impacts of the magnitude required by the RTG-1 system, so accelerometer data was recorded only for the hammer tests.

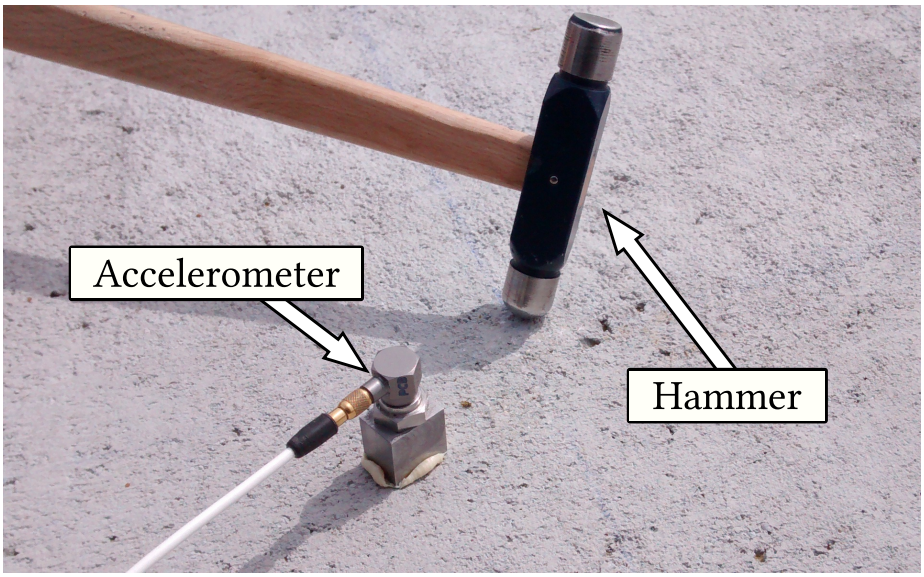

Figure 4.11: Accelerometer configuration for hammer impact test on concrete.

The V1 speaker performance was evaluated using a glass disc. The speaker was placed in the center of a glass disc and the response to the same battery of signals used with the concrete was recorded. The glass disc (with diameter 500 mm and thickness 5.8 mm) was placed on acoustic foam with a circle cutout so that only the outer 1 in (25 mm) of the disc rested on the foam. With this method of support, the plate can be considered to have roughly free boundary conditions. By testing the speaker on another medium with more well-known dimensions and boundary conditions like the glass disc, the features of the acoustic response caused by the speaker itself can be distinguished from those caused by the concrete vibration. A hammer test with both microphone recording and a contact accelerometer was also performed on the glass to verify the frequency peaks observed in the speaker test.

4.4 Defect detection performance

The basis for the detection of a defect is a comparison between the frequency spectrum of a test on a slab location to the frequency spectrum recorded at a similar place on the control slab. While the most prominent peak in the frequency spectrum is an important consideration in this comparison, the size and location of other peaks is also of interest. For example, in the hammer test results, defects that are not detected may have different prominences in peaks compared to the control slab. However, they typically demonstrated

low frequency peaks in the vicinity of 400 Hz and 700 Hz, as well as a higher frequency peak between 12 and 15 kHz. The lower peaks are to be expected from the flexural vibration of the entire slab, and the higher peaks are possibly caused by compressive vibration of the slab (of the type exploited by impact echo methods). The exact forms of the response signals for defects and the control slab depended on excitation methods (hammer, speaker, or chain) and parameters (impactor size, mass, or excitation signal).

A comparison of the frequency spectrum for defects that are detected and another that is not, along with the frequency spectrum of the control slab is shown in Figure 4.12 for the 2 oz. hammer test, as recorded using the Zoom H1. The spectrums have been normalized by their maximum value for the purposes of Figure 4.12 as the varying absolute amplitudes of the different spectrums make the comparison visually difficult otherwise. Similarly, the frequency in Figure 4.12 has been limited from 0 to 7 kHz to frame the peaks of interest appropriately.

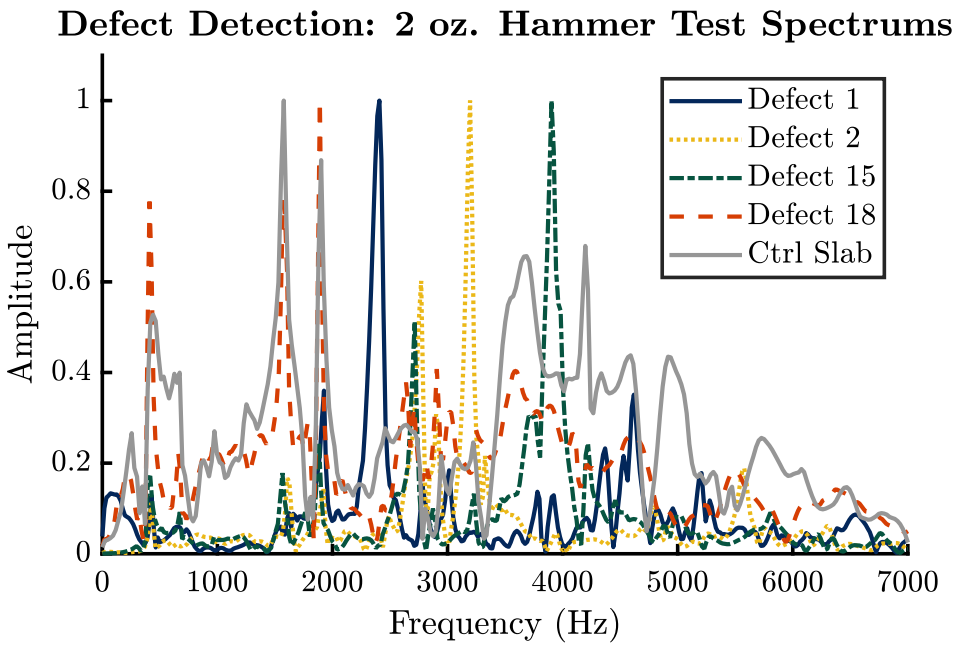

Figure 4.12: Frequency spectrums for 2 oz. hammer test showing detected and undetected defects spectrums along with the control slab spectrum.

The frequency spectrums for Defects 1, 2, and 15 in Figure 4.12 have a most prominent peak that indicates a dominant flexural mode of vibration, and stand in stark contrast to the shape and form of the control slab frequency spectrum. Less prominent peaks in these spectrums may correspond to other modes of vibration or overtones. Importantly, the most prominent peaks in these three microphone-recorded spectrums have a mean percent

difference of 5 % from those measured using the contact accelerometer. Deeper defects and those with smaller lateral size have higher frequency peaks than shallower defects with larger lateral size. Spectrums from the other hammers show the same trends as those in the 2 oz. hammer test.

Conversely, the frequency spectrum for Defect 18 shown in Figure 4.12 has significant similarity to the control slab spectrum. There are peaks near 400 Hz, 1.6 kHz, and 1.9 kHz, and there is no other dominant peak to indicate the kind of flexural vibration associated with a subsurface defect. A comparison between the frequency spectrum for Defect 18 and the control slab is not adequate to say that a defect has been detected.

A summary of the defect detection via each of the three primary method tested is shown in Table 4.2. For the hammer and speaker tests, if one variation detected the defect, the result in Table 4.2 is a positive detection. For example, if only two of the six chirps tested detect a defect, the result in Table 4.2 is considered a positive detection for that defect for the speaker chirp method. Out of 22 total defects, the hammer methods detected 12 defects, the speaker methods detected 9 defects, and the chain drag methods detected 10 defects.

Table 4.2: Defects detected by the sounding methods used in this study.

Detected: yes (Y) or no (—)						
	Hammer		**Speaker**		**Chain Drag**	
Defect No.	Acoustic	Accel.	Bumps /Spikes	Chirps	Single-link	Triple-link
1	Y	Y	Y	Y	Y	Y
2	Y	Y	Y	—	—	Y
3	—	—	—	—	—	—
4	—	—	—	—	—	—
5	—	—	—	—	—	—
6	—	—	—	—	—	—
7	—	—	—	—	—	—
8	Y	Y	Y	Y	Y	Y
9	Y	Y	Y	Y	Y	Y
10	Y	Y	—	Y	Y	Y
11	Y	Y	—	—	Y	Y
12	Y	Y	—	—	—	Y
13	—	—	—	—	—	—
14	—	—	—	—	—	—
15	Y	Y	—	Y	—	—
16	Y	Y	—	Y	—	—
17	—	—	—	—	—	—
18	—	—	—	—	—	—
19	Y	Y	Y	Y	Y	Y
20	Y	Y	Y	Y	Y	Y
21	Y	Y	—	—	Y	Y
22	—	—	—	—	—	—

4.4.1 Slab vibration and thickness ratio

Table 4.3 summarizes defect detection based on detection method and plate thickness using the ratio of depth to side length for delaminations) and the ratio of depth to diameter for voids (h/b and $h/2a$ respectively).

As Table 4.3 shows, there appears to be a relationship between the detectability of a defect via the sounding methods used and the thickness of the plate of concrete left above the defect. Values in Table 4.3 are sorted according to h/b or $h/2a$ as this measure is dimensionless. Although more data is required to accurately estimate the depth to side

Table 4.3: Defect detection for each method sorted by defect depth to lateral size ratio.

Defect		**Detected: yes (Y) or no (—)**			
No.	Type	h/b or $h/2a$	Hammer	Speaker	Chain
8	Void	0.06	Y	Y	Y
19	Delam	0.11	Y	Y	Y
9	Void	0.11	Y	Y	Y
20	Void	0.14	Y	Y	Y
10	Void	0.17	Y	Y	Y
21	Void	0.18	Y	—	Y
1	Delam	0.19	Y	Y	Y
11	Void	0.21	Y	—	Y
12	Void	0.24	Y	—	Y
2	Delam	0.24	Y	Y	Y
13	Void	0.29	—	—	—
15	Delam	0.31	Y	Y	—
16	Delam	0.32	Y	Y	—
14	Void	0.35	—	—	—
3	Delam	0.36	—	—	—
4	Delam	0.40	—	—	—
22	Void	0.41	—	—	—
5	Delam	0.41	—	—	—
7	Delam	0.48	—	—	—
6	Delam	0.50	—	—	—
17	Delam	0.82	—	—	—
18	Delam	1.80	—	—	—

ratio cut-off point, the values in Table 4.3 seem to indicate that an h/b or $h/2a$ of about 0.35 or less seems to yield an acceptable level of detection.

If a defect is both deep and lacks sufficient lateral size, the vibration of the concrete above is no longer adequately plate-like and the vibration of the slab as a whole appears to dominate the audio recording of the test. So, for a square defect such as a delamination with side length 8 in (203 mm), detection would be expected up to depths of about 2 in (51 mm). It is possible that the boundary conditions on an actual structure such as a bridge deck play a role in what ratio of depth to lateral size is acceptable.

4.4.2 Speaker performance: glass

The speaker tests on the glass plate offer insight into the speaker results for the concrete slabs. The plate is excited by the speaker in the center, which should excite modes of vibration with zero nodal diameters. The first four modes of vibration with zero nodal diameters can be computed using Equation 4.3. Required are the dimensions of the glass plate (a = 0.025 m, h = 0.0058 m), nominal glass material properties ($\nu = 0.24$, $E = 69$ GPa, $\rho = 2500$ kg/m^3), and the appropriate frequency parameters for a free circular plate from Leissa [52]. Computing the frequencies using these values yields $f_{01} = 205$ Hz, $f_{02} = 885$ Hz, $f_{03} = 2.02$ kHz, and $f_{04} = 3.62$ kHz where the first subscript indicates the number of nodal diameters and the second indicates the number of circular nodes in the vibration.

The first four prominent frequency peaks in the spectrum from the speaker test of the glass disc occur at 207 Hz, 879 Hz, 2.01 kHz, and 2.7 kHz. The first three are in near perfect agreement with the predicted peaks, although the fourth is not. A closer inspection reveals that a peak at roughly 3.6 kHz does exist, but the peak at about 2.7 kHz is more prominent. This is a likely indication that the speaker itself may be responsible for some peaks in close proximity to 2.7 kHz.

Comparison of the speaker data to the accelerometer and speaker data collected during a hammer test of the glass plate also supports the notion of speaker noise causing peaks. For the accelerometer hammer measurement the fourth peak is located at 3.74 kHz and for the hammer acoustic measurement the peak is located at 3.54 kHz; both are near the expected location of 3.62 kHz.

Up-chirp speaker signals appear to generate some kind of noise peaks in neighborhood 5.6 and 8.0 kHz. These peaks become more pronounced as the length of the up-chirp increases. Figure 4.13 shows frequency spectrums for down chirps for the glass disc showing the peaks associated with first four modes of vibration with zero nodal diameters.

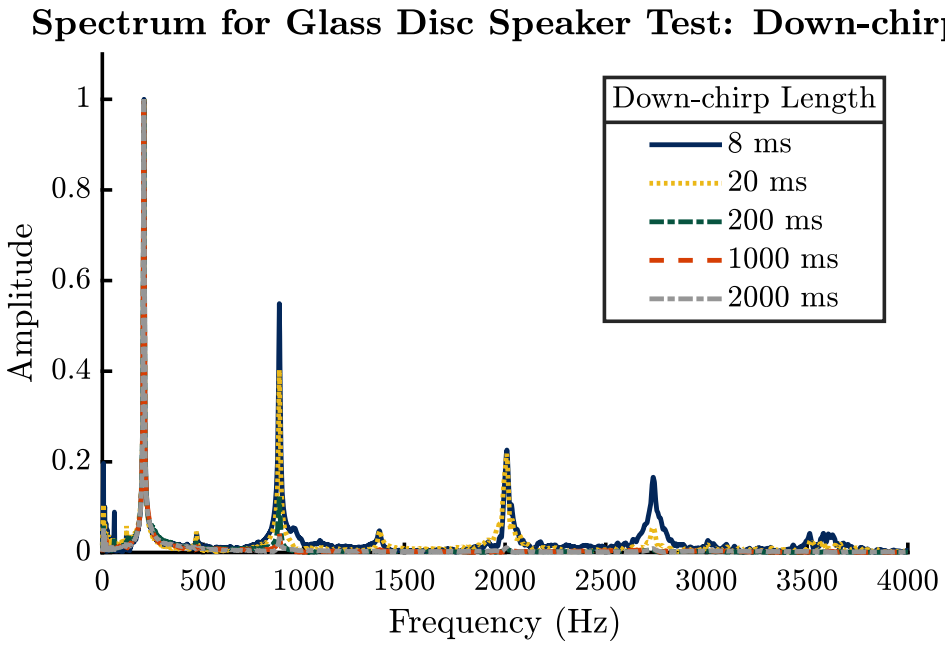

Figure 4.13: Normalized down-chirp spectrums for the glass speaker test showing peaks associated with modes of vibration with no nodal diameters.

Amplitudes in Figures 4.13 and 4.14 are normalized by the largest value in each spectrum to make the plots easier to view (the amplitude is also plotted on a logarithmic scale in Figure 4.14 for this purpose). Figure 4.14 shows a comparison of the 1000 ms up- and down-chirp signals for the glass disc. From Figure 4.14, it can be observed that the noise in the vicinity of 5.6 kHz can be found in both the up-chirp and down-chirp signals. The noise in the neighborhood of 8.0 kHz appears to be exclusive to the up-chirp signal.

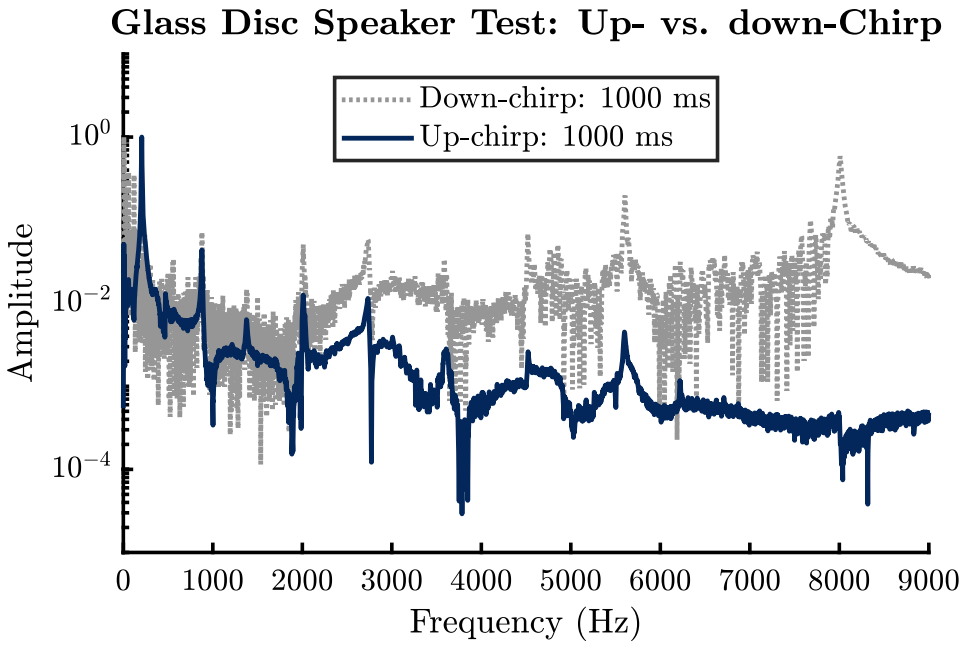

Figure 4.14: Comparison of normalized 1000 ms up- and down-chirp spectrums for the glass disc speaker test.

4.4.3 Speaker performance: concrete

The speaker performance for concrete is somewhat similar to that of the glass plate tests. In general, both impact-like speaker signals (half-sinusoid "bumps" or up-down ramp "spikes") and down-chirps generate peaks that appear to correspond to flexural vibration above defects, while the up-chirps produce more noise. While the glass disc testing indicates that these peaks are caused by the speaker itself, it is possible that this is a problem isolated to the specific speaker used in this work.

For impact signals, longer signals produced less noise but were limited in detection of defects that exhibited higher resonant frequencies. For example, normalized frequency spectrums for the signals tested above defect #8 are shown in Figure 4.15. To avoid interference from the frequency content of the excitation signal itself, all audio for the speaker is carefully selected to use only the part of the overall signal that corresponds to the response that follows the excitation signal.

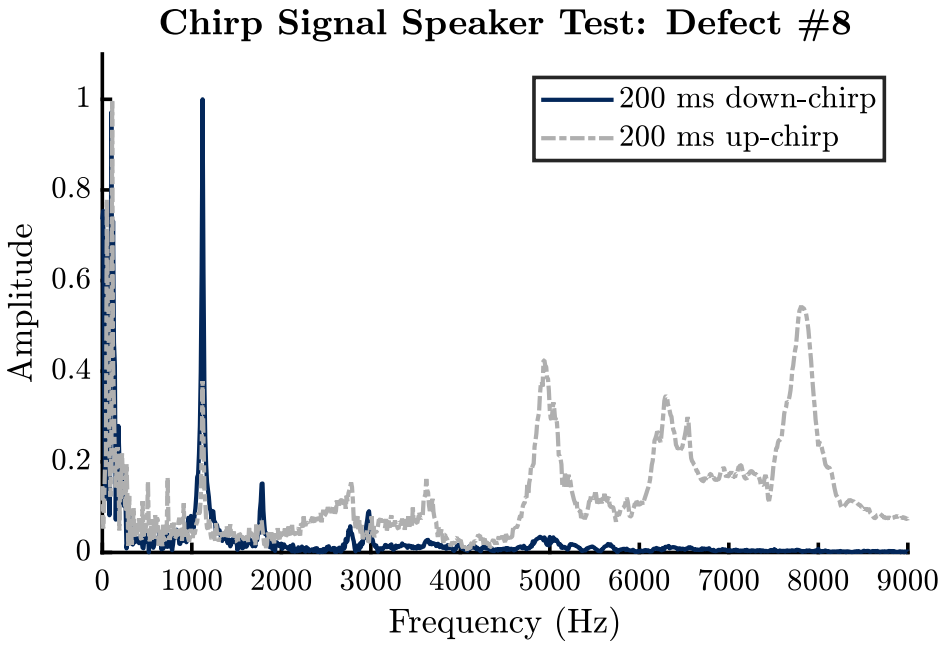

(a)

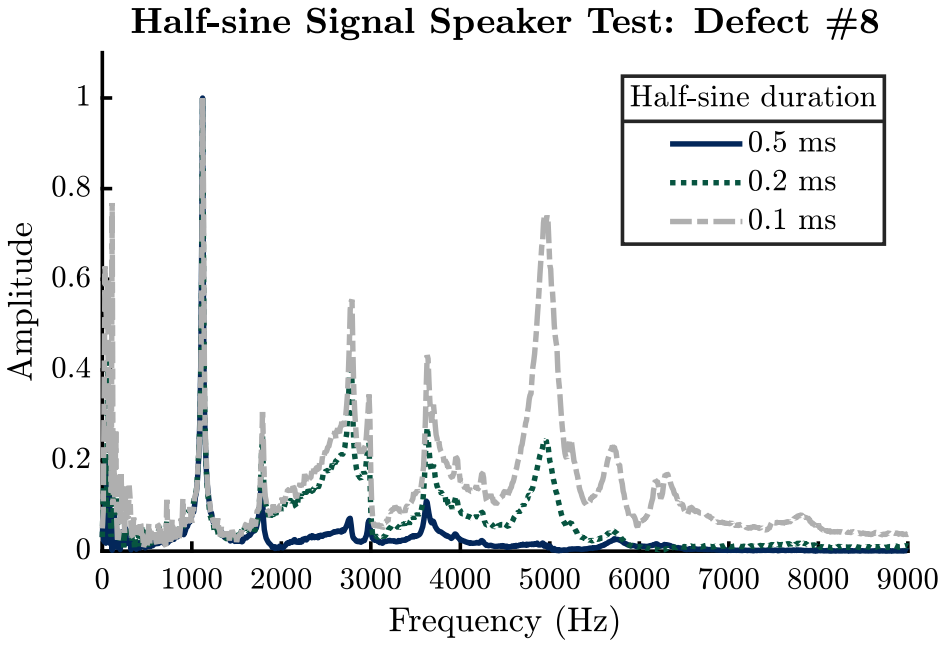

(b)

Figure 4.15: Frequency x-axis ranges are set to best display features of interest. (a) Comparison of normalized 200 ms up- and down-chirp spectrums for the concrete speaker test of defect #8. (b) Comparison of normalized spectrums for half-sine "bump" signals of different lengths for speaker test of defect #8.

As shown in Figure 4.15, there is a clear resonance peak that indicates defect detection at roughly 1120 Hz and other peaks that may be caused by noise, other modes of vibration,

or overtones. Up-chirps of longer duration like the 200 ms signal spectrums shown have significant noise in the 5–6 and 8 kHz range as was observed in the glass disc test. The noise in the 5–6 kHz range also appears in the spectrums for the shorter duration half-sine signals. The speaker used is very inexpensive and has a thin injection molded plastic casing. It is possible that this particular signal and duration produce some vibration of this speaker casing that causes the noise observed, but more investigation is required to determine the exact cause of these noise peaks with certainty. The low frequency noise (below about 300 Hz) appears to be at least somewhat related to the ambient conditions (primarily wind and nearby traffic and construction). The low frequency of this noise is not in a range that would be associated with concrete specimens and type of vibration explored in this study.

For chirps, as excitation signal length is increased, the impact of noise becomes more significant. The frequency spectrums for up-chirps indicate significantly more noise in the signal that those for down-chirps. Though no bias caused by transient vibrations is discernible, it may be difficult to detect due to frequency components from noise (likely attributable to ambient noise or speaker self-noise), which is evident to some degree in nearly all frequency spectrums for chirp-based tests. The frequency peaks in the spectrums for chirp based tests are consistent between chirp signals of different lengths, and betwen up- and down-chirps, but the relative magnitudes of the peaks fluctuate. For those defects detected by the chirp-based speaker test, the shorter signal lengths produce resonance peaks that have greater prominence compared to peaks attributed to noise or peaks that also appear in the control slab (that is, frequency peaks associated with non-defect vibration). To determine an optimal shape of the acoustic signal which produces minimal levels of noise and avoids transient vibration bias, testing with a larger variety of signal lengths is suggested. Of the chirp signals used in this work, the 8 ms down-chirp produced the least noise and most prominent resonance peaks.

4.4.4 Performance of hammer percussion and chain drag

The hammers used all demonstrated adequate sounding performance. The frequency spectrums of the hammers are generally very similar, but some variation between hammers is observable. The acoustic hammer tests were verified using a contact accelerometer. In general, the results of the accelerometer and acoustic tests are in very good agreement for the defects that are detected. The percent error between the accelerometer and hammer

measurements in this case is usually less than 5 % and always less than 12 %.

In general, for spectrums in which subsurface defects are detected there is very little difference between the frequency of peaks for different hammers (5 % difference or less). The peak that is most prominent may differ between hammers, but the frequencies of the peaks are generally very consistent between hammers provided a defect is detected.

In order for the chain drag to produce meaningful results, the frequency peaks caused by noise from the chain links themselves needs to be removed from consideration. The chain links produce minor noise across a wide frequency range, but the most prominent noise occurs between 13 and 14.5 kHz. This noise occurs in both single-link and triple-link tests, indicating it is possibly cause by a vibration in the link itself. The prominence of the noise peaks in this range can be so large that it becomes difficult to properly detect peaks associated with defective concrete vibration in the frequency range of those expected in this study (about 1 to 12 kHz). Thus, the chain link frequency range for peak detection was deliberately limited to between 200 Hz and 13 kHz to avoid some self-noise from the chain. Since the exact frequency of the chain self-noise is likely dependent upon the chain properties, it may be advisable to verify chain noise parameters before conducting concrete sounding via a chain drag method with a particular chain.

4.5 Conclusions

This work evaluates the performance of three sounding methods in detecting simulated subsurface concrete defects in a series of test slabs. Hammer percussion, a speaker excitation method, and chain drags, were adapted as concrete sounding techniques for use with a microphone and recorder coupled with an audio file analysis procedure. The hammer percussion, speaker, and chain drag methods all detect a similar number of defects. In general, the ratio of depth of the concrete above a simulated defect to the lateral dimensions of the defect may be said to limit the detectability of the defect using the sounding methods. The speaker test was found to be sensitive to the length and type of the excitation signal. Speaker excitation signals with shorter durations produced more distinct results than longer signals in some cases, but more investigation is required to determine the exact effect of signal duration and type on frequency excitation and subsequent defect detection. Three chain links in series detected a larger number of defects compared to a single chain link. Self-noise from the chain was observed but did not overlap with meaningful flexural

frequency content associated with concrete defects for the slabs tested. More work is required to assess the relationship, if any, between the accuracy of depth estimation using frequency of flexural vibration and defect depth to lateral size ratio.

Acknowledgements

The authors would like to acknowledge the assistance of the fine technical support staff with the UVic Facility for Innovative Materials and Infrastructure Monitoring in constructing the test specimens. This work has been completed with financial support from India-Canada-IMPACTS and Networks of Centres of Excellence of Canada. In-kind support from Butler Brothers Supplies Ltd. is also acknowledged.

Chapter 5

UAV-based sounding of subsurface concrete defects

This chapter is a pre-publication version of a paper concerning UAV-based concrete sounding.

S. Blaney and R. Gupta. UAV-based sounding of subsurface concrete defects.

In this paper, a UAV-based acoustic sounding device is evaluated using one of the concrete specimens from the concrete sounding work of Chapter 4. The performance of the acoustic sounding device in detecting and estimating the depth of the embedded defects in the concrete specimen is reported. Note that for this chapter defects numbered 1, 2, and 3 correspond to defects 8, 9, and 10 as numbered in Figure 4.5.

Abstract

A sounding technique that uses an unmanned aerial vehicle (UAV) equipped with two microphones can detect subsurface concrete defects and provide a basis for defect depth estimation. Current UAV-based inspection methods like optical and thermal imaging are typically limited to two-dimensional subsurface defect information. Since UAVs are known to generate noise in the frequency range of interest, three noise reduction measures for this sounding technique are assessed. Given adequate distance between the microphones and UAV, a two microphone signal subtraction technique and a spectral noise gating procedure are shown to decrease noise in the frequency range of interest. The spectral noise gating procedure yields substantially more noise reduction than the two-microphone approach.

5.1 Introduction

The feasibility of using a UAV as a platform from which a concrete sounding technique can be performed is investigated in this letter. Authors aim to determine the feasibility of detecting and estimating depth of defects via a UAV-based concrete sounding procedure. Three methods of mitigating UAV-noise are also explored.

Optical strategies [5] and passive thermal methods [26] have been evaluated for UAV-based inspection of concrete bridges. Crack detection is popular with optical inspection practices [21, 22, 53], and UAV-based two-dimensional surface location measurement of subsurface defects has been demonstrated [25]. UAV-based methods that can gauge depth such as UAV-based piezoelectric sensor placement [54] may be difficult to apply to concrete.

A percussion test is an alternative that uses the flexural frequency of the vibration response caused by a surface impact to estimate the depth of a subsurface defect [17]. A UAV with identical propellers to those used in this work has been shown to generate noticeable noise in the range from 100 Hz – 6 kHz [55], which overlaps the expected resonant flexural vibration frequencies of the concrete above shallow subsurface defects of a size and location roughly similar to this work, estimated using closed form solutions for vibrating plates. A noise reduction strategy needs to be undertaken to reduce the effect of aircraft noise on the desired acoustic content. Both closed form solutions [39, 43] and finite element models [42] have been used with success to relate defect depths to frequency of vibration from sounding information, concrete properties, and lateral dimensions.

5.2 Specimens

The primary specimen used in this letter is a 36×36×5.5 in (914×914×140 mm) concrete slab. Void defects are simulated by pieces of 1.5 in (38.1 mm) thick polystyrene foam embedded in the concrete. An image of a completed slab undergoing a test is shown in Figure 5.1. A control specimen identical to the first but without any defects is used to indicate the performance of undamaged concrete.

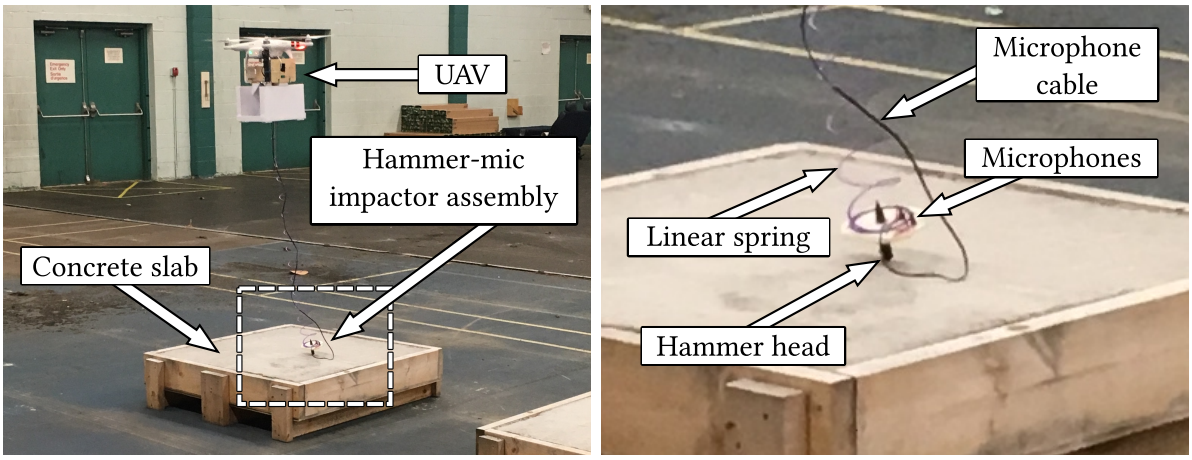

(a) (b)

Figure 5.1: (a) Image of a UAV test on the slab, (b) Enlarged view of impactor assembly during an impact.

There are four voids in the primary test slab, but only three (numbered 1, 2, and 3) were detected using the methods of sounding used. A control slab free of simulated defects was used to generate a control acoustic profile for defect-free concrete. Defect (i.e. void) depth (also referred to as the cover of a defect) is measured from the top concrete surface to the top of the embedded foam. The measured defect depths are shown in Figure 5.2 and Table 5.1. Slab concrete has a measured density of about 2300 kg/m^3 and average compressive strength at 80 days after casting of 23.6 MPa.

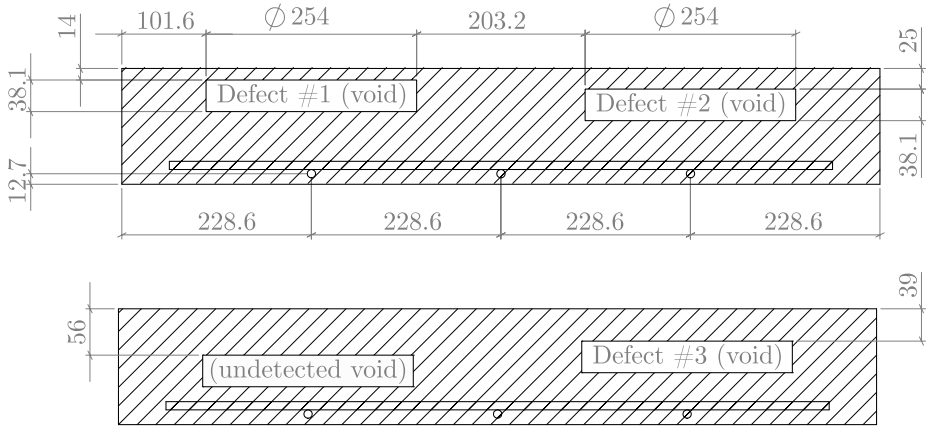

Figure 5.2: Section views of slab showing void cover dimensions (all values in mm).

5.3 Concrete sounding

Acoustic recordings were performed using a Polsen OLM-20 lavalier microphone and recorded by a Zoom H1 digital audio recorder. The OLM-20 contains two mono microphones; each was recorded to one channel of a stereo recording at a sampling rate of 96 kHz at 24 bit depth. The OLM-20 has a flat frequency response from 100 Hz to about 5 kHz. The flexural frequencies for the simulated defects in the slab have been previously measured and are all recorded below 5 kHz. The slab rests in the formwork during all sounding tests.

A 2 oz (57 g) ball pein hammer was used as an impactor to obtain reference percussion test measurements. The resonant frequencies are determined by locating the frequency at peak locations of FFTs of the audio recordings.

The UAV used for all experiments is a DJI Phantom 3 Standard equipped with DJI 9450 propellers. The impact device used on the UAV-based measurements consists of a ball-shaped steel hammer head (diameter roughly 12.4 mm) attached to a plastic linear spring. By carefully moving the UAV during flight, small vertical oscillations of the spring about an equilibrium extension can be induced as a means of impacting the top surface of the concrete above a defect location. This is one of the first studies to investigate such a setup. A diagram of the basic test setup is shown in Figure 5.3. Baseline results were generated by holding the impactor assembly by hand.

The equilibrium length is the spring length extended under load of the hammer impact assembly without the oscillations induced as part of the testing, so the exact distance between the aircraft and concrete surface for each equilibrium length may be slightly more than the reported value. The equilibrium lengths were tuned by increasing or decreasing the number of coils in the linear spring that were free to move. The acting stiffness of the spring increases or decreases accordingly. That is, the shorter equilibrium lengths have a higher spring constant and longer lengths have a lower spring constant. Impact with inadequate force will simply not be recognizable in the acoustic recording.

Using a hammer head with a roughly spherical shape (except for the connection point to the rest of the impactor assembly) means that even if the assembly is not perfectly oriented the impacts should be adequately consistent.

The frequency of the peaks in the FFTs of the acoustic signals can be used with concrete material properties and details of the lateral dimensions to estimate defect depth, which

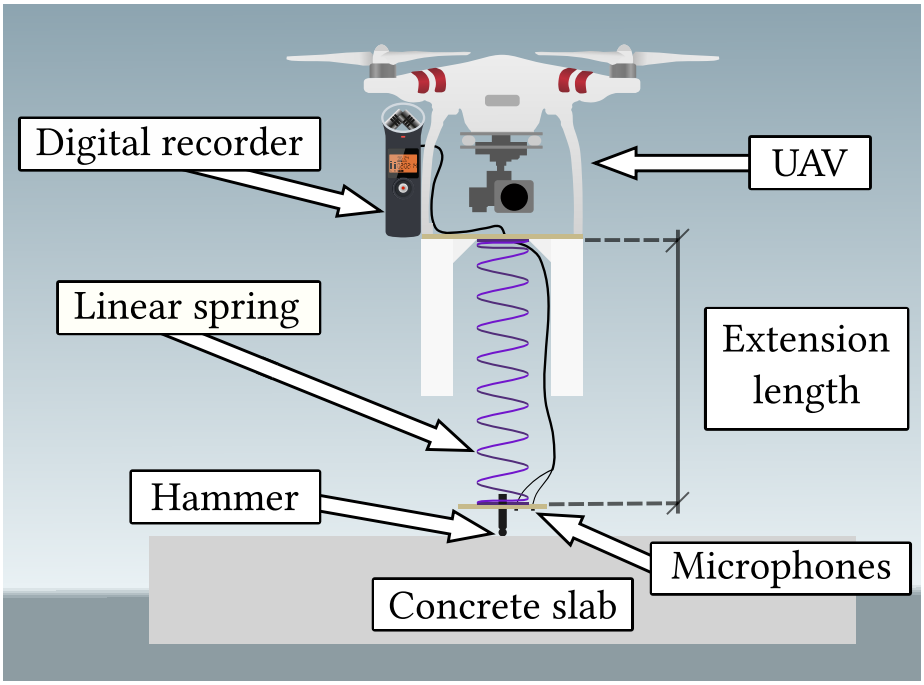

Figure 5.3: Diagram of basic UAV-based test setup.

has previously been done by Cheng et al.[39], among others. For flexural vibration, the depth of a defect is proportional to the fundamental frequency of vibration [52]. This means that even if there is not a reliable estimate of the concrete properties (as might be the case in damaged concrete), a depth from a single defect can be used with frequency and lateral size information of other defects to estimate depths of the other defects. Lateral size information of defects can be determined by a variety of methods, including UAV-based infrared thermography [25].

5.4 Noise Reduction Strategy

Three noise reduction measures were evaluated: a physical distance between the aircraft and microphones, a two-microphone setup for noise cancellation, and a noise reduction tool in the audio software.

The advantage of a separation between the aircraft and microphones is noise dissipation by the air between the UAV and the microphones at the end of the linear spring device. Measurements were taken at four equilibrium spring extension lengths: 18 in, 48 in, 60 in, and 120 in (0.46 m, 1.22 m, 1.52 m, 3.05 m respectively).

The two mono microphones, located at 1 in (25.4 mm) and 2 in (50.8 mm) lateral distance from the hammer head, can be used to perform some noise reduction. The microphones are recorded to separate audio channels in a stereo audio file. The microphones are significantly closer to the impact site than the aircraft, so the sound generated by the concrete strike changes a noticeable amount between the two microphones and the noise generated at the UAV changes comparatively little. The two mono signals are subtracted to create an audio file that has the UAV noise reduced by a greater amount than the impact sound. Audacity® audio software is used to perform the two-microphone noise reduction.

Audacity® also has a software-based noise reduction feature, which uses spectral noise gating. A section of the recording that contains only noise is used to establish noise characteristics, which are then applied to the recording of the impact and subsequent vibration to reduce noise.

5.5 UAV-based performance relative to baseline and reference results

The recorded frequency peaks for reference, baseline, and UAV-based measurements are shown in Table 5.1 for both the defects and the control slab.

Table 5.1: Frequencies of peaks for simulated subsurface voids.

Defect		Frequency of Peak (kHz)		
No.	Depth (mm)	Reference	Baseline	UAV-based
1	15	1.23	1.23	1.24
2	27	2.14	2.12	2.00
3	43	2.98	2.98	2.99
Ctrl	140	0.42	0.85	0.87

Peaks in the 300–500 Hz range (as measured during reference tests of the control slab) would be expected from the vibration of an entire slab. Baseline and control slab tests indicate that the microphone assembly may produce some vibration between 800 and 900 Hz (as observed in baseline and UAV-based control slab measurements). Broadband UAV noise from motors and propellers was recorded, but noise from interaction between propeller wash and the concrete surface is the most noticeable noise observed (mostly in the range of 0 to 500 Hz).

Overall, the peaks recorded in Table 5.1 indicate that defects 1, 2, and 3 can be detected by sounding from a UAV based platform at each of the four distances tested. The closeness of the UAV-based peaks to the reference and baseline peaks mean that any depths calculated using the UAV-based measurements will be roughly as the non-UAV-based methods.

5.6 Effect of noise reduction measures

The three noise reduction measures explored in this research include separation between the microphones and UAV, two mono signal combination, and the use of Audacity® spectral noise gating features.

There is no discernible effect on defect detectability directly attributable to increased equilibrium extension length between the aircraft and the concrete surface. Figure 5.4 shows the FFT for a strike above defect #1 before and after spectral gating noise reduction.

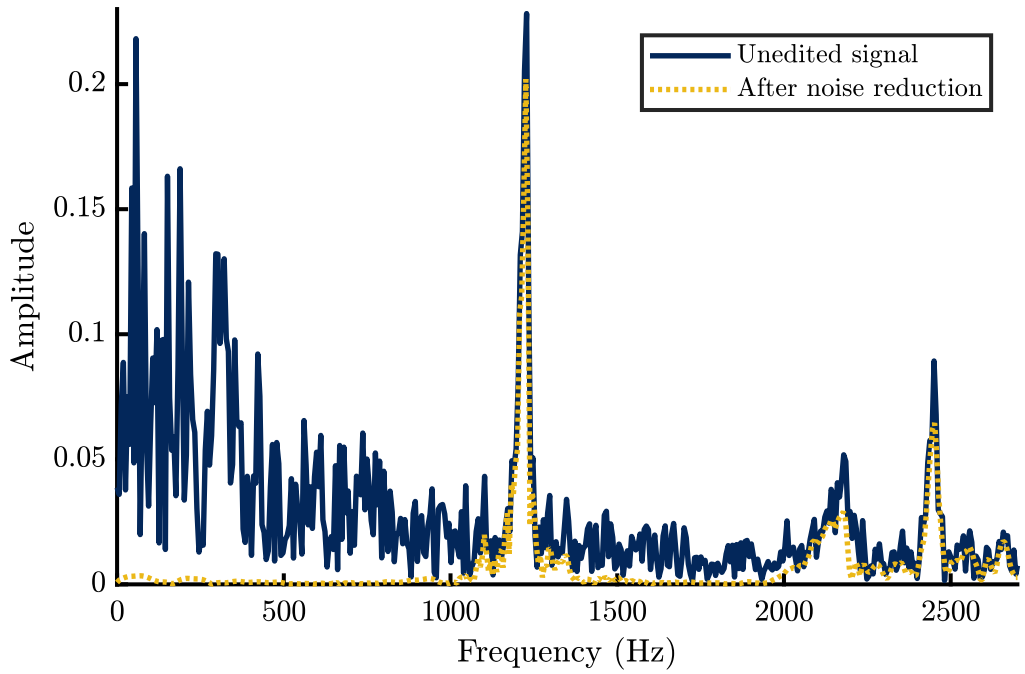

Figure 5.4: FFT of an impact recording at 60 in extension over defect #1, before and after noise reduction.

Short-time Fourier Transform spectrograms of a percussion test above defect #1 with a 60 in (1524 mm) equilibrium extension length are shown in Figure 5.5. The three spectrograms correspond to the three methods of noise reduction evaluated.

From Figure 5.5 it is observed that the mono signal subtraction produces some noise reduction, but the Audacity® spectral noise gating approach produces a far more thorough reduction. The sound of the aircraft moving prior to the strike is visualized in the pre-strike region on the spectrogram, to the left of the strike, by the roughly parallel striations. The strike is shown by the strong vertical feature that appears to bifurcate the spectrogram. After the strike, the aircraft moves closer to the concrete surface as the downward movement continues, resulting in a significant air draft caused by the propeller wash from the UAV interacting with the surface of the concrete. Air draft noise can also be seen in the pre-strike region, but is not as prominent. Since the source of this noise is in the immediate vicinity of both left and right microphones, the dual mono recording cannot correct the noise, as it occurs at comparatively different levels between the two recorded acoustic signals. However, because the aircraft noise shown by the parallel features before the strike occurs at a distance from the two mics, the two signals can be used to reduce this noise component.

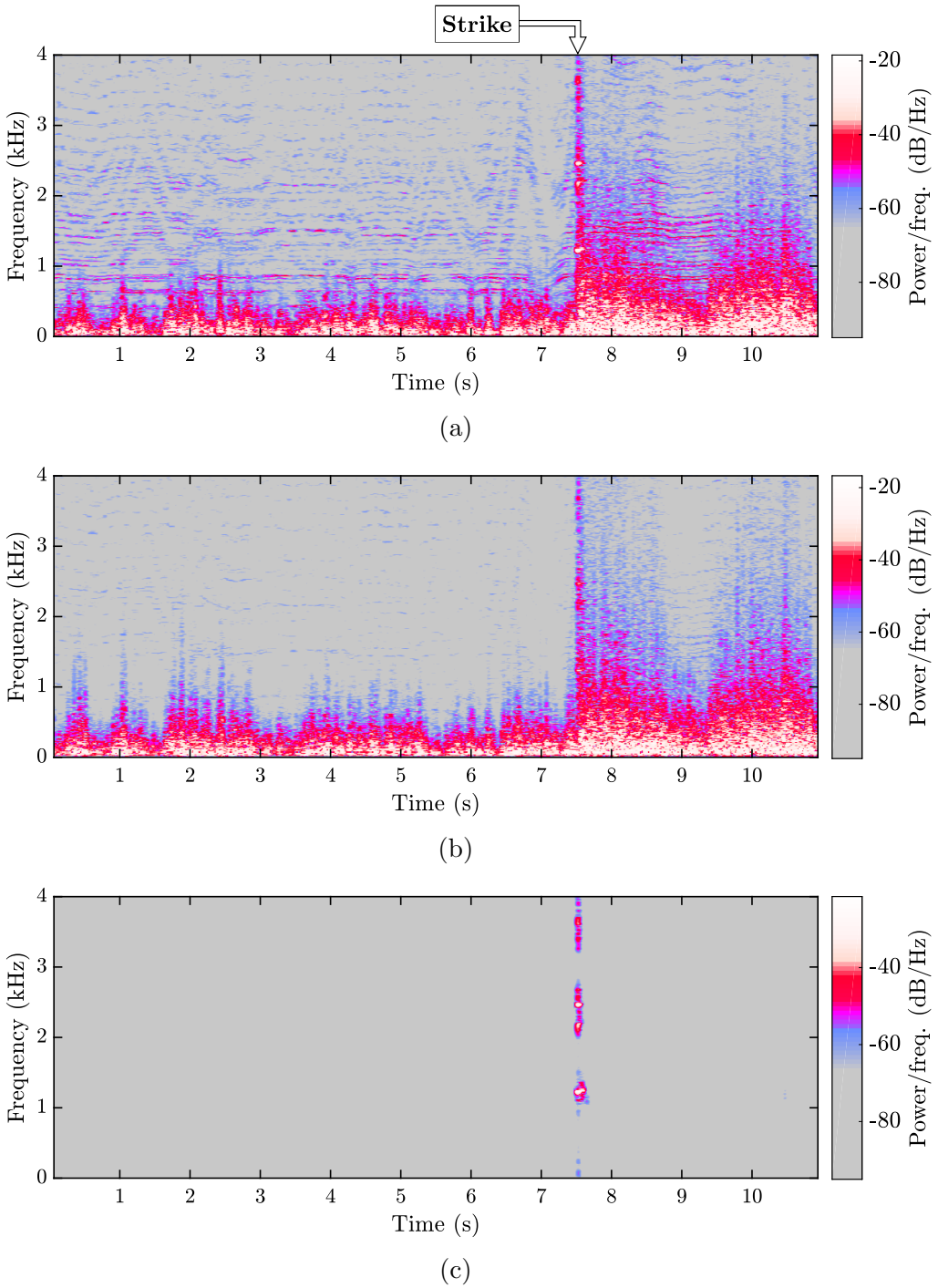

Figure 5.5: STFT spectrograms of a recording of an impact above defect #1 with (a) no noise reduction, (b) dual mono-mic noise reduction, (c) Audacity® spectral noise gating noise reduction.

Overall, the two mono signal combination can be said to yield some noise reduction in the 1 – 4 kHz range, but increases noise below 1 kHz. This offers an indication that the noise below 1 kHz is close to the mics and the noise above 1 kHz is distant noise. For

signals with noise created in the immediate vicinity of the impact area, the purely software-based approach produces much better results, and can eliminate most of the noise present in the signal. The software-based approach does ultimately greatly outperform the two-mic approach. However, the Audacity® noise reduction requires a recording of the noise that does not include the impact signal and also requires tuning of some parameters in the software to obtain the best result. The two-mic approach requires only a signal subtraction and is comparatively simple to perform, but does not reduce noise as well.This can be shown quantitatively by calculating the level of noise reduction in the first seven seconds of the recording shown in Figure 5.5. In the range of 0 – 1 kHz the 2-mic approach increases noise by 2.1 dB and the Audacity® noise gating reduces noise by 48.1 dB. However, in the 1 – 4 kHz range, the 2-mic approach reduces noise by 4.6 dB and the noise gating is consistent with a 48.1 dB noise reduction.

The noise caused by propeller wash and the associated interaction between it and the concrete surface can be mitigated by taking measurements in which the UAV and microphone location have some lateral separation. In other words, the air draft noise in the recording could likely be eliminated by moving the microphone and test location out of a region of expected propeller wash. For example, the microphone assembly could be mounted and oriented horizontally to the UAV.

5.7 Conclusion

A technique for UAV-based sounding of concrete defects has been demonstrated to have the capacity to detect some simulated subsurface void defects in a concrete sample. No significant effect of separation distance between the recording device and aircraft was observed. Noise reduction using both multiple recorded audio signals as well as Audacity® spectral noise gating was successful, although the software-based approach provided a greater level of noise reduction. Future work may wish to explore a greater range of concrete and aircraft parameters and better characterize the effects of distance and sound manipulation, but overall, it may be said that at least some degree of UAV-based concrete sounding is possible.

5.8 Acknowledgments

This research was supported by India-Canada IMPACTS and Networks of Centres of Excellence of Canada. Authors also acknowledge the assistance of fellow researchers and staff at the University of Victoria's Facility for Innovative Materials and Infrastructure Monitoring (FIMIM) in constructing specimens and conducting measurements.

Chapter 6

Implementation of UAV-based inspection methods

Prior chapters have focused on theoretical or specimen-based testing of UAV-based methods of inspection. In this chapter, the development of a UAV-compatible instrumentation platform with the capability to record and transmit images and data in real-time is presented. The design and preliminary prototype bench testing results for this Wighton-funded device are included. Also presented are the results of a concrete bridge deck inspection on an actual bridge currently in use over a forestry service road. Recommendations for future inspections are described.

Together, the development of the inspection platform system and the bridge inspection demonstrate practical implementations of some of the techniques described in earlier chapters.

6.1 A UAV-compatible Instrumentation Platform

A UAV-compatible instrumentation platform for infrastructure inspection was proposed for the 2017 Wighton Fund awards for product development. The project received funding and a prototype was constructed.

Sections 6.1 to 6.3 contain details and information from the original Wighton fund proposal from November 2016 as well as the follow-up progress report from November

2017. While Sean Blaney is the primary author of these original documents, suggestions and contributions to the project were made by the project leader Dr. Rishi Gutpa, as well as participants Harsh Rathod and Matthew Walker. Prototype construction and testing was conducted exclusively by Sean Blaney. Excerpts from the Wighton progress report, written by Sean Blaney, are used in Section 6.3.

6.2 Platform design

The proposed design called for a low-cost, UAV-compatible infrastructure inspection instrumentation platform, or the "i3P" for short. The i3P was intended as a low-cost alternative to more costly gimbal-based systems designed to carry and articulate scientific instruments on UAVs. For infrastructure inspection, these instruments can include optical and infrared cameras.

The i3P was designed to operate independently of the UAV on which it was mounted. In order for the i3P to be a self-contained system, it requires its own power source, control system, and data collection mechanism. The basic layout of i3P components and wired connections is shown in by the diagram in Figure 6.1. Connections are by pulse width modulation (PWM) or pulse position modulation (PPM).

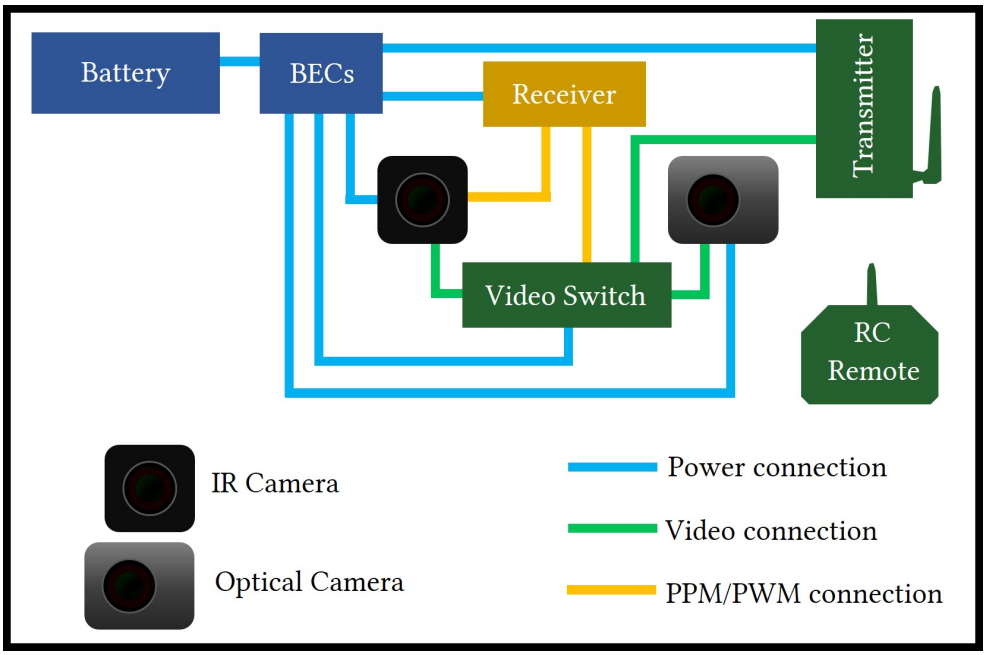

Figure 6.1: Diagram of i3P connections and layout.

Both an infrared (IR) and optical camera are shown in the system as their application to concrete and infrastructure inspection has been demonstrated [25]. In the future, hyper-spectral, optical laser, or acoustic methods may also become viable infrastructure tools for a UAV-based platform, and the i3P will potentially need future revisions to accommodate these payloads.

A battery provides power, and a battery eliminator circuit (BEC) is used to deliver regulated voltage to the components of the system. A receiver is present to receive control commands from an RC remote. A video switch can alternate between the infrared and optical camera video signal that is broadcast by a video transmitter to a digital video recorder and LCD monitor.

The physical design of the i3P system is articulated and capable of a variety of mounting positions on a UAV. By avoiding the active articulation found on gimbal-based systems, the i3P can be made less expensively than comparable gimbal systems. The electronic components of the i3P were designed to be placed in such a way so as to partially balance the weight of the cameras. Cameras are held on a platform supported by two positionable arms. This configuration is mindful of the impact of center of gravity changes to whichever aircraft on which the i3P is to be mounted. Renderings of the i3P design are shown in Figures 6.2 and 6.3.

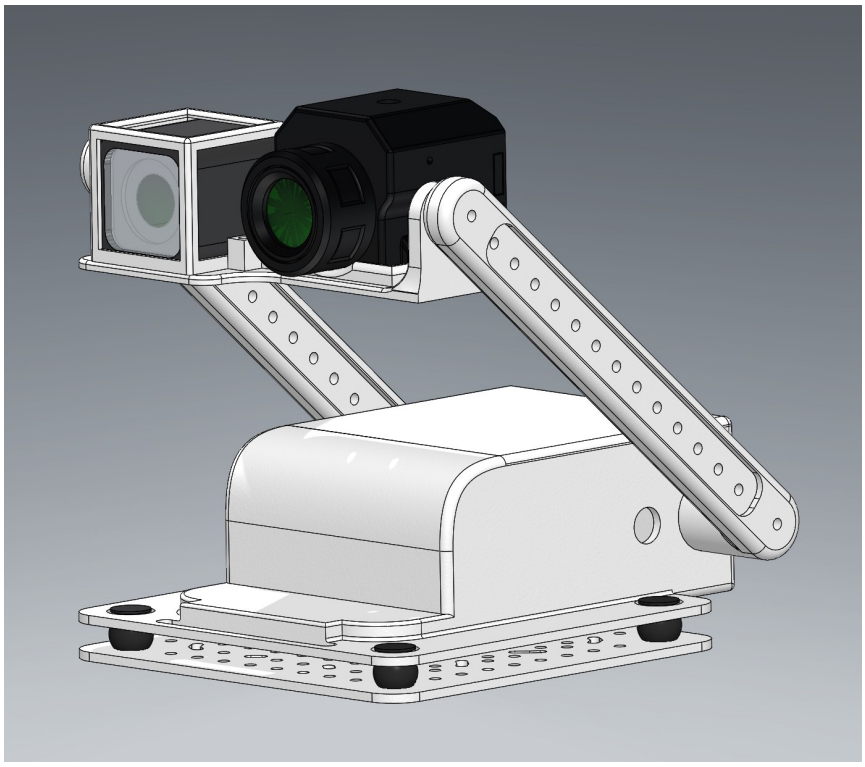

Figure 6.2: The i3P design with arms fixed in an upright position.

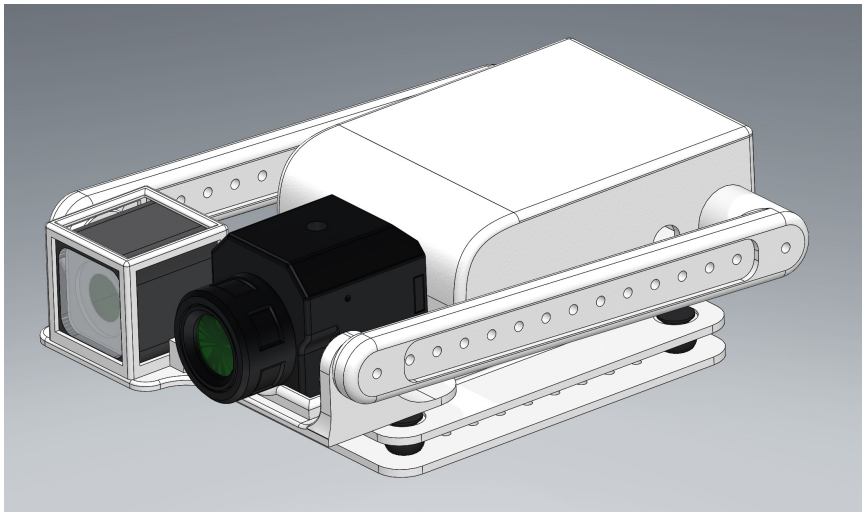

Figure 6.3: The i3P design with arms retracted.

6.3 Prototype

6.3.1 Materials and construction

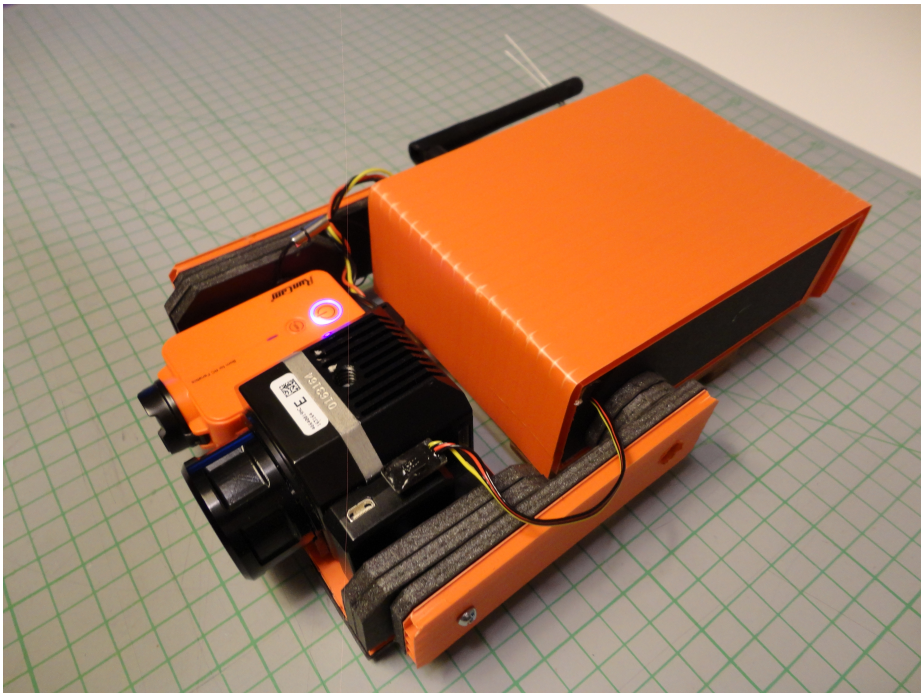

Figure 6.4: Overview of i3P prototype on a 1 cm by 1 cm grid.

An overview of the prototype of the i3P is shown in Figure 6.4. The i3P prototype body and arms are constructed of a custom foam board and Coroplast corrugated plastic laminate. The substructure of the i3P prototype is constructed of laser-cut 1/8 inch plywood held together using a contact cement product. These materials are extremely lightweight, inexpensive, and easy to work with. The black foam board product and orange Coroplast used offer a colour palette that matches the colours of the cameras selected for use with project. They are also highly visible, which is an important consideration for future use with an aircraft. The underside of the i3P showing the plywood frame is shown in Figure 6.5.

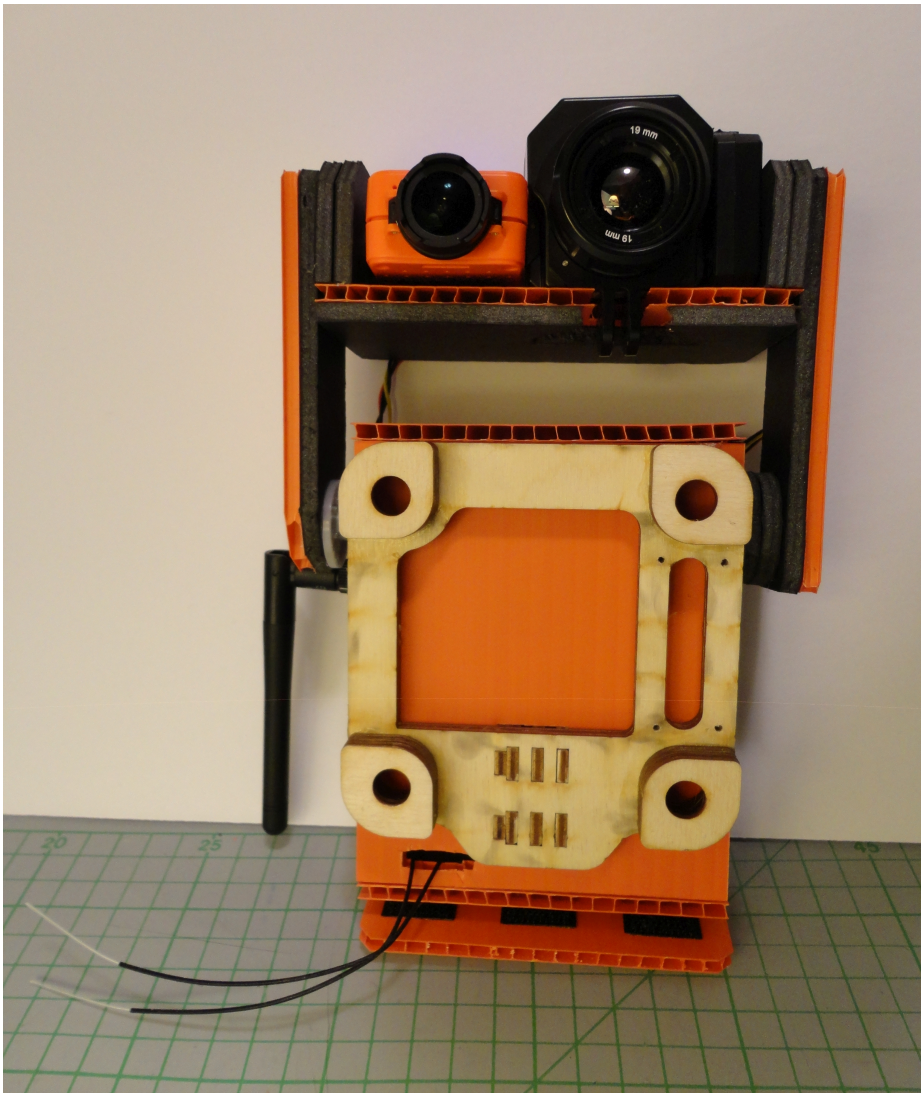

Figure 6.5: Underside of i3P prototype showing plywood frame. Pictured on a 1 cm by 1 cm grid.

6.3.2 Operation and features

The i3P prototype allows for control of imaging or other scientific payloads with real-time feedback viewable on a first-person-view monitor. Control is provided by a FrSky Taranis X9D Plus RC remote, and the feedback is displayed on an Eachine brand LCD monitor. A view of the feedback from the thermal camera is shown during a bench test in Figure 6.6.

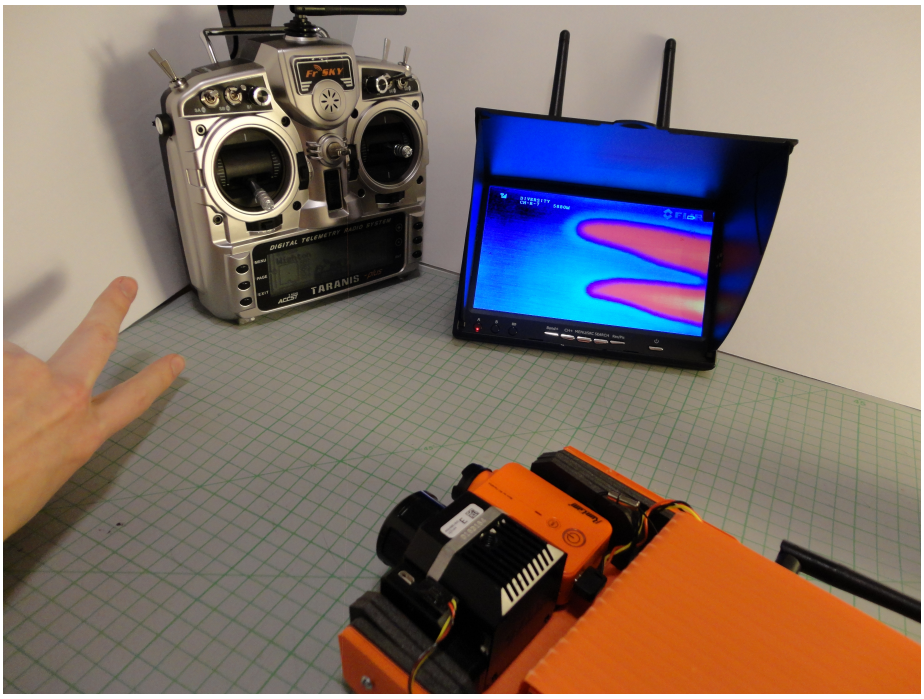

Figure 6.6: i3P prototype imaging Sean Blaney's fingers and relaying the image to the video monitor. Pictured on a 1 cm by 1 cm grid.

The i3P features an articulated platform for two cameras: a Runcam 2 HD optical camera and a FLIR Vue Pro thermal camera. The platform is connected via two arms to the main body of the i3P. The body of the i3P features a laser-cut plywood construction that can be used with rubber vibration dampers to connect the entire assembly to a four-corner gimbal mount on a multirotor UAV. The cameras pivot where they are connected to the arms, and the arms pivot at their connection to the i3P main body. The arm position is determined by a servo motor built-in to one of the arms, and controlled via the Taranis XD9 Plus.

The video is broadcast over a different frequency than the control link used to control the arms, and the video transmitter has a separate antenna that protrudes from the side of the i3P body to this end. Either camera may be used as the video source. A video channel switcher was tested to attempt remote video source signal switching, but the switch evaluated did not perform adequately. It may be advisable to implement RC-controlled video switching in the future.

The internal components of the i3P are accessed by opening the top panel, which is currently secured using fabric hook and loop fastening tape.

Further images of the i3P prototype are shown in Appendix C.

6.4 Skutz River Bridge Inspection

To gauge the performance of two of the most prominent means of UAV-based inspection of concrete infrastructure, an inspection of a bridge with a concrete deck was performed. The Skutz Bridge, located in the Cowichan Valley Regional District in British Columbia (BC), was inspected by UAV-based optical and infrared cameras. The Skutz Bridge spans the Cowichan River and is in Cowichan River Provincial Park. The BC Ministry of Forests, Lands and Natural Resource Operations is responsible for operating and maintaining the bridge.

6.5 Legal use of research UAVs in Canada

In Canada, use of UAVs for research requires a Special Flight Operations Certificate (SFOC) from Transport Canada. The imaging of the Skutz River Bridge described herein was performed with an SFOC issued to Sean Blaney operating as a representative of the University of Victoria Department of Civil Engineering.

6.6 Skutz Bridge and imaging conditions

The Skutz Bridge is part of the Skutz Falls Forestry Service Road (Mayo Rd.). Appropriate arrangements were made with the BC Ministry of Forests, Lands and Natural Resource Operations to close the bridge to vehicle and pedestrian traffic for the duration of flight operations.

The bridge inspection took place on 15 March 2018. Flight operations commenced at 09:37 PDT and concluded at 10:32 PDT. The weather in the area during the inspection was sunny with scattered clouds. Sunrise was at 07:26 PDT, so the bridge had not yet received three direct hours of sunlight as per ASTM 4788 – 03 [34]. Additionally, the bridge deck contained some debris, primary at edges of the roadway. Debris appeared to be mostly dirt, gravel, and decomposed local vegetation.

The bridge deck is partially obscured from sunlight due to the surrounding woodlands. Essentially, trees at both edges of the bridge and along the river banks cast shadows over the bridge deck.

The bridge deck was imaged using the Phantom 3 Standard equipped with a FLIR Vue Pro infrared camera. Optical video as well as infrared video and images were captured at a variety of heights above the deck. Infrared images and video were captured at a resolution of 640 × 512 pixels. The FLIR Vue Pro used was not radiometric, so no absolute values for temperature data are available from the images. Optical video was recorded at a frame width of 2704 pixels and height of 1520 pixels. The i3P was not used during the Skutz Bridge Inspection as the Phantom 3 Standard requires the built-in camera gimbal system to fly and cannot carry the i3P.

6.7 Skutz Bridge deck imaging results

The Skutz Bridge is a relatively new bridge. As such, it comes as no surprise that no defects are observable in the optical footage of the bridge. The steel bridge deck railings and divider between the vehicle and pedestrian areas of the bridge are clear in the visual images, as are the areas of the bridge deck covered in the scattering of debris. An optical image of the bridge deck is shown in Figure 6.7.

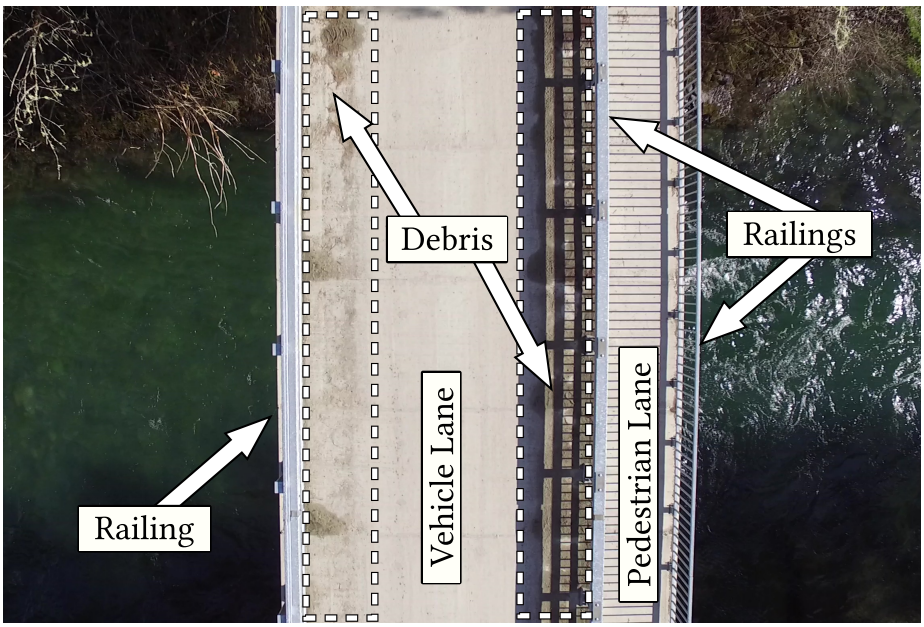

Figure 6.7: Overview of Skutz bridge elements visible in optical images.

Infrared video of the bridge deck captured in close proximity is difficult to garner information from. The limited distance and temperature range coupled with the aircraft movement appear to make it difficult for the camera to adequately image the deck. Still

infrared images captured at a greater distance from the bridge deck are more insightful. In these images there are a number of distinctions that can be made between different areas of the bridge. The railings cast shadows on the bridge deck, and the areas in the shadow are cooler than those in direct sunlight. Shadows appear to have a major impact on the infrared images. Figure 6.8 shows an optical and infrared image taken within about one second of each other.

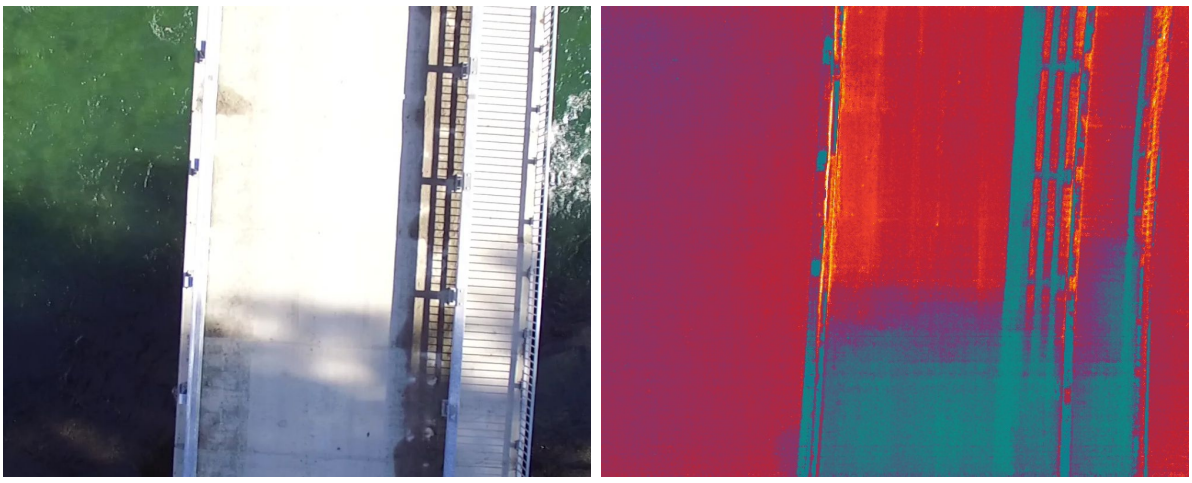

(a) Optical image. (b) Infrared image.

Figure 6.8: Optical and infrared images of the Skutz bridge deck displaying the impact of shadows.

The IR image has a narrower field of view and covers less area, but it can be observed that the cooler areas of the bridge correspond to those areas that are under the cover of shadows. The shadow from the railing is pronounced in the top of the image which shows a portion of the bridge deck in direct sunlight, but becomes more obscure in the region of the bridge that is also under the shadows from nearby trees.

The potential impact of shadows on the ability to detect potential defects may indicate that the bridge deck to be imaged needs to have received at least several hours of direct sunlight prior to infrared imaging to obtain results that are consistent between different areas of the bridge. This may be especially true for radiometric comparisons between different areas of the bridge, which was not included with these images.

Other images show that debris on the bridge deck is also something that may pose an issue for infrared inspection via UAV. Higher temperatures observed on the left side of the bridge deck appear to correspond to debris. Figure 6.9 shows roughly similar areas of the bridge in both optical and thermal images.

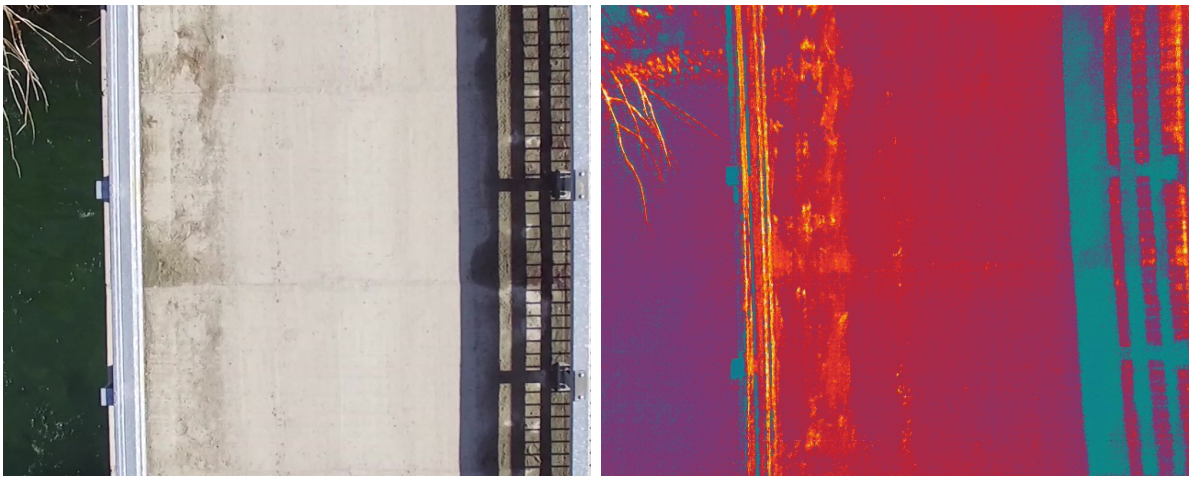

(a) Optical image. (b) Infrared image.

Figure 6.9: Optical and thermal images of the Skutz bridge deck debris.

The shape and size of the increased temperature areas on the left hand side of the bridge deck shown in the thermal image in Figure 6.9b appear to correspond to those areas that are shown covered in some type of debris in Figure 6.9a. Debris on the other side of the roadway on the bridge would be obscured by the shadow of the railing that divides the pedestrian and vehicle lanes. Aberration in the IR image is more noticeable than in the optical image.

6.8 Bridge deck shadow area comparison

To gauge the accuracy of the infrared imaging, it is useful to compare optical and infrared images. The optical image has a much greater resolution, so it is used as a benchmark. If the infrared image is as accurate as the optical image, then the area of the divider shadow on the bridge deck should be the same in both images. The results will be applicable only to the camera combination used in this inspection, but offer insight into a means of comparison between a reference size and the infrared image.

To compute the area, an infrared and optical image taken within one second of each other are processed using MATLAB® to isolate the shadow area in each image. Each image is first converted to the CIE (International Commission on Illumination) 1976 L*a*b colour space, also called the "CIELAB" colour space. This colour space represents the colours in the image as three values, much like the familiar RGB colour system, but is device independent. The CIELAB colour space is perceptually uniform; the Euclidean

distance between two colours is roughly the perceptual difference between the colours (how different they look to the human eye).

The perceptual uniformity is helpful in isolating the shadow region from the rest of the image. A reference pixel within the shadow in the CIELAB version of the image is used to compute the square of the distances between the reference point and all other pixels on the image. This representation indicates the closeness in colour of all other pixels to the reference pixel. The computed closeness matrix can be subsequently transformed into a grayscale image in which darker pixels indicate a closeness of colour between a pixel and the reference pixel, and lighter pixels represent less similar colours. In the grayscale image, the reference pixel is used to compute a contiguous region with similar gray values. The contiguous area determined is the area of the shadow in the image. The result is converted to a binary black and white image to compute the area of the shadow in each image in pixels.

To obtain a scale in both images, a meters per pixel ratio is determined by using the width of the bridge deck in both images. The actual width of the bridge deck is about 7.126 m. In the optical image the bridge deck is 579 pixels, and in the infrared image it is 361 pixels.

The computed area for the divider shadow on the bridge deck between three support posts is 5.2 m^2 for the infrared image and 5.7 m^2 for the optical image. There is to be some expected difference between the two areas, given the reduced pixel resolution of the infrared image. An overview of the images indicates the shadow in the infrared image has less well-defined edges and more rounded corners in comparison to the optical image. The infrared image also appears to display more aberration in comparison to the optical image. The percent error between the infrared and optical image is 9.7 %. Optical and infrared images of the bridge before and after modification to isolate the divider shadow are shown in Figures 6.10 and 6.11.

6.9 Skutz Bridge deck inspection conclusions

There are no obvious signs of damage or delamination defects in the Skutz bridge deck shown in the infrared or optical images recorded. The images in Figures 6.8 and 6.9 indicate that future inspections should be mindful of the lighting conditions of the bridge including the location of shadows, as well as any debris that lies on the surface of the bridge.

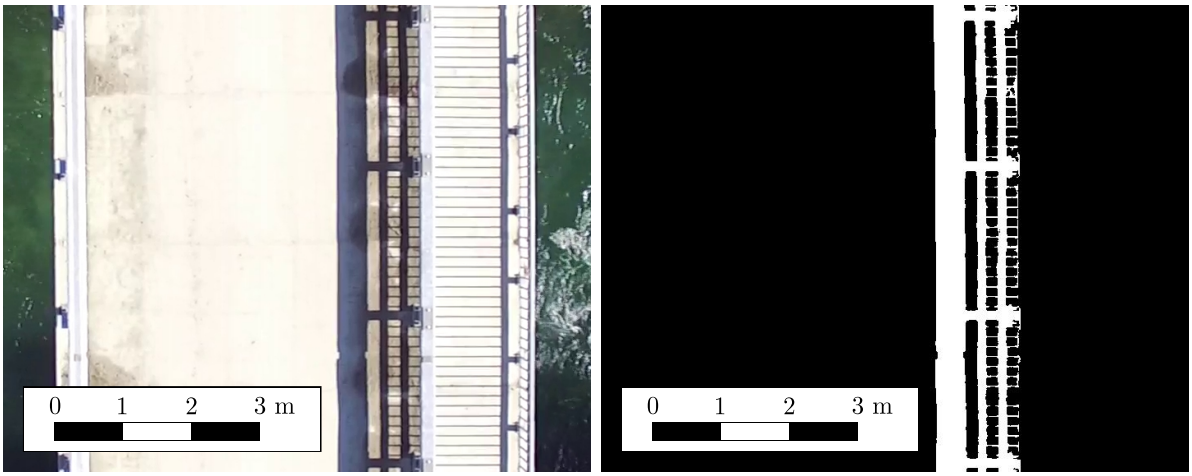

(a) Original image. (b) Shadow-isolated black and white image.

Figure 6.10: Optical images of the Skutz Bridge deck divider shadow.

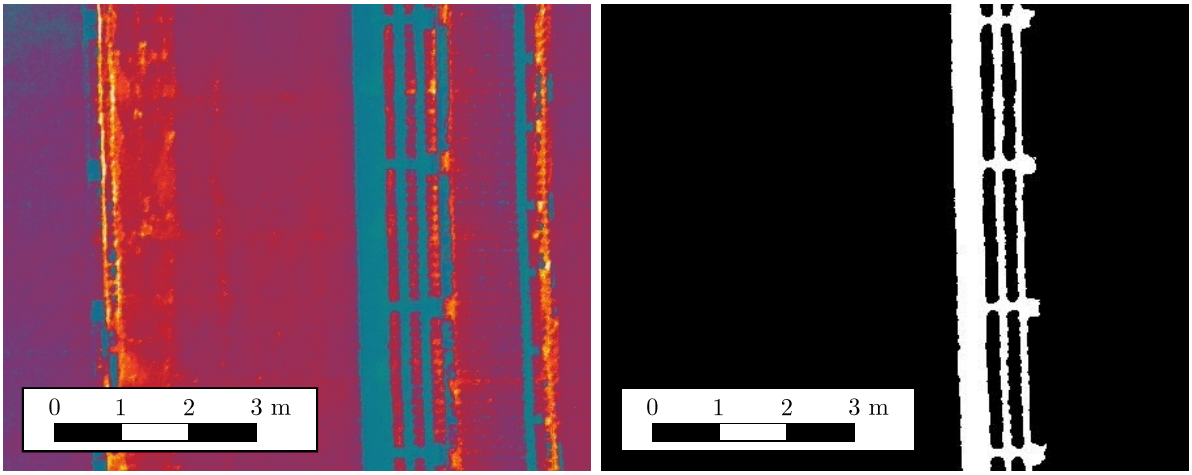

(a) Original image. (b) Shadow-isolated black and white image.

Figure 6.11: Infrared images of the Skutz Bridge deck divider shadow.

Chapter 7

Conclusions

With respect to the original objectives outlined in Section 1.2, the following conclusions can be made:

1. Though speaker-based excitation for concrete sounding shows promise, hammer percussion offered the best performance in terms of defects detected and depth estimation accuracy when recorded using a microphone and digital recorder.

2. A linear inspection strategy should consider the effects of camera distance and aircraft speed in deciding on a flight program.

3. The UAV-based infrared camera is capable of detecting near-surface voids and delaminations induced in concrete test specimens.

4. A UAV-based hammer impactor is capable of detecting and estimating depth of subsurface voids in a concrete sample. Microphones record the acoustic response of the flexural vibration and the frequency content is analyzed to estimate depth.

5. An instrumentation system anointed the "i3P" was developed and houses an optical and thermal camera with live image broadcasting and recording capability. It is made of low-cost materials and its articulated arms are capable of a variety of fixed positions.

6. An inspection of the Skutz Bridge in Cowichan River Provincial Park indicates that shadows and debris are concerns for UAV-based thermal bridge inspections.

7.1 Future work

Future work should continue along two avenues of exploration. First, optical and thermal methods need to be improved in performance and better understood. Second, improvements to UAV-based concrete sounding techniques and equipment are required for the method to become an effective complement or alternative to optical or infrared methods.

7.1.1 Optical and thermal methods

The optical and infrared methods used in the inspection of the Skutz Bridge inspection should be combined into an integrated platform like the i3P or a commercially available multi-camera gimbal device. For example, UAVs with better positioning and communication equipment than the DJI Phantom 3 Standard used in Chapters 2, 3, 5,and 6 are capable of carrying upward-facing cameras for inspection of the underside of bridge decks.

For optical imaging, blur estimation that considers more complicated aircraft movement may be of use when trying to design a flight strategy or select an appropriate camera or lens. The crack detection and image analysis presented in this thesis utilizes simple thresholding techniques that could be potentially improved by using edge detection or other methods. No corrections for image aberration were performed on any images used in this work, so implementation of aberration correction in images stands as a possible improvement. The effect of the lighting or other ambient conditions on optical imagery may also be of interest if future bridge inspections may include areas that are out of direct sunlight or other lighting. To this end, a camera calibration could be used to estimate both radial and tangential distortion as well as camera intrinsics and extrinsics.

The effects of defect depth, size, and type on the effectiveness of UAV-based infrared thermography are of interest. While the results in Chapter 3 offer some insight into the effect of depth and lateral size, comprehensive studies of these parameters are required to provide statistically significant conclusions. Radiometric infrared thermography (capable of gauging temperature values) may be useful in comparing different test samples or defect parameters. Camera calibration for the IR camera would likely be required for flight planning of the type described for the optical camera.

7.1.2 UAV-based concrete sounding

While the results shown in Chapter 5 offer proof that UAV-based concrete sounding is possible, they do little to characterize performance in terms of the concrete or defect parameters. The method of concrete excitation is of particular interest. The linear spring impactor assembly used in Chapter 5 is likely better replaced with an actively controlled or actuated mechanism. The effect of the impactor size and shape is not well understood, nor is the type of impact that produce the best results in terms of detection accuracy and speed. Several impactors may want to be combined into a single delivery system to cover larger areas of concrete. The position and location of the impactor relative to the UAV on which it is mounted appears to be of some concern. Placing the impactor in a place that is affected by the propeller wash (as was done in Chapter 5) appears to create noise.

Noise parameters of the particular UAV used during any UAV-based sounding work are an important consideration for future work. The work conducted in Chapter 5 was conducted indoors. Infrastructure inspection occur outdoors, so the effects of noise from sources like traffic and wind need to be explored. The effects of varying concrete and defect parameters on the effectiveness of sounding methods are also of interest.

References

[1] Sardar Kashif Ur Rehman, Zainah Ibrahim, Shazim Ali Memon, and Mohammed Jameel. Nondestructive test methods for concrete bridges: A review. *Construction and Building Materials*, 107(Supplement C):58 – 86, 2016. ISSN 0950-0618. doi:10.1016/j.conbuildmat.2015.12.011. URL http://www.sciencedirect.com/science/article/pii/S0950061815306905.

[2] ASTM D4580 / D4580m-12, Standard Practice for Measuring Delaminations in Concrete Bridge Decks by Sounding. Technical report, ASTM International, West Conshohocken, PA, 2012. URL http://www.astm.org/cgi-bin/resolver.cgi?D4580D4580M-12.

[3] ASTM C1383-15, Standard Test Method for Measuring the P-Wave Speed and the Thickness of Concrete Plates Using the Impact-Echo Method. Technical report, ASTM International, West Conshohocken, PA, 2015. URL http://www.astm.org/cgi-bin/resolver.cgi?C1383-15.

[4] ASTM C597-16, Standard Test Method for Pulse Velocity Through Concrete. Technical report, ASTM International, West Conshohocken, PA, 2016. URL http://www.astm.org/cgi-bin/resolver.cgi?C597-16.

[5] Norman Hallermann and Guido Morgenthal. Visual inspection strategies for large bridges using Unmanned Aerial Vehicles (UAV). pages 661–667, July 2014. doi:10.1201/b17063-96.

[6] Canadian Infrastructure Report Card (CIRC). The Canadian Infrastructure Report Card 2016. Technical report, 2016.

[7] American Society of Civil Engineers. 2017 Infrastructure Report Card. Technical report, 2017.

[8] DJI Enterprise. DJI Introduces M200 Series Drone Built For Enterprise Solutions, February 2017. URL https://www.dji.com/newsroom/news/dji-introduces-m200-series-drones-built-for-enterprise-solutions.

[9] Ascending Technologies. UAV Inspection & Monitoring. URL http://www.asctec.de/en/uav-uas-drone-applications/aerial-inspection-aerial-monitoring/.

[10] Global Market Insights. Commercial Drone Market Outlook - UAV Industry Size Forecast 2024, February 2018. URL https://www.gminsights.com/industry-analysis/unmanned-aerial-vehicles-UAV-commercial-drone-market.

[11] ASTM E1316-16a, Standard Terminology for Nondestructive Examinations. Technical report, ASTM International, West Conshohocken, PA, 2016. URL http://www.astm.org/cgi-bin/resolver.cgi?E1316-16a.

[12] Nicholas J Carino. Impact Echo: The Fundamentals. In *International Symposium on Non-Destructive Testing in Civil Engineering*, 2015.

[13] Xianglei Ni, Piervincenzo Rizzo, and Chiara Daraio. Novel sensor technology for NDE of concrete. In *Sensors and Smart Structures Technologies for Civil, Mechanical, and Aerospace Systems 2009*, volume 7292, pages 729218–1–729218–9, 2009. doi:10.1117/12.815510. URL http://dx.doi.org/10.1117/12.815510.

[14] Chi-Won In, Fabian Schempp, Jin-Yeon Kim, and Laurence J. Jacobs. A Fully Noncontact, Air-Coupled Ultrasonic Measurement of Surface Breaking Cracks in Concrete. *Journal of Nondestructive Evaluation*, 34(1):272, November 2014. ISSN 1573-4862. doi:10.1007/s10921-014-0272-6. URL https://doi.org/10.1007/s10921-014-0272-6.

[15] Jinying Zhu and John S. Popovics. Imaging concrete structures using air-coupled impact-echo. *Journal of Engineering Mechanics - ASCE*, 133(6):628–640, June 2007. ISSN 0733-9399. doi:10.1061/(ASCE)0733-9399(2007)133:6(628).

[16] Taekeun Oh, Seong-Hoon Kee, Ralf W. Arndt, John S. Popovics, and Jinying Zhu. Comparison of NDT Methods for Assessment of a Concrete Bridge Deck. *Journal of Engineering Mechanics*, 139(3):305–314, 2013. doi:10.1061/(ASCE)EM.1943-7889.0000441. URL https://ascelibrary.org/doi/abs/10.1061/%28ASCE%29EM.1943-7889.0000441.

[17] Hongbin Sun, Jinying Zhu, and Suyun Ham. Acoustic evaluation of concrete delaminations using ball-chain impact excitation. *The Journal of the Acoustical Society of America*, 141(5):EL477–EL481, 2017. doi:10.1121/1.4983343. URL http://dx.doi.org/10.1121/1.4983343.

[18] Tsuneyoshi Sugimoto, Itsuki Uechi, Kazuko Sugimoto, Noriyuki Utagawa, and Kageyoshi Katakura. Study on the Non-contact Acoustic Inspection Method for Concrete Structures by using Strong Ultrasonic Sound source. *Proceedings of the 2015 ICU International Congress on Ultrasonics, Metz, France*, 70:398–401, January 2015. ISSN 1875-3892. doi:10.1016/j.phpro.2015.08.115. URL http://www.sciencedirect.com/science/article/pii/S1875389215008561.

[19] Mahendra P. Singh, Bijan Khaleghi, Vijay K. Saraf, Sudhir K. Jain, Gary Norris, Rajiv Goel, and C. V. R. Murty. Roads and Bridges. *Earthquake Spectra*, 18(S1): 363–379, July 2002. ISSN 8755-2930. doi:10.1193/1.2803920. URL https://doi.org/10.1193/1.2803920.

[20] Christian Eschmann, Chen-Ming Kuo, Chung-Hsin Kuo, and Christian Boller. Unmanned aircraft systems for remote building inspection and monitoring. volume 36, January 2012.

[21] A. Ellenberg, L. Branco, A. Krick, I. Bartoli, and A. Kontsos. Use of Unmanned Aerial Vehicle for Quantitative Infrastructure Evaluation. *Journal of Infrastructure Systems*, 21(3):04014054, September 2015. doi:10.1061/(ASCE)IS.1943-555X.0000246. URL https://doi.org/10.1061/(ASCE)IS.1943-555X.0000246.

[22] G. Morgenthal and N. Hallermann. Quality Assessment of Unmanned Aerial Vehicle (UAV) Based Visual Inspection of Structures. *Advances in Structural Engineering*, 17(3):289–302, March 2014. ISSN 1369-4332. doi:10.1260/1369-4332.17.3.289. URL https://doi.org/10.1260/1369-4332.17.3.289.

[23] H Kim, SH Sim, and S Cho. Unmanned aerial vehicle (UAV)-powered concrete crack detection based on Digital Image Processing. pages 1–2, 2015.

[24] S. Sankarasrinivasan, E. Balasubramanian, K. Karthik, U. Chandrasekar, and Rishi Gupta. Health Monitoring of Civil Structures with Integrated UAV and Image Processing System. *Eleventh International Conference on Communication Networks, ICCN 2015, August 21-23, 2015, Bangalore, India Eleventh International Conference*

on Data Mining and Warehousing, ICDMW 2015, August 21-23, 2015, Bangalore, India Eleventh International Conference on Image and Signal Processing, ICISP 2015, August 21-23, 2015, Bangalore, India, 54:508–515, January 2015. ISSN 1877-0509. doi:10.1016/j.procs.2015.06.058. URL http://www.sciencedirect.com/science/article/pii/S1877050915013824.

[25] A. Ellenberg, A. Kontsos, F. Moon, and I. Bartoli. Bridge deck delamination identification from unmanned aerial vehicle infrared imagery. *Automation in Construction*, 72:155–165, December 2016. ISSN 0926-5805. doi:10.1016/j.autcon.2016.08.024. URL http://www.sciencedirect.com/science/article/pii/S0926580516301789.

[26] Jennifer Zink and Barritt Lovelace. Unmanned aerial vehicle bridge inspection demonstration project. Technical Report MN/RC 2015-40, Minnesota Department of Transportation, July 2015. URL http://www.dot.state.mn.us/research/TS/2015/201540.pdf.

[27] Charles S. Johnson, Jr. *Science for the curious photographer: an introduction to the science of photography.* Number Book, Whole. Routledge, New York, New York;London, [England];, second edition, 2017. ISBN 9781351811859;1351811851;0415793262;9780415793261;.

[28] Mark R. Nissen. Image blur. Technical Report SAND–93-0644, Sandia National Labs, Albuquerque, NM (United States), April 1993. doi:10.2172/10176898.

[29] D.J. Schroeder. *Astronomical Optics*. Elsevier Science, 2012. ISBN 978-0-323-13856-7.

[30] E. Allen and S. Triantaphillidou. *The Manual of Photography*. Elsevier/Focal Press, 2011. ISBN 978-0-240-52037-7.

[31] A.R. Greenleaf. *Photographic optics*. Photographic Optics. Macmillan, New York, 1950.

[32] How to find the length of an object in an image? - MATLAB Answers - MATLAB Central, . URL https://www.mathworks.com/matlabcentral/answers/163290-how-to-find-the-length-of-an-object-in-an-image?requestedDomain=true.

[33] What is camera calibration? - MATLAB Simulink, . URL https://www.mathworks.com/help/vision/ug/camera-calibration.html.

[34] ASTM D4788-03(2013), Standard Test Method for Detecting Delaminations in Bridge Decks Using Infrared Thermography. Technical report, ASTM International, West Conshohocken, PA, 2013. URL http://www.astm.org/cgi-bin/resolver.cgi?D4788-03(2013).

[35] Ali A. Sultan and Glenn Washer. A pixel-by-pixel reliability analysis of infrared thermography (IRT) for the detection of subsurface delamination. *NDT & E International*, 92:177 – 186, 2017. ISSN 0963-8695. doi:10.1016/j.ndteint.2017.08.009. URL http://www.sciencedirect.com/science/article/pii/S0963869516301499.

[36] L. E. Mavromatidis, J.-L. Dauvergne, R. Saleri, and J.-C. Batsale. First experiments for the diagnosis and thermophysical sampling using pulsed IR thermography from unmanned aerial vehicle (UAV). In *Proceedings of the 2014 International Conference on Quantitative InfraRed Thermography*. QIRT Council, 2014. doi:10.21611/qirt.2014.213. URL https://doi.org/10.21611/qirt.2014.213.

[37] Shuhei Hiasa, Recep Birgul, and F. Necati Catbas. Effect of Defect Size on Subsurface Defect Detectability and Defect Depth Estimation for Concrete Structures by Infrared Thermography. *Journal of Nondestructive Evaluation*, 36(3):57, July 2017. ISSN 1573-4862. doi:10.1007/s10921-017-0435-3. URL https://doi.org/10.1007/s10921-017-0435-3.

[38] Sean Blaney and Rishi Gupta. Sounding of subsurface concrete defects using frequency response of flexural vibration. *Cement and Concrete Composites*, 92:155–164, September 2018. ISSN 0958-9465. doi:10.1016/j.cemconcomp.2018.06.006. URL https://www.sciencedirect.com/science/article/pii/S095894651731185X.

[39] Chia-Chi Cheng, Tao-Ming Cheng, and Chih-Hung Chiang. Defect detection of concrete structures using both infrared thermography and elastic waves. *Automation in Construction*, 18(1):87 – 92, 2008. ISSN 0926-5805. doi:10.1016/j.autcon.2008.05.004. URL http://www.sciencedirect.com/science/article/pii/S0926580508000812.

[40] C. Cheng and M. Sansalone. The impact-echo response of concrete plates containing delaminations: numerical, experimental and field studies. *Materials and Structures*, 26(5):274–285, June 1993. doi:10.1007/bf02472949. URL https://doi.org/10.1007/bf02472949.

[41] Huadong Wu and M. Siegel. Correlation of accelerometer and microphone data in

the "coin tap test". *IEEE Transactions on Instrumentation and Measurement*, 49(3): 493–497, June 2000. ISSN 0018-9456. doi:10.1109/19.850382.

[42] Masanori Asano, Toshiro Kamada, Minoru Kunieda, Keitetsu Rokugo, and Ichiro Kodama. Impact acoustics methods for defect evaluation in concrete. In *Proceedings International Symposium Non-Destructive Testing in Civil Engineering (NDT-CE), Berlin*, 2003.

[43] Roberto Felicetti. Assessment of an industrial pavement via the impact acoustics method. *European Journal of Environmental and Civil Engineering*, 14(4):427–439, 2010. ISSN 1964-8189. doi:10.1080/19648189.2010.9693235.

[44] N. J. Carino. Training: Often the missing link in using NDT methods. *Construction and Building Materials*, 38(Supplement C):1316 – 1329, 2013. ISSN 0950-0618. doi:10.1016/j.conbuildmat.2011.03.060. URL http://www.sciencedirect.com/science/article/pii/S0950061811001061.

[45] Mary Sansalone and Nicholas J. Carino. Impact-Echo: A Method for Flaw Detection in Concrete Using Transient Stress Waves. Technical Report NBSIR 86-3452, National Bureau of Standards, September 1986.

[46] Hiroshi Haya, Xiu Luo, Tomoaki Inaba, and Taketo Uomoto. Study on Impact Acoustic Method and System Development Based on Wavelet Analysis. In *Proceedings International Symposium Non-Destructive Testing in Civil Engineering (NDT-CE), Berlin*, 2003.

[47] H. M. Nelson. High frequency flexural vibration of thick rectangular bars and plates. *Journal of Sound and Vibration*, 60(1):101 – 118, 1978. ISSN 0022-460X. doi:10.1016/0022-460X(78)90404-2. URL http://www.sciencedirect.com/science/article/pii/0022460X78904042.

[48] Sh Hosseini-Hashemi, M. Eshaghi, H. Rokni Damavandi Taher, and M. Fadaie. Exact closed-form frequency equations for thick circular plates using a third-order shear deformation theory. *Journal of Sound and Vibration*, 329(16):3382 – 3396, 2010. ISSN 0022-460X. doi:10.1016/j.jsv.2010.02.024. URL http://www.sciencedirect.com/science/article/pii/S0022460X10001471.

[49] Ji Lu. *Advancements in evaluation of air-coupled impact-echo test method*. PhD thesis, Iowa State University, Ames, Iowa, 2015. URL http://lib.dr.iastate.edu/etd/14490.

[50] M. Sansalone and W.B. Streett. *Impact-echo: non-destructive evaluation of concrete and masonry*. Bullbrier Press, 1997. ISBN 978-0-9612610-6-1.

[51] Anders Gudmarsson, Nils Ryden, and Bjrn Birgisson. Non-contact excitation of fundamental resonance frequencies of an asphalt concrete specimen. *AIP Conference Proceedings*, 1650(1):1401–1408, 2015. doi:10.1063/1.4914755. URL http://aip.scitation.org/doi/abs/10.1063/1.4914755.

[52] Arthur W. Leissa. Vibration of Plates. Technical Report NASA-SP-160, NASA, Washington, DC, United States, January 1969.

[53] Hyunjun Kim, Junhwa Lee, Eunjong Ahn, Soojin Cho, Myoungsu Shin, and Sung-Han Sim. Concrete Crack Identification Using a UAV Incorporating Hybrid Image Processing. *Sensors*, 17(9), 2017. ISSN 1424-8220. doi:10.3390/s17092052.

[54] S. Wongi Na and Jongdae Baek. Impedance-Based Non-Destructive Testing Method Combined with Unmanned Aerial Vehicle for Structural Health Monitoring of Civil Infrastructures. *Applied Sciences*, 7(1), 2017. ISSN 2076-3417. doi:10.3390/app7010015.

[55] Nanyaporn Intaratep, William N. Alexander, William J. Devenport, Sheryl M. Grace, and Amanda Dropkin. Experimental Study of Quadcopter Acoustics and Performance at Static Thrust Conditions. In *22nd AIAA/CEAS Aeroacoustics Conference*, Aeroacoustics Conferences. American Institute of Aeronautics and Astronautics, May 2016. doi:10.2514/6.2016-2873. URL https://doi.org/10.2514/6.2016-2873.

Appendix A

Images used in distance and crack width estimation

Images used for the analysis in Section 2.2 with the distance and crack width calculator utility are shown in the Figures A.1 to A.4, and are grouped according to the sample pictured and camera used.

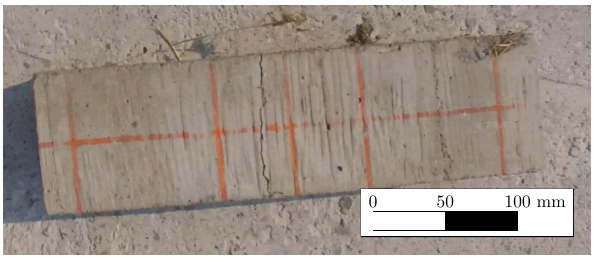

(a) $d \approx 0.5$ m

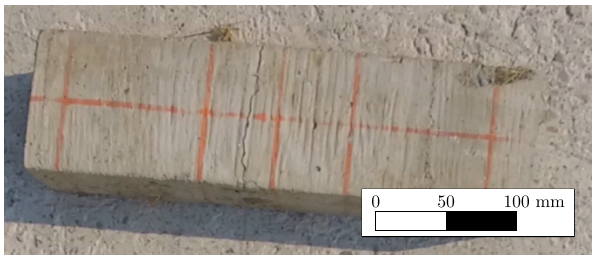

(b) $d \approx 0.9$ m

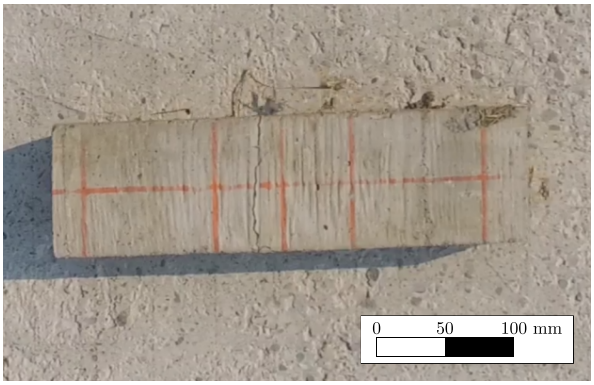

(c) $d \approx 1$ m

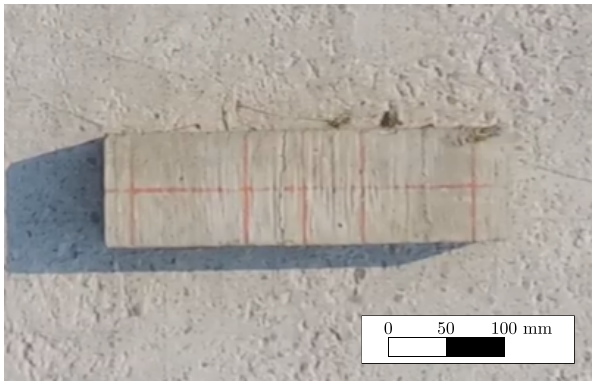

(d) $d \approx 2$ m

Figure A.1: Images for sample #1 from the Phantom 3 Standard.



(a) $d \approx 0.5$ m

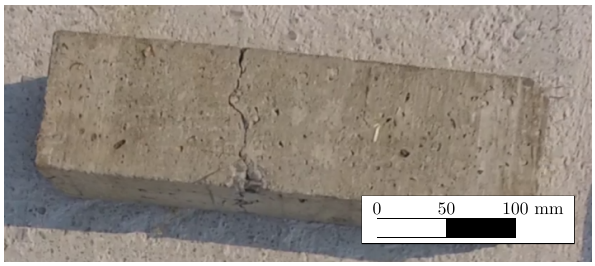

(b) $d \approx 0.9$ m

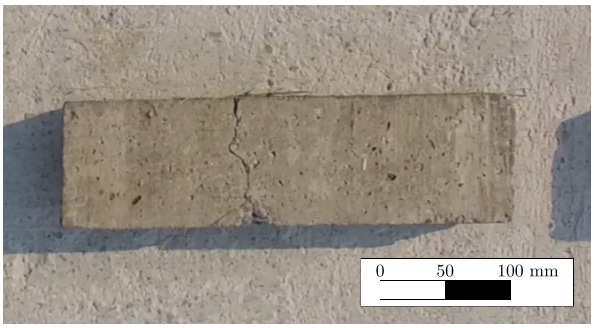

(c) $d \approx 1$ m

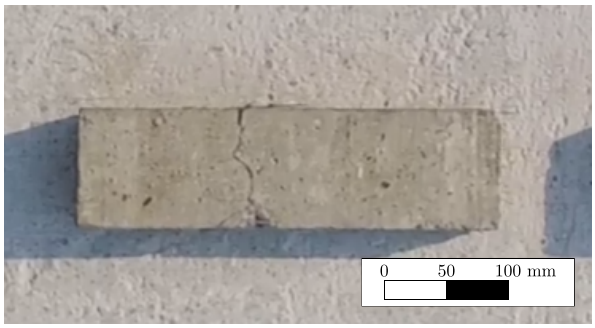

(d) $d \approx 2$ m

Figure A.2: Images for sample #2 from the Phantom 3 Standard.

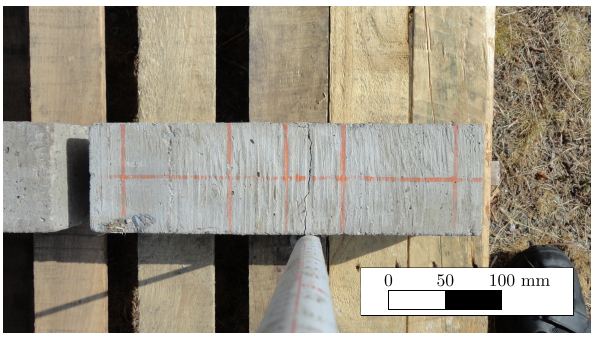

(a) $d \approx 0.5$ m



(b) $d \approx 1$ m

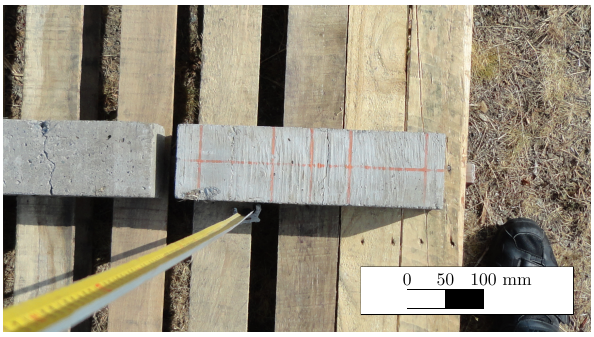

(c) $d \approx 1.5$ m

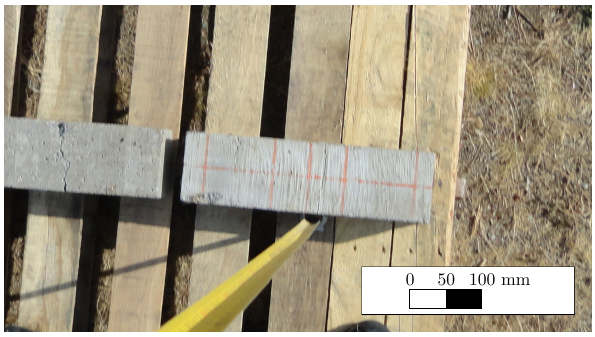

(d) $d \approx 2$ m

Figure A.3: Images for sample #1 from the Sony DSC-W570 Camera.

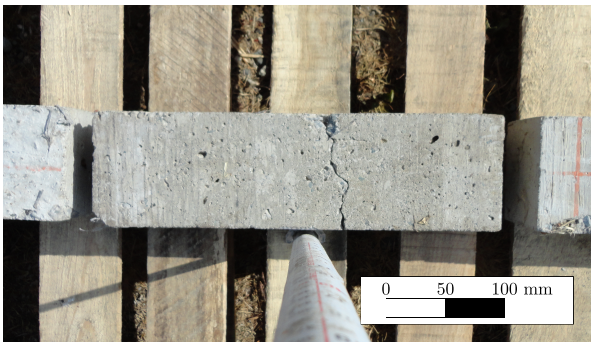

(a) $d \approx 0.5$ m

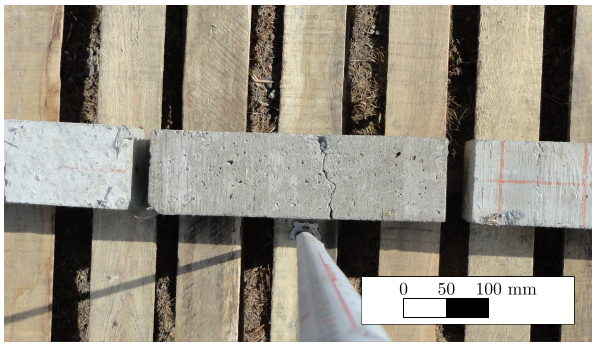

(b) $d \approx 1$ m

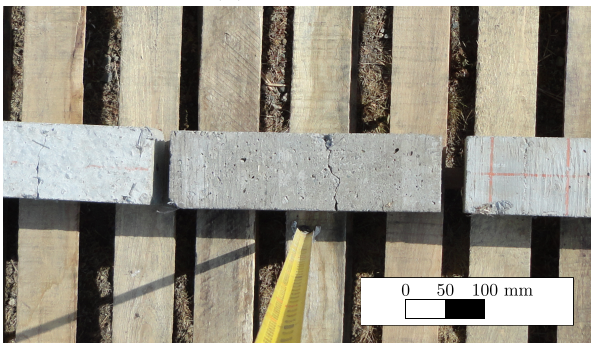

(c) $d \approx 1.5$ m

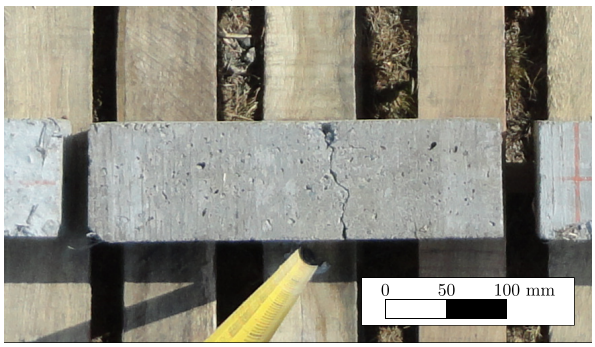

(d) $d \approx 2$ m

Figure A.4: Images for sample #2 from the Sony DSC-W570 Camera.

Appendix B

Thermal images of concrete slab specimens

Un-cropped infrared images of the concrete slab specimens taken using the FLIR Vue Pro camera are presented in the Figures B.1 to B.6. Slab numbers are indicated in the captions and are consistent with those in Figure 4.5. Images have been scaled to fit the format of this document.

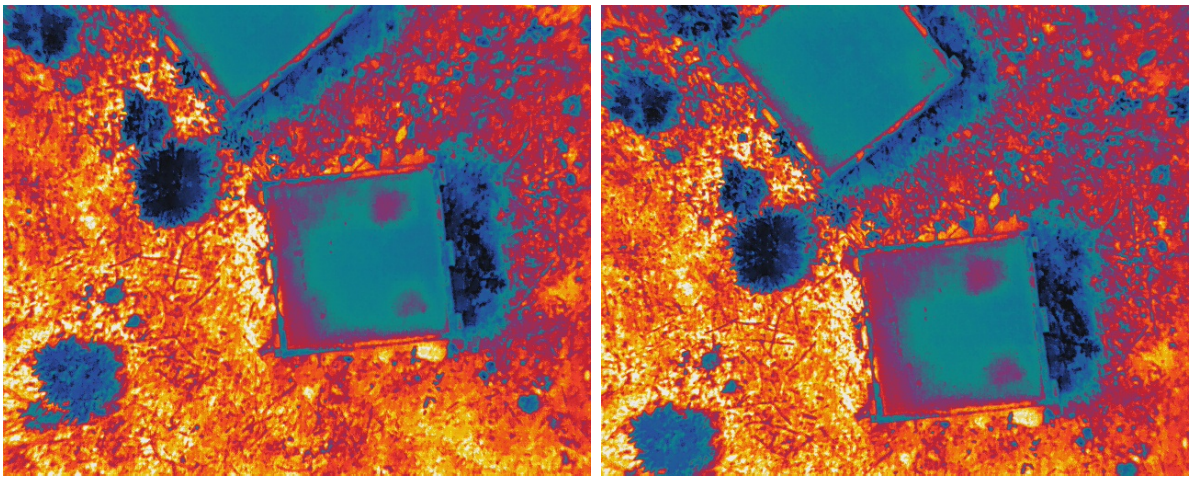

(a) Slab 1 (center) and 2 (top). (b) Slab 1 (bottom) and 2 (top).

Figure B.1: Thermal images of slabs #1 and 2.

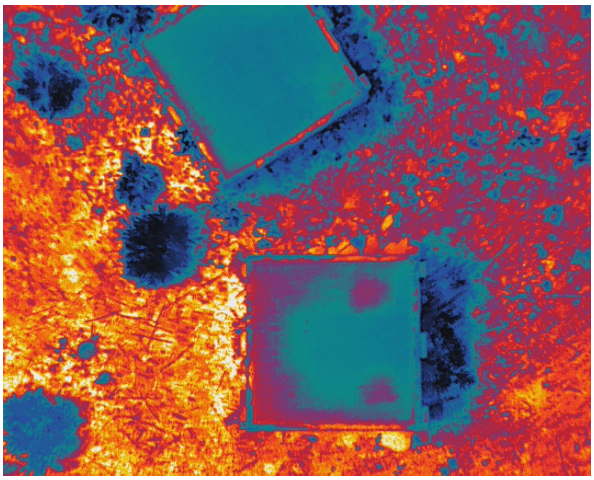

(a) Slab 1 (bottom) and 2 (top).

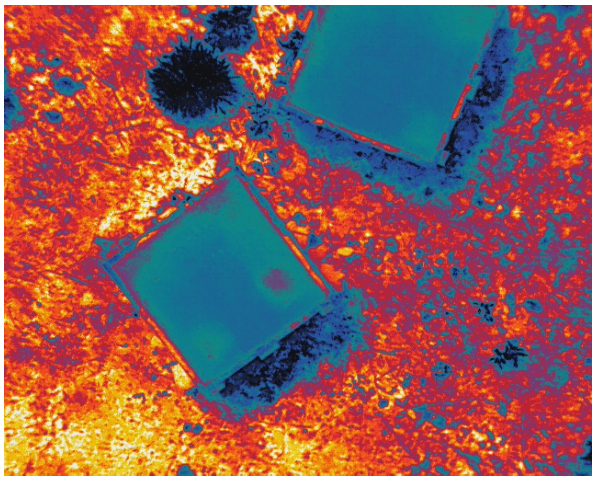

(b) Slab 1 (center) and 2 (top).

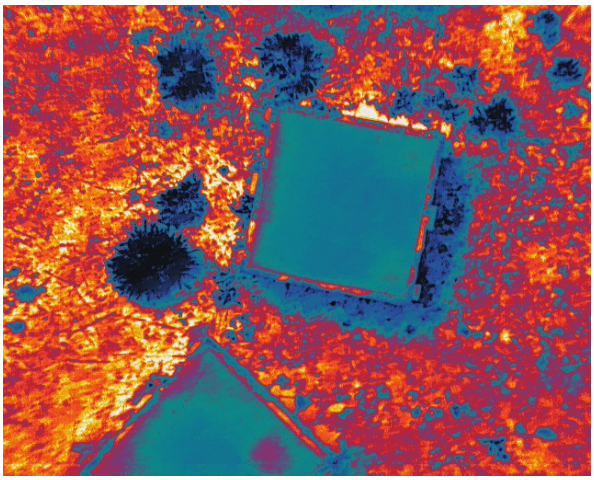

(c) Slab 2 (center) and 1 (bottom).

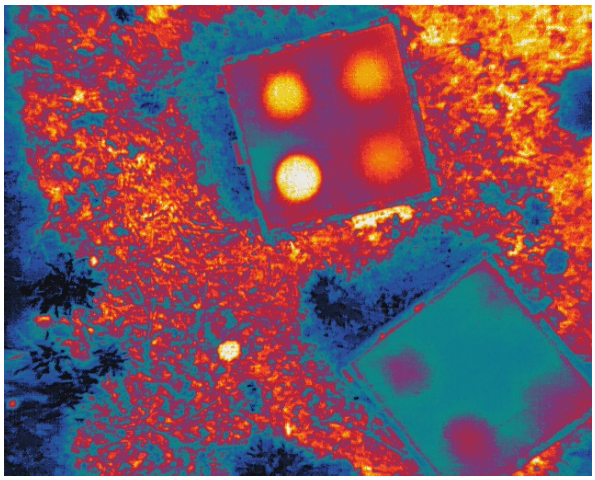

(d) Slab 3 (top) and 4 (bottom right).

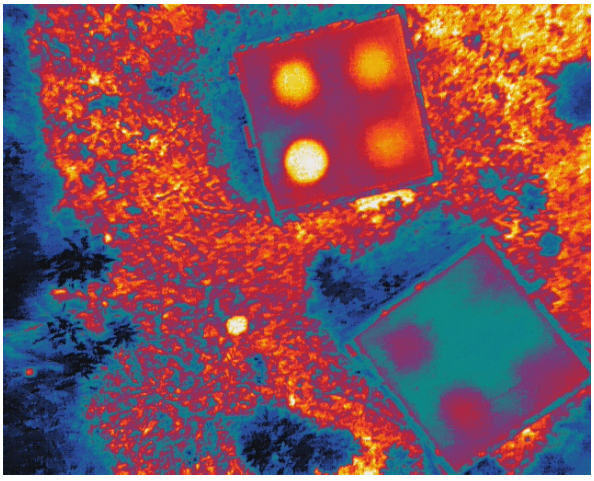

(e) Slab 3 (top center) and 4 (bottom right).

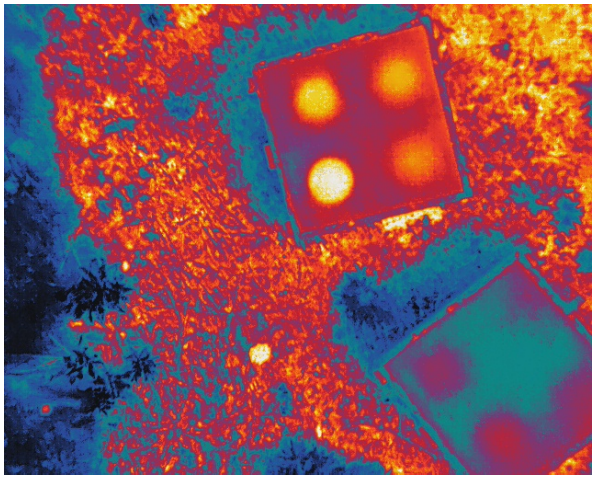

(f) Slab 3 (top center) and 4 (bottom right).

Figure B.2: Thermal images of slabs #1, 2, 3, and 4.

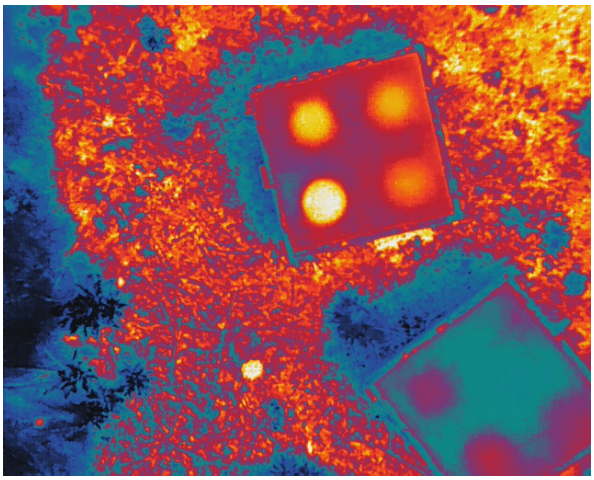

(a) Slab 3 (top center) and 4 (bottom right).

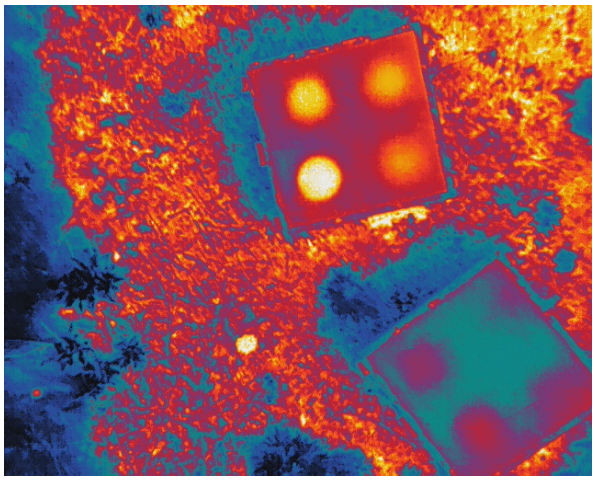

(b) Slab 3 (top center) and 4 (bottom right).

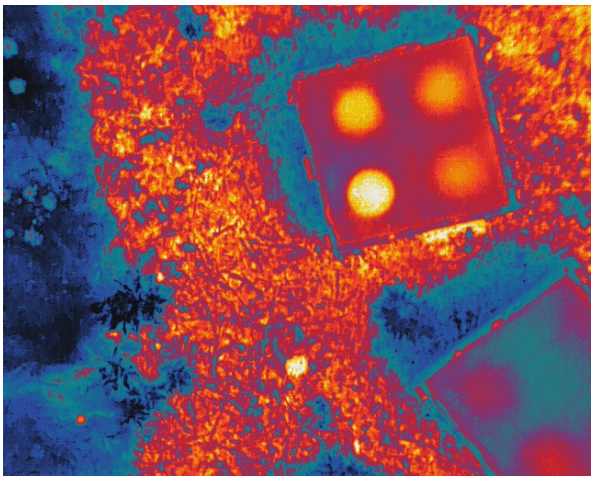

(c) Slab 3 (top center) and 4 (bottom right).

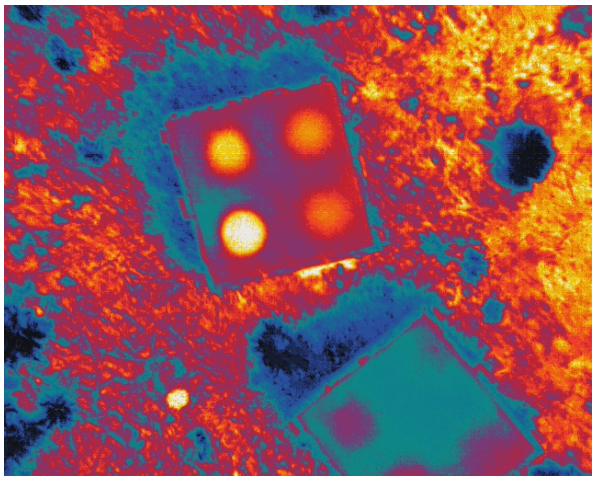

(d) Slab 3 (center) and 4 (bottom right).

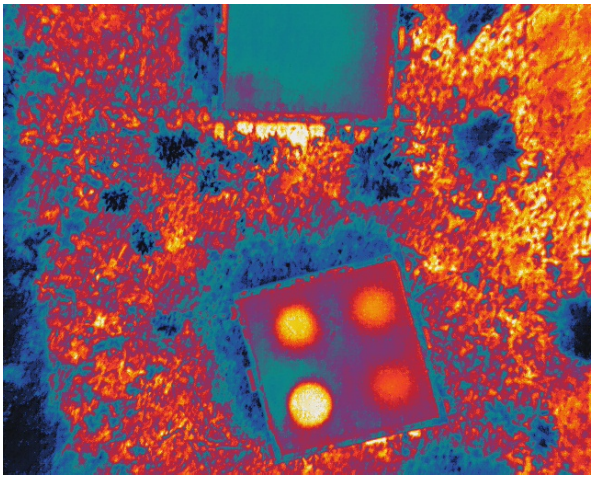

(e) Slab 2 (top) and 4 (bottom).

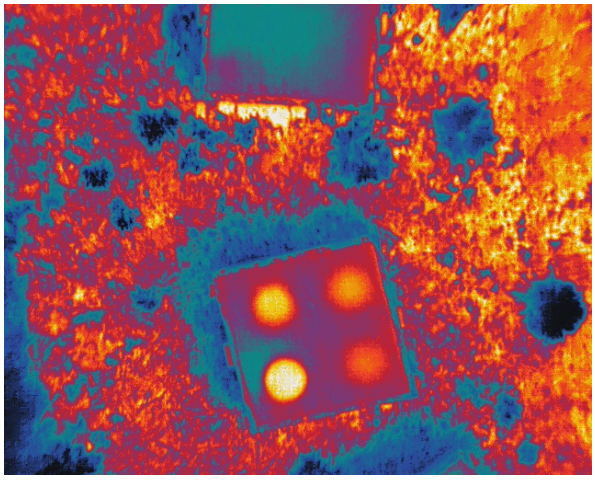

(f) Slab 2 (top) and 4 (bottom).

Figure B.3: Thermal images of slabs #3 and 4.

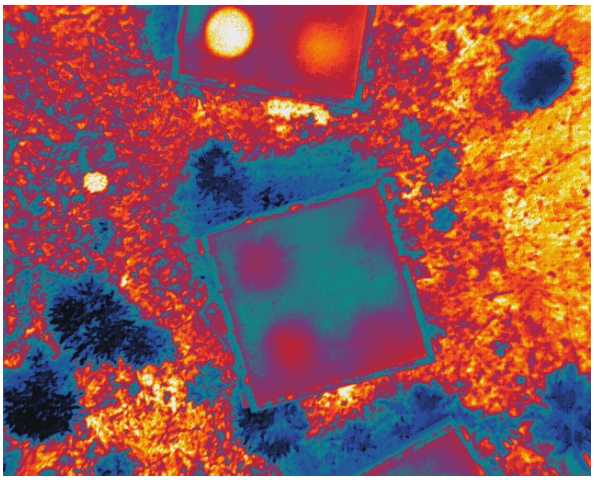

(a) Slab 3 (top) and 4 (center).

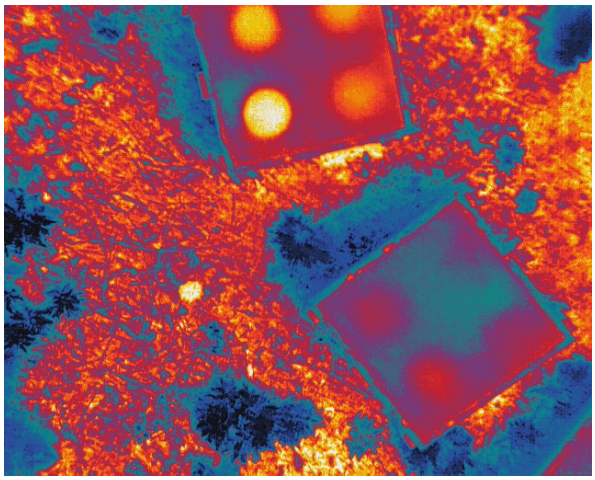

(b) Slab 3 (top center) and 4 (bottom right).

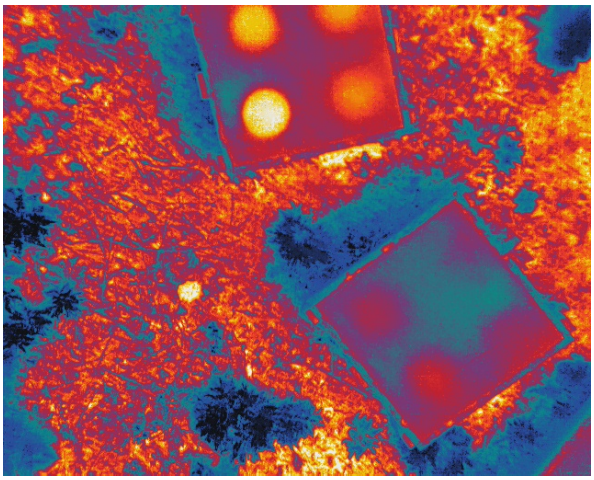

(c) Slab 3 (top center) and 4 (bottom right).

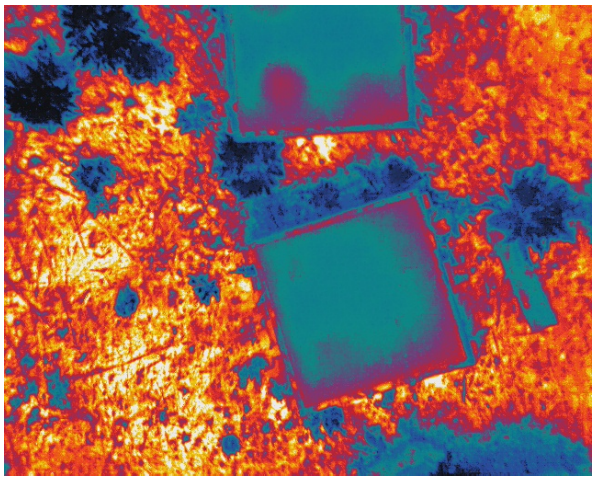

(d) Slab 4 (top) and 5 (center).

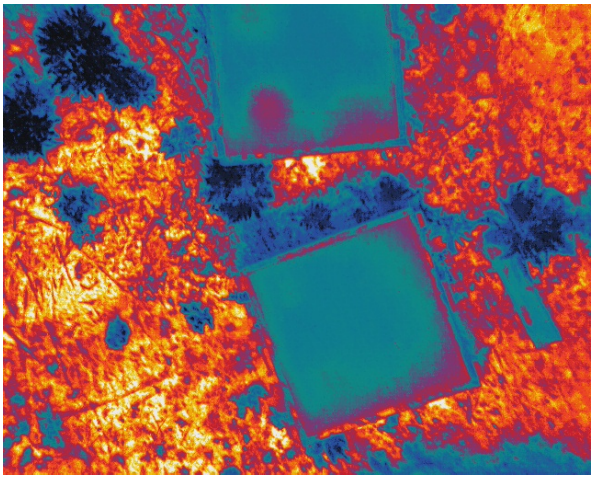

(e) Slab 4 (top) and 5 (middle).

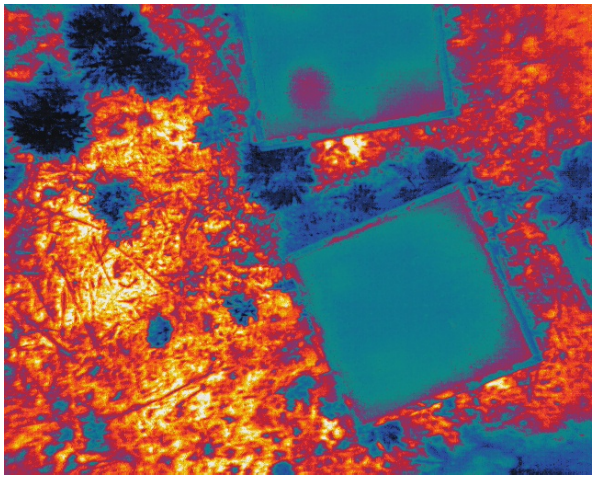

(f) Slab 4 (top) and 5 (center right).

Figure B.4: Thermal images of slabs #3, 4, and 5.

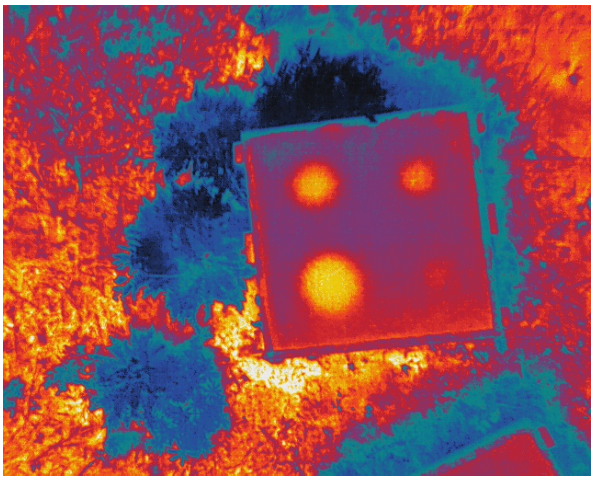

(a) Slab 6 (center) and 5 (bottom right).

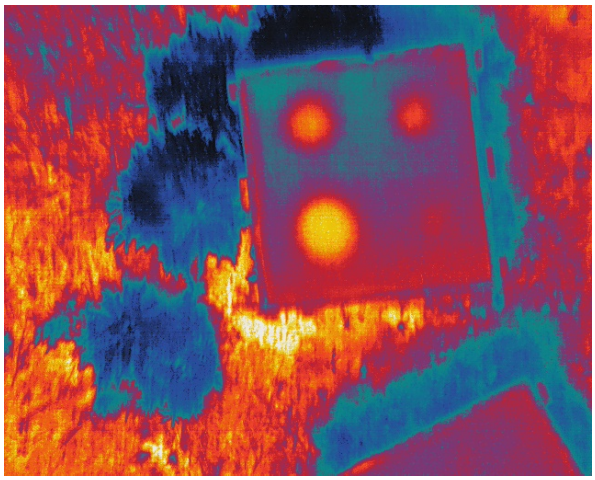

(b) Slab 6 (center) and 5 (bottom right).

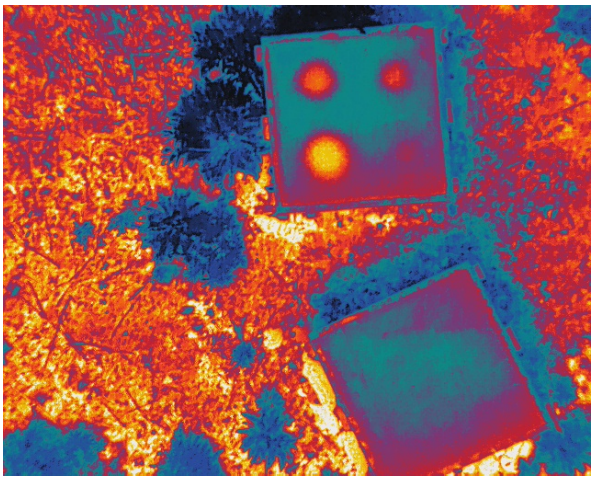

(c) Slab 6 (top center) and 7 (bottom right).

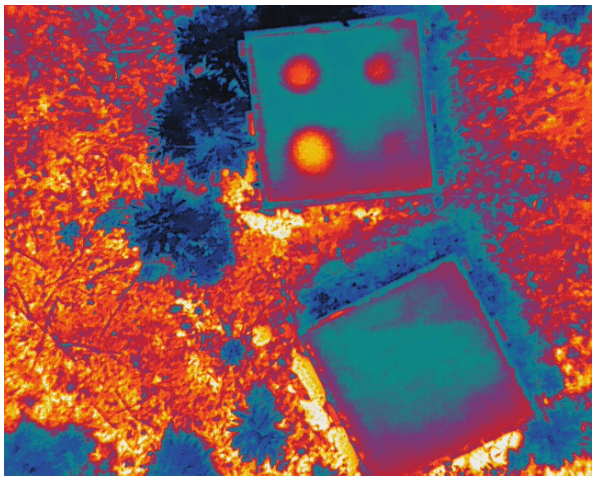

(d) Slab 6 (top center) and 7 (bottom right).

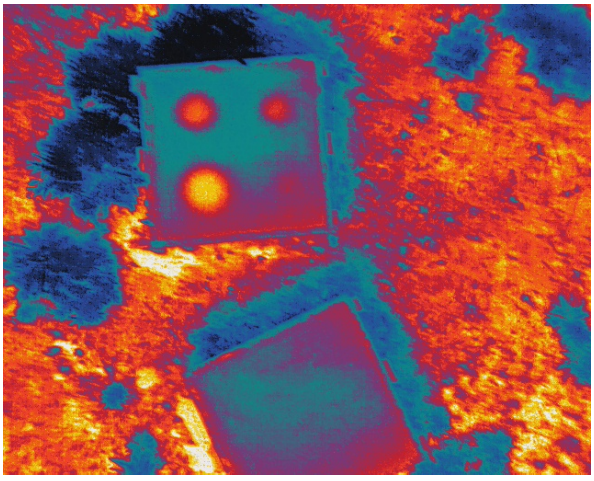

(e) Slab 6 (upper left) and 7 (bottom).

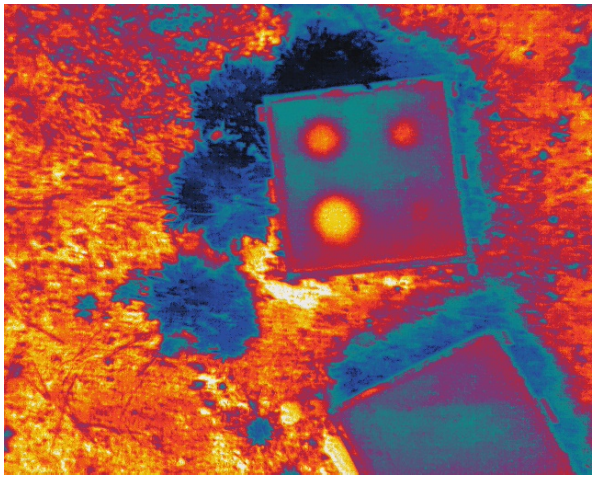

(f) Slab 6 (middle) and 7 (bottom right).

Figure B.5: Thermal images of slabs #6 and 7.

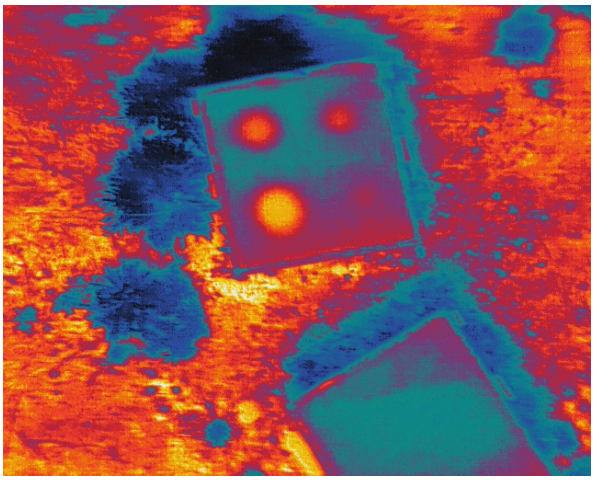

(a) Slab 6 (middle) and 7 (bottom right).

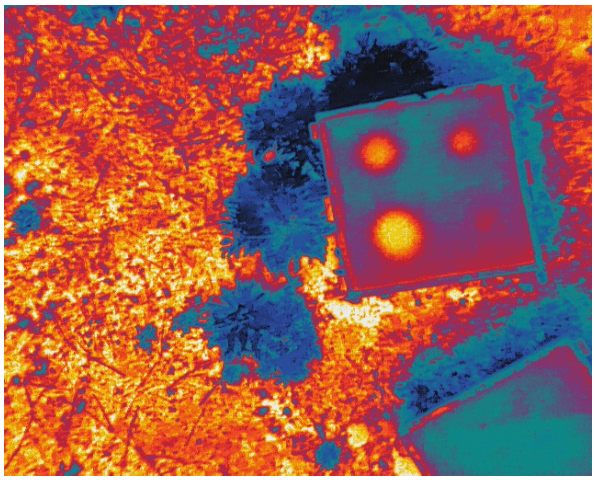

(b) Slab 6 (middle) and 7 (bottom right).

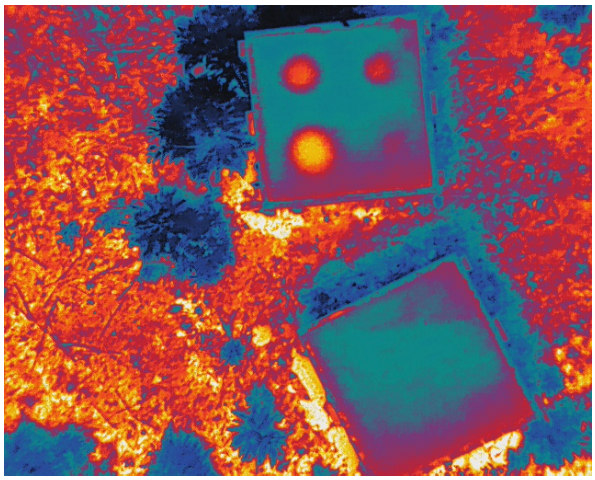

(c) Slab 6 (top) and 7 (bottom right).

Figure B.6: Thermal images of slabs #6 and 7.

Appendix C

i3P Prototype Images

Images of the i3P prototype are presented in this appendix. Images show the structure of the i3P prototype and its control remote, as well as a basic optical image broadcast to the viewing monitor.

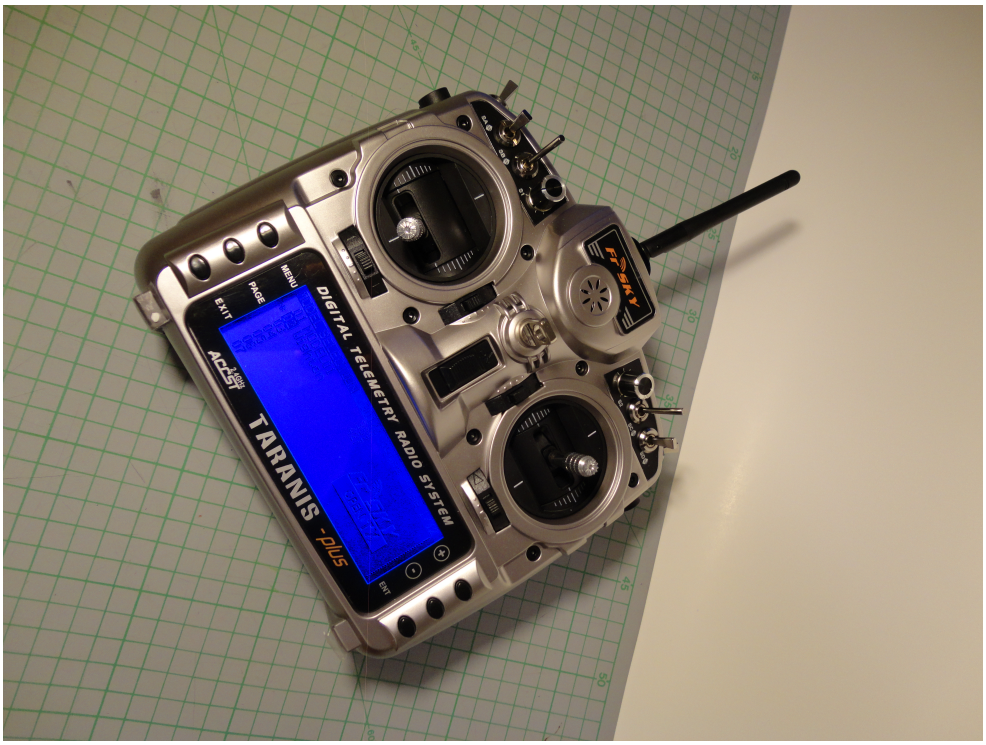

Figure C.1: Taranis X9D Plus RC Remote

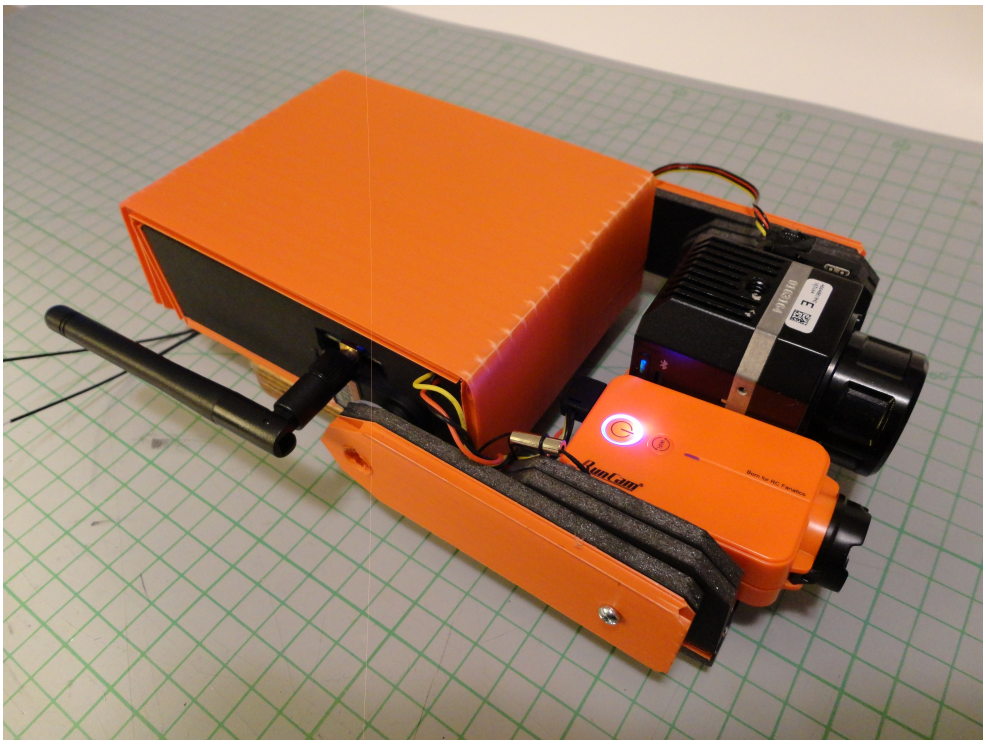

(a) i3P overview showing video and control antennae.

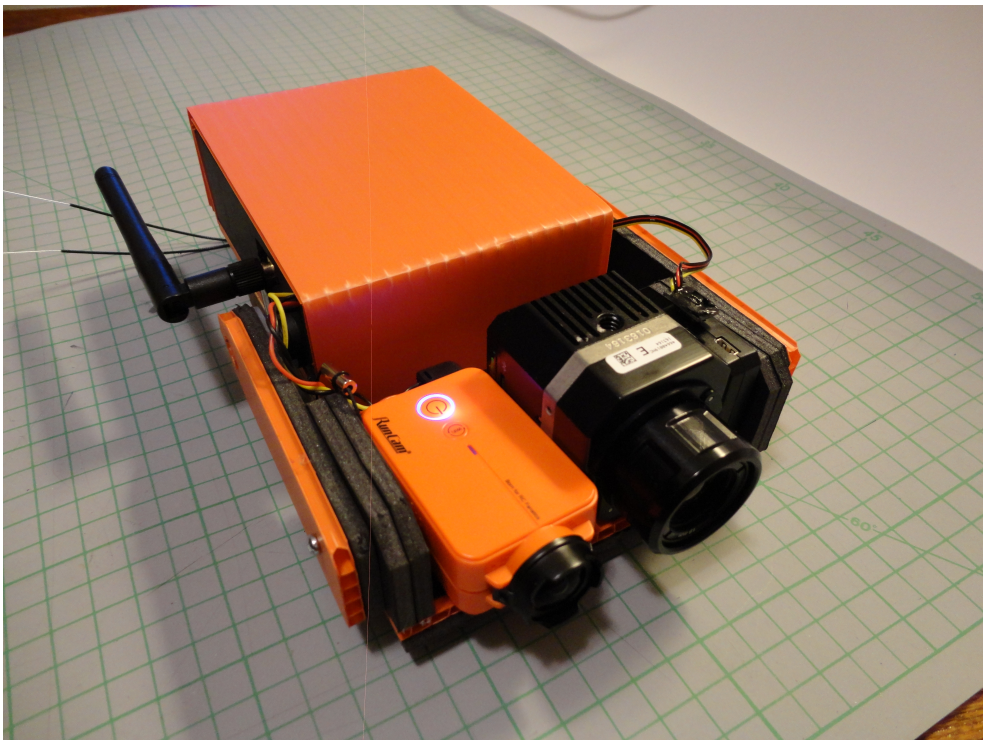

(b) i3P prototype with cameras forward facing.

Figure C.2: i3P prototype showing cameras and antennae.

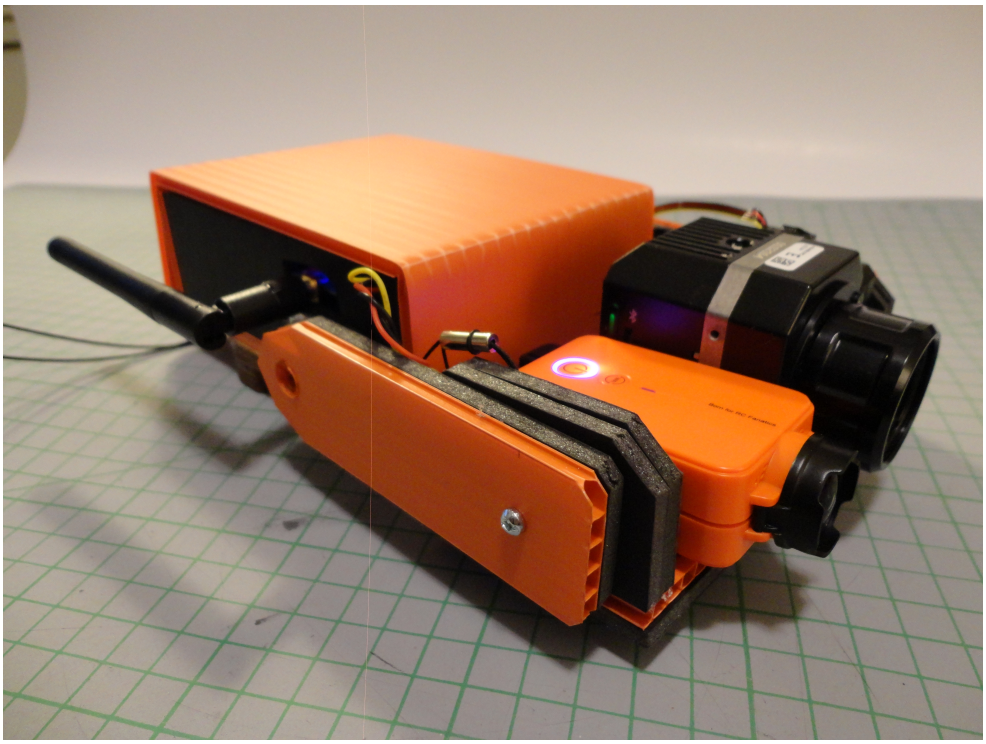

(a) i3P prototype with arms in the down position.

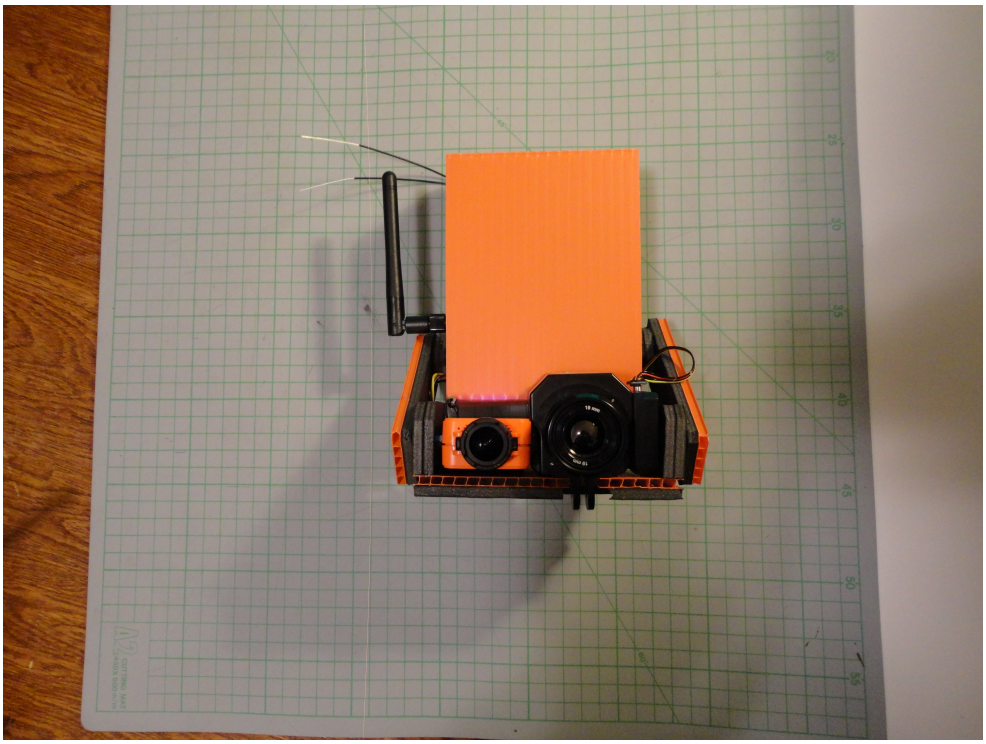

(b) i3P prototype with cameras facing upward.

Figure C.3: i3P prototype showing arm positions.

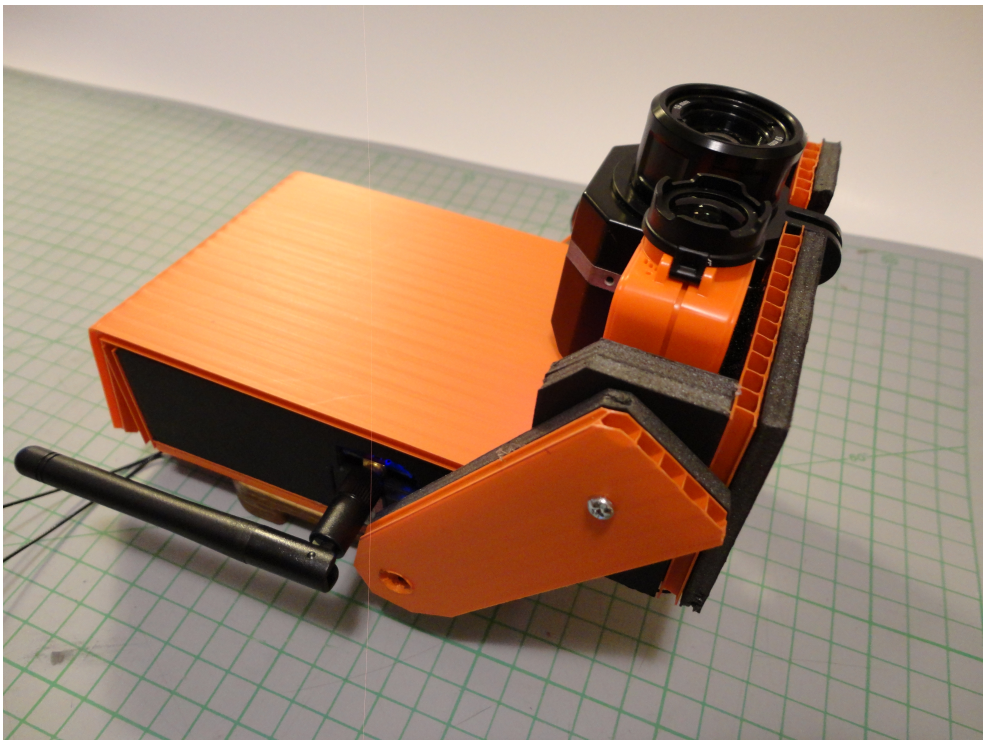

(a) i3P prototype with arms extended to roughly 45°.

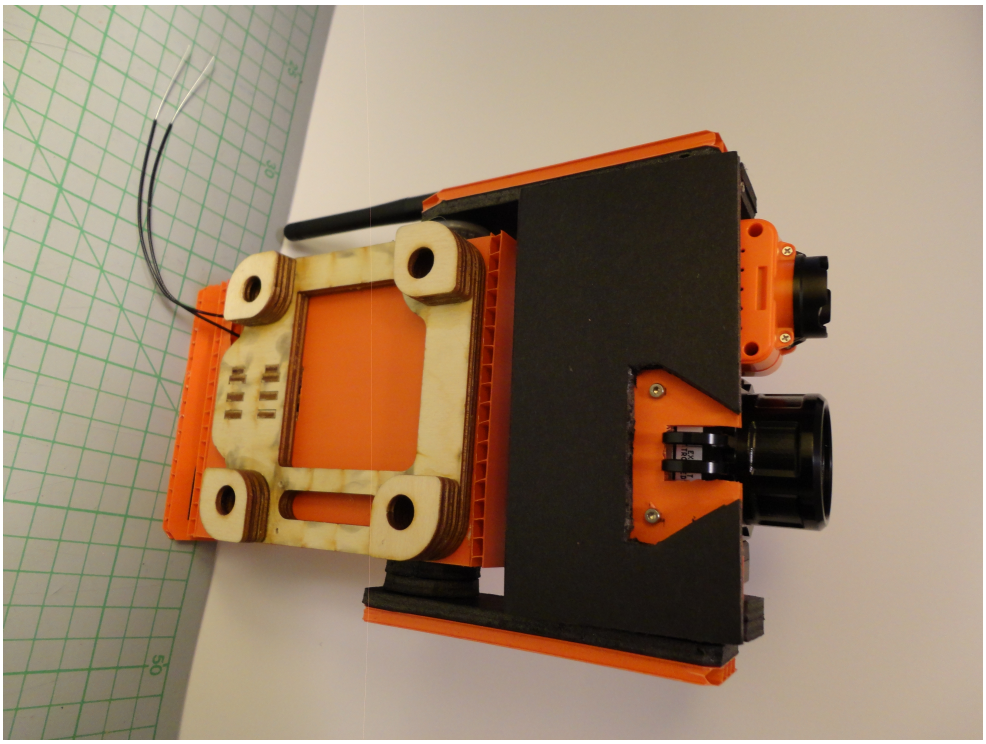

(b) Underside of i3P prototype.

Figure C.4: i3P prototype images.

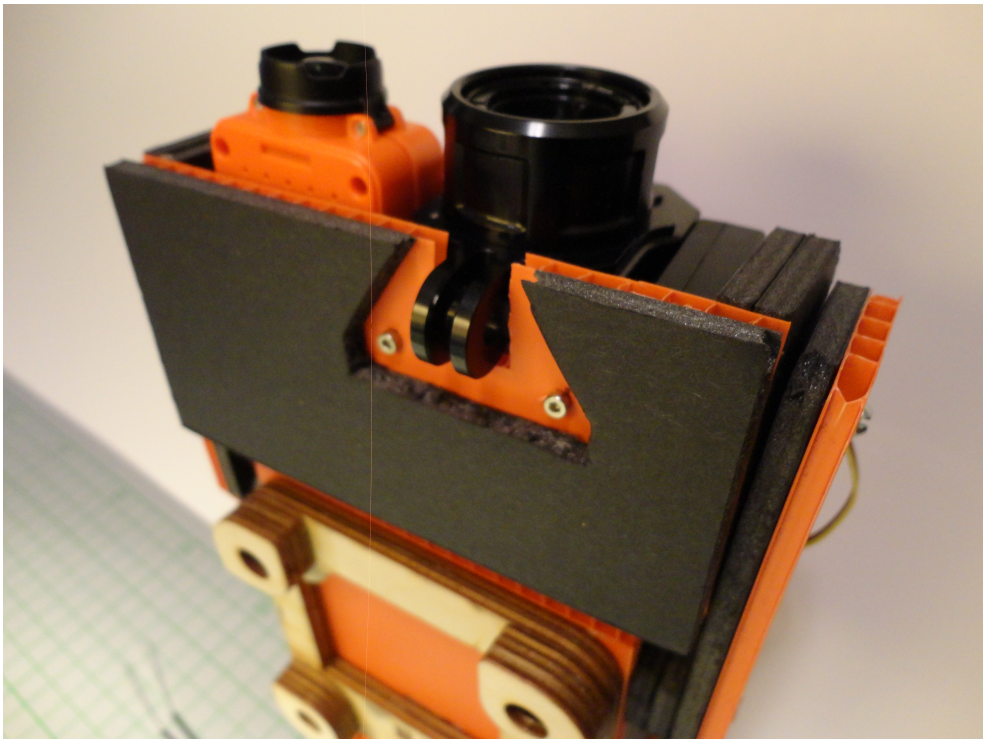

(a) Underside of i3P prototype camera platform.

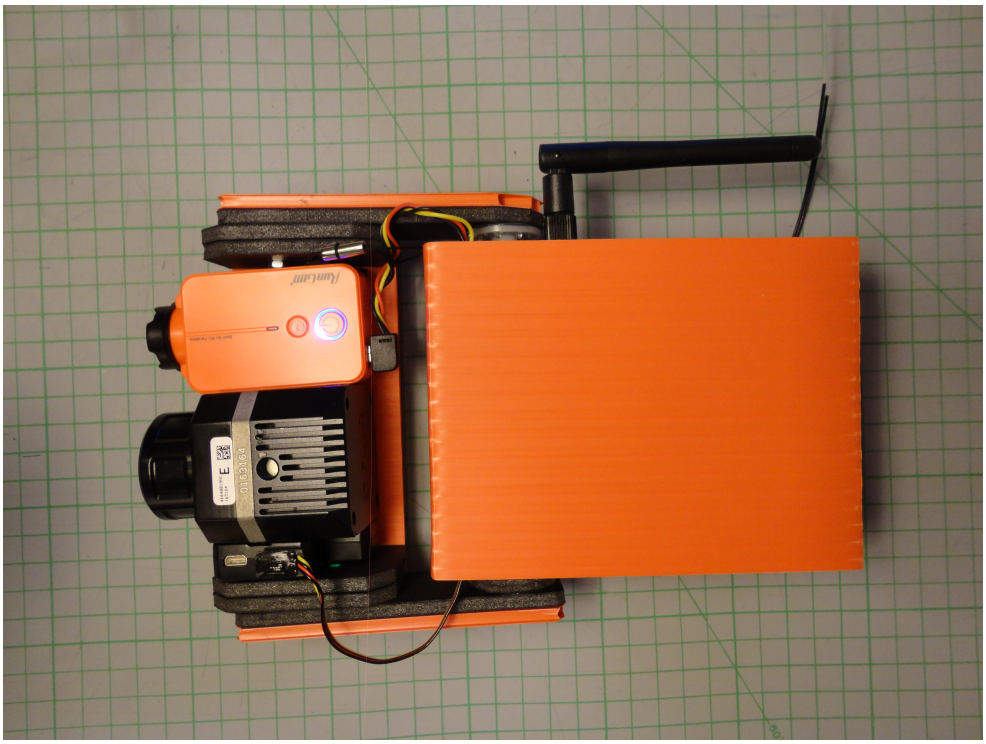

(b) Top view of i3P prototype.

Figure C.5: i3P prototype images showing opposite sides.

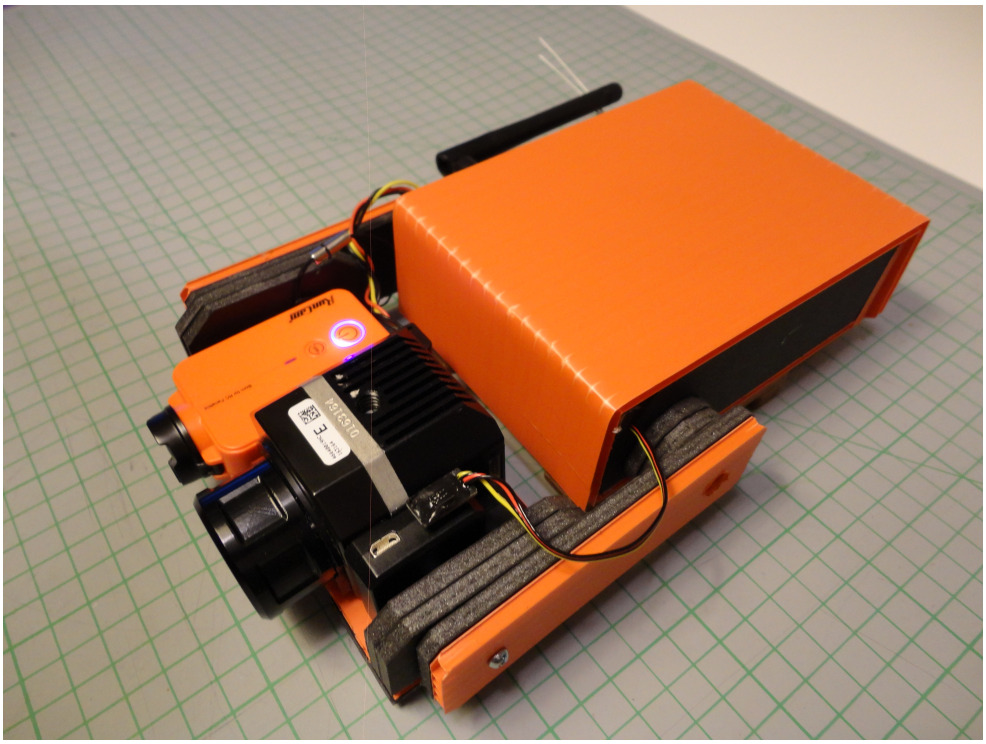

(a) i3P prototype showing FLIR Vue Pro power and signal cable.

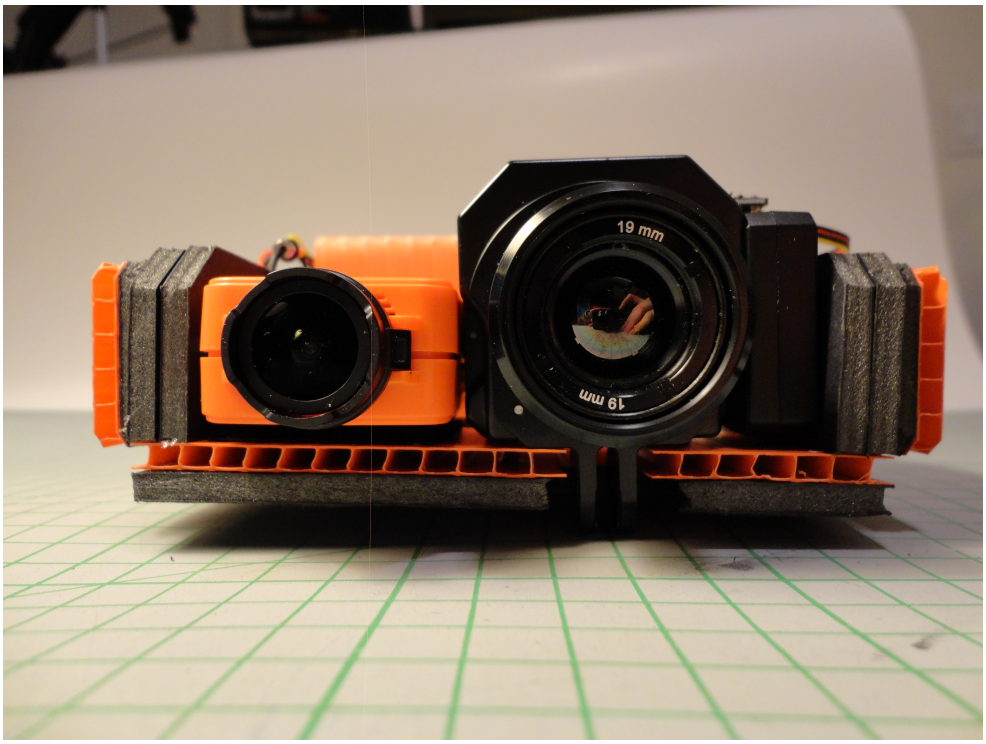

(b) i3P prototype front view.

Figure C.6: i3P prototype images featuring optical and thermal cameras.

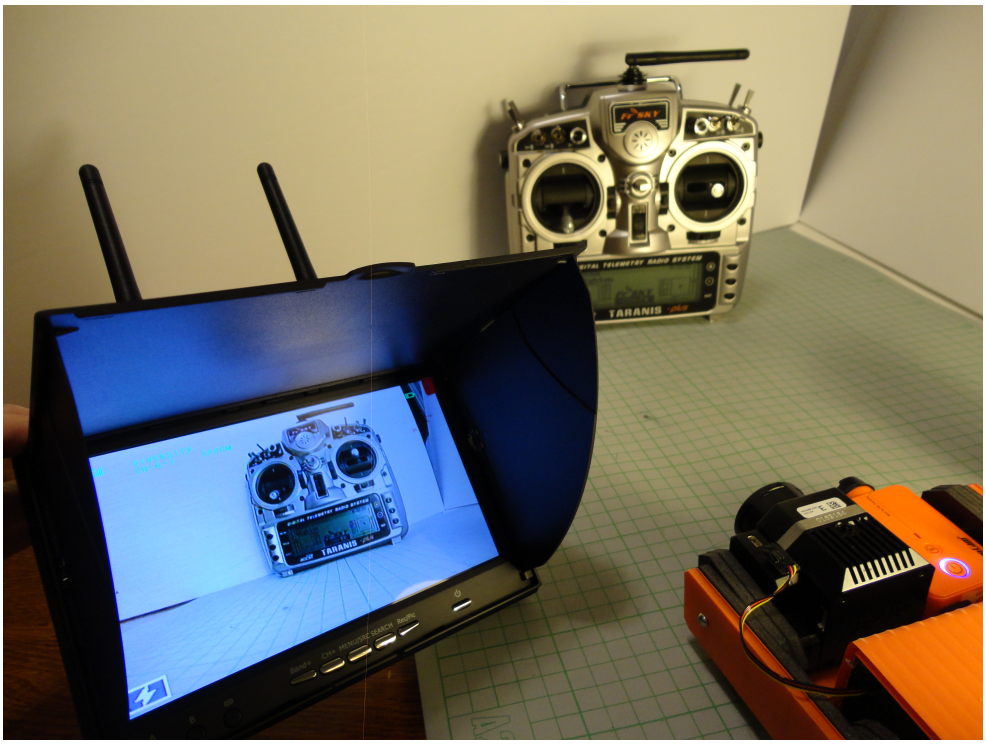

Figure C.7: i3P showing optical camera broadcast.